COMPUTATIONAL MODELS OF NEUROVASCULAR COUPLING

Katharina Dormanns

A thesis submitted in partial fulfilment of the requirements for the Degree of Doctor of Philosophy in Mechanical Engineering at the University of Canterbury.

November 2015

Katharina Dormanns: *Computational Models of Neurovascular Coupling*, Department of Mechanical Engineering, University of Canterbury, Christchurch, New Zealand, November 2015

"You have brains in your head.

You have feet in your shoes.

You can steer yourself any direction you choose."

— Dr. Seuss (Oh, The Places You'll Go!)

Dedicated to our son Samuel.

* 26.01.2014

PREFACE

Material covered in Chapters 4 to 7 of this thesis have been published in international, peer-reviewed journals. The author of this thesis, Katharina Dormanns, has contributed with 50 % or more of the workload for the preparation of each of the manuscripts. Co-authorship forms are attached.

Permission for the reproduction of figures and excerpts of text have been obtained from the publishers where applicable.

Chapters 4 and 5:

K. Dormanns, E. M. J. van Disseldorp, R. G. Brown and T. David (2015): Neurovascular coupling and the influence of luminal agonists *via* the endothelium. Journal of Theoretical Biology 364: 49-70.

Permission guidelines of the journal: Authors retain the rights to include their articles in full or in part in a dissertation for non-commercial purposes.[1]

Chapter 6:

K. Dormanns, R. G. Brown and T. David (2015): The Role of Nitric Oxide in Neurovascular Coupling. Journal of Theoretical Biology. Submitted on 15th June 2015, currently under review.

Chapter 7:

K. Dormanns, R. G. Brown and T. David (2015): Neurovascular Coupling: A Parallel Implementation. Frontiers in Computational Neuroscience 9:109. Open access publication.

1 https://www.elsevier.com/about/company-information/policies/copyright/permissions

The foundation model of the neurovascular unit (NVU) and the nitric oxide signalling pathway described in Chapter 4 and Chapter 6, respectively, are based on the work of Dr. Hannah Farr during her doctoral studies (2009-2012) in the Bluefern Supercomputing Unit of the University of Canterbury under supervision of Prof. Tim David.

The NVU model was developed further in a cooperative effort by the visiting research assistants Loes van der Donk, Evert de Kock and Emiel van Disseldorp from the University of Eindhoven, Netherlands, under the direct supervision of Katharina Dormanns and Prof. Tim David.

The vascular tree model (Chapter 7) was originally developed by Dr. Richard Brown and adapted and implemented into the present work by Katharina Dormanns.

CONTENTS

"Out there things can happen, and frequently do,
To people as brainy and footsy as you.
And when things start to happen, don't worry, don't stew.
Just go right along, you'll start happening too!"

— Dr. Seuss (Oh, The Places You'll Go!)

ACKNOWLEDGEMENTS

This journey started and "things happened" with a one-way ticket in our hands – a ticket to Christchurch which is, with an exact 18,738 km, the furthest place on earth away from where my husband Jan and I lived before. It has been a journey full of unforgettable experiences, wonderful encounters and, with the birth of our son Samuel, the biggest miracle we could have ever imagined. I owe many thanks to all the fabulous people who supported me during this journey from near and far.

I would like to express my deep sense of gratitude to my supervisors Prof. Tim David and Dr. Richard G. Brown. Thank you for your outstanding guidance and encouragement on a professional and personal level. I'm immensely grateful for your valuable advice over the past years and our friendship.

My thanks go to all members of our outstanding "BRATS" research group, especially Christine de Lancea, Michelle L. Goodman, Ealasukanthan Thavanayagam, Elshin Mathias, Jaijus P. Johny and Tim van Ginkel. Thank you for helpful discussions, the great experience and our famous late-night group dinners, I always felt surrounded by friends in this team. Special thanks to Tim for proofreading this thesis.

Thanks to all the visiting researchers from all over the world. Dr. Vera Novak, Prof. Pierre Gremaud, Emiel M. J. van Disseldorp, Loes van der Donk, Evert G. J. de Kock, Lisa Wiesent, Franziska Hoyer, Allanah Kenny,

Sanne van der Lelij, Thomas Hölscher, Joerik de Ruijter, Stewart Dowding, Dominic Roberts and Jan Dembianny. Thank you for your valuable input. Special thanks to Allanah for your help with the AUTO program.

I would like to convey my thanks to all members of the UC HPC Centre. How lucky are we to be allowed to share the office with you wonderful people. Thank you for all the advice and help with computational questions and beyond, especially Dr. Sung E. Bae, Anthony Dale, Dan Sun and Dr. François R. P. Bissey. Thanks to Angela Armstrong for her endless support on so many levels.

Thank you all for allowing me to bring Samuel in the office from time to time. Especially in the first couple of months this was immensely helpful.

I want to especially thank the University of Canterbury for granting a UC Doctoral Scholarship, which made this journey possible in the first place.

Thanks to Tim and the BRATS group for the excellent opportunity to attend the Australasian winter conferences on brain research (AWCBR) in Queenstown in 2013, 2014 and 2015, the World Congress of Biomechanics in Boston in 2014 and the Computational Neuroscience and Neuromorphic Engineering Workshop in Queenstown in 2015. I acknowledge with thanks the three travel grants provided through the generosity of the Neurological Foundation of New Zealand.

I would like to thank all my friends here, at home and around the globe for so much. Please stay the wonderful selves you are. Special thanks to Rachelle Binny for her thesis writing support, you are the best "thing that happened" on our first day here in New Zealand. To my parents and my family, thank you for encouraging me in all of my pursuits and inspiring me to live my dreams. No matter how far apart we are, you will always be in my heart.

Thank you, Jan. Thank you, Samu. This journey with you could not have been more wonderful. I love you both.

ABSTRACT

The human brain critically relies on a continuous blood supply to ensure its function. Impaired cerebral perfusion is associated with diseases, such as Alzheimer's Disease, cortical spreading depression and stroke. Cerebral cells work together to ensure a finely regulated blood supply. However, many of the underlying mechanisms of this regulation, termed neurovascular coupling (NVC), are still not fully understood.

The development of mathematical models of cell signalling is a promising approach that complements experimental studies by investigating the contribution of key components and pathways and guiding further experiments.

This dissertation reports the development of a lumped parameter compartment model of a neurovascular unit (NVU), comprising neurons, astrocytes, smooth muscle cells (SMCs) and endothelial cells (ECs). The model couples neuronal activity to vasodilation/contraction models *via* the astrocytic mediated perivascular K^+ and the smooth muscle Ca^{2+} pathway. It successfully relates a neuronal input signal to the corresponding vessel reaction.

It was found that the voltage-operated Ca^{2+} channels are, due to the hyperpolarisation from the K^+ efflux of the SMC, almost entirely closed and do not seem to play a significant role during neuronal activity.

The current model shows that in contrast to a number of experiments, outlining the importance of astrocytic Ca^{2+} in NVC, this Ca^{2+} pathway is not the only one mediating NVC.

Model inputs from the endothelial side of the blood vessel in the form of luminal agonists provide a flux of inositol trisphosphate (IP_3) into the EC

cytosol. EC/SMC coupling through gap junctions has a substantial effect on the NVC dynamics. The IP_3 influx induces Ca^{2+} release from the SMC stores resulting in Ca^{2+}-induced Ca^{2+} release oscillations which were shown to inhibit NVC.

The incorporation of nitric oxide (NO) signalling pathways in the NVU model shows the vasodilating effects of NO in the resting state. Furthermore, dilation during neuronal activation is enhanced with NO dynamics included. Results show that K^+ release is responsible for the fast onset of vascular response, whereas NO-modulated mechanisms maintain dilation. The governing source of NO that diffuses into the SMC, which provides the contractile force, depends on neuronal activation. In the resting state the EC provides the major contribution of NO release for vasorelaxation, whereas during neuronal stimulation NO produced by the NE dominates.

In a scaled model, embedded in a parallel computing environment, multiple NVUs were connected to a space filling binary tree, facilitating the simulation of a perfusing vascular tree. The model couples the NVUs to the vasculature *via* stretch-mediated Ca^{2+} channels on both the EC and SMC.

The coupling between the vasculature and the set of NVUs was found to be relatively weak for the case with agonist induced where only the Ca^{2+} in cells inside the activated area becomes oscillatory. However, the radii of vessels both inside and outside of activated areas oscillate (albeit small for those outside).

In addition, simulations reveal a different oscillation profile when comparing coupled and decoupled states with the time required to refill the cytosol with decreasing Ca^{2+} and increasing frequency with coupling. The solution algorithm is shown to have excellent weak and strong scaling. Results have been generated for tissue slices containing up to 4096 NVUs, which corresponds to an area of 2.5 cm $\times$ 2.5 cm of cerebral tissue.

LIST OF FIGURES

LIST OF TABLES

LISTINGS

ABBREVIATIONS

20-HETE 20-hydroxyeicosatetraenoic acid

AA arachidonic acid

AC astrocyte

A-β amyloid-β

AD Alzheimer's Disease

ADP adenosine diphosphate

APP amyloid precursor protein

ATP adenosine triphosphate

BBB blood brain barrier

BK big potassium

Ca^{2+} calcium ion

CAC cerebral arterial circle

CBF cerebral blood flow

CCO constrained constructive optimisation

cGMP cyclic guanosine monophosphate

CICR calcium-induced calcium release

Cl^{-} chloride ion

CO_2 carbon dioxide

CSD cortical spreading depression

CSF cerebrospinal fluid

EC endothelial cell

ECF extracellular fluid

ECS extracellular space

EET epoxyeicosatrienoic acid

ER endoplasmic reticulum

GABA gamma-aminobutyric acid

GJ gap junction

Glu glutamate

H^+ hydron

HCO_3^- bicarbonate

iGlu-R ionotropic glutamate receptor

IP_3 inositol trisphosphate

K^+ potassium ion

KCC1 Potassium chloride cotransporter type 1

KIR inward-rectifying potassium

MLC myosin light chain

MPI message passing interface

Na^+ sodium ion

NE neuron

NKCC1 sodium-potassium-chloride cotransporter type 1

NMDA-R N-methyl-D-aspartate receptor

NO nitric oxide

NVC neurovascular coupling

NVS neurovascular simulator

NVU neurovascular unit

O_2 oxygen

ODE ordinary differential equation

PDE partial differential equation

PLC phospholipase C

PVS perivascular space

SAC stretch-activated channel

SC synaptic cleft

SERCA sarcoplasmic/endoplasmic reticulum calcium-ATPase

SMC smooth muscle cell

SR sarcoplasmic reticulum

TCA tricarboxylic acid

TRPV4 transient receptor potential cation channel subfamily V member 4

VOCC voltage-operated calcium channel

WSS wall shear stress

1

INTRODUCTION

1.1 MAMMALIAN BRAIN

The brain has the most sophisticated and complex structure of all organs. It is responsible for general control over the organism and it executes all purposeful movements. It critically relies on the supply of oxygen (O_2) and nutrients by the perfusion of blood to the cerebral tissue.

1.1.1 *Anatomy and Histology*

The brain forms, together with the spinal cord, the central nervous system. It is commonly divided into the following five embryonic structures (from the Greek *en cephalon*, "in the head"), which the brains of all vertebrates have in common and from which the mature parts develop (see also Figure 1a):

- Telencephalon ("endbrain", develops into cerebral cortex, hippocampus, basal ganglia and olfactory bulb)
- Diencephalon ("interbrain", develops into thalamus and hypothalamus)
- Mesencephalon ("midbrain")
- Metencephalon ("hindbrain", develops into pons and cerebellum)
- Myelencephalon ("marrowbrain", develops into medulla oblongata)

Sometimes the telencephalon and the diencephalon are together referred to as the "forebrain" and the metencephalon and the myelencephalon as the "hindbrain".

The three main components of the brain are the cerebral cortex (also called cerebrum), the cerebellum, and the brainstem (medulla oblongata, pons and midbrain) and have distinct functions. The cortex is the largest and most developmentally advanced part. It forms two symmetric cerebral hemispheres, each of which are specialised for distinctive roles. Language and the dexterity of the right hand are controlled by the left hemisphere of the human brain, whereas the right hemisphere is dominant in the control of the sense of objects' interrelation in space (MacNeilage et al., 2009). The two almost mirrored cerebral hemispheres are connected by a bundle of over 200 million neural fibres (corpus callosum), through which communication is realised.

The surface of both hemispheres is heavily folded, forming ridges (gyri) and grooves (sulci if shallow and fissures if deep), which allow the cortex to grow immensely in surface area without necessarily increasing in volume. The sulci and fissures divide the cortex into functional lobes, which are (from anterior to posterior): frontal, temporal, parietal and occipital lobe (Duvernoy, 1999), see Figure 1b).

The cortex is responsible for several higher functions, including vision, hearing, speech, emotions, executive function, and the fine control of movement. The cerebellum is the second largest component and is responsible for maintaining balance and further control of movement and coordination. The brainstem connects the cerebral structures and the spinal cord. It is responsible for automatic survival functions, such as control of respiration, heart rate, and blood pressure.

In formaldehyde prepared specimens of brain, the superficial, outer parts appear grey, while the deeper, inner parts are white. The different colours

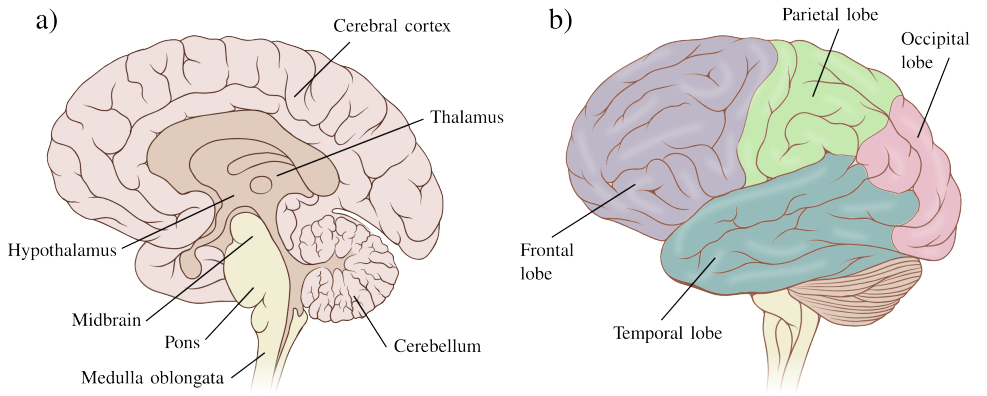

Figure 1: a) Regions of the human brain, lateral view. b) Lobes of the cerebral cortex, sagittal section. Adapted from Wikimedia Commons. [1]

are due to the different cell types present. The grey matter contains the neuronal cell bodies, glial cells and unmyelinated axons, whereas the white matter appears lighter due to the presence of myelinated axons and fewer cell bodies. The grey matter includes regions of the brain involved in muscle control, and sensory perception, while the white matter connects different parts of the grey matter and controls communication *via* nerve impulses between them (Miller et al., 1980). While 20% of all oxygen taken in by the body goes to the brain, 95% of that goes specifically into the grey matter, a recognition its large metabolic function, mainly needed for the maintenance and restoration of ion gradients across cell membranes (Bélanger et al., 2011).

1.1.2 *Neurovascular Unit*

The brain tissue comprises multiple heterotypic cells. Studies over the last decades indicate that neurons (NEs), astrocytes (ACs), SMCs and endothelial cells (ECs) constitute a functional unit, dynamically performing together with

1 https://commons.wikimedia.org

the primary purpose of maintaining homeostasis in the cerebral microcirculation (Iadecola, 2004; Hamel, 2006; Attwell et al., 2010; Drewes, 2012). NEs are connected to each other by synapses forming a synaptic cleft (SC) that is used for information exchange, e.g. *via* neurotransmitters. ECs form the wall of blood vessels creating the blood brain barrier (BBB), the interface for blood-tissue exchange. Arteries and arterioles are surrounded by SMCs which provide a contractile force to regulate the vessel diameter and hence the blood flow. ACs form a complex network surrounding neuronal synapses and blood vessels with their foot processes (Abbott et al., 2010). Zoppo and Mabuchi (2003) were the first to collectively call this assembly of cells an NVU. It highlights the intimate functional relationships between these cells as an interconnected, interactional system (Iadecola, 2004; Witthoft et al., 2013). A schematic representation of it is given in Figure 2.

Cells are filled by the cytoplasm, a thick solution of water, proteins and salts, and are enclosed by the cell membrane. Salt forms electrically charged solute ions that are contained in the cytosol and in the extracellular fluid (ECF) in high concentrations. Water molecules surround them and can form several spherical layers, which is called hydration. An important form of communication between cells is achieved by ion exchange (Ackerman and Clapham, 1997).

Each of the highly specialised cell types has its defined functionality and is in close relationship, and constantly communicates with, its adjacent cells. Interactions with other cells are essential for their functioning.

1.1.2.1 *Neurons*

The human brain contains approximately 100 billion neurons, which are connected to each other through over 100 trillion synapses. They form complex neural circuits sending and receiving information, within, to and from the

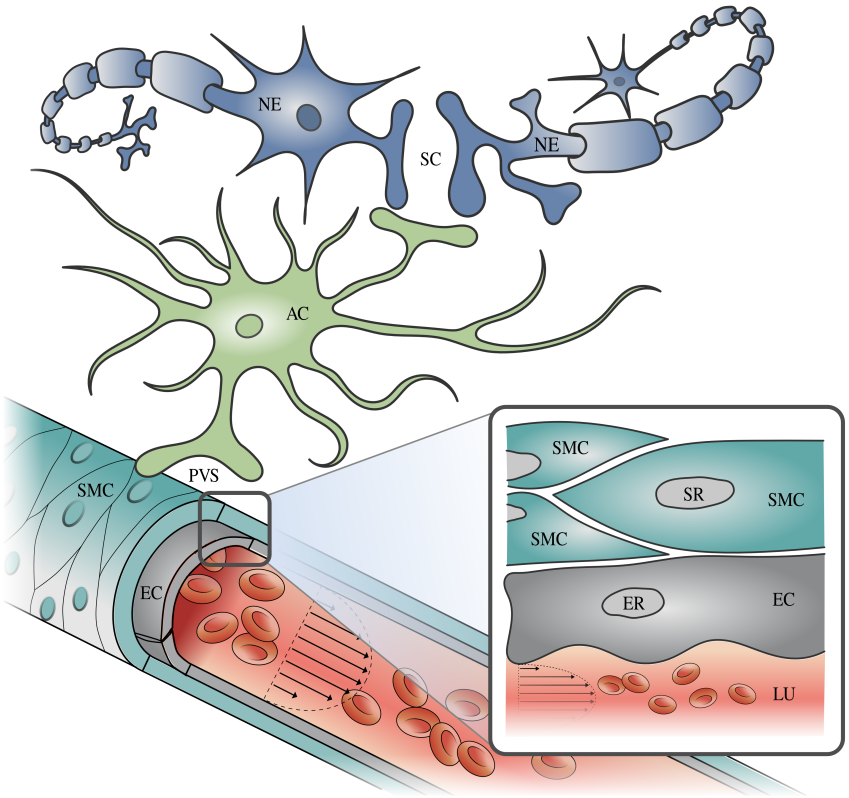

Figure 2: The neurovascular unit consisting of neuron (NE), astrocyte (AC), smooth muscle cell (SMC) and endothelial cell (EC). SC - synaptic cleft, ER - endoplasmic reticulum, PVS - perivascular space, SR - sarcoplasmic reticulum, LU - lumen with indicated blood flow.

brain. Each neuron receives and processes information entering from adjacent NEs in the circuit and then sends out signals at the opposite end. Once these circuits are established during development they remain relatively constant throughout the whole life. The only exception is the hippocampus, where neurogenesis (birth of neurons) occurs and which constantly replaces parts of the circuit (Berridge, 2012).

The central part of the neuron is the cell body (soma), which contains many organelles, such as the nucleus, the Golgi apparatus, the mitochondria and the endoplasmic reticulum. Tapering, typically branching extensions from the soma are called dendrites and are specialised for receiving signals from other neurons and the environment. The axon, a single, up to

a few hundred micrometre long cylindrical extension from the soma, transports electrochemical signals to their targets like other neurons in the brain, spinal cord, autonomic ganglia, and effector cells in muscles and glands throughout the body (Purves et al., 2008; Ramachandran, 2002).

Neurons communicate *via* nerve impulses, also called action potentials, which are short-term reversible fluctuations in membrane potential. The axon of many neurons is covered with myelin, a fatty insulating layer derived from the cell membranes of glial cells, which acts as insulation. Myelinated axons show a higher conduction of action potentials, because they jump from myelin-free gap to gap, called the nodes of Ranvier (Purves et al., 2008).

The end of an axon branches into several terminals, also called synaptic endings or terminal boutons. The most abundant type of synapse in the nervous system is a chemical synapse, which releases neurotransmitter molecules from secretory organelles, synaptic vesicles, to communicate with other cells (another type, called an electrical synapse, is not further considered in this research). The neurotransmitters released from synaptic vesicles modify biochemical dynamics of the target cell by binding to postsynaptic receptors (Purves et al., 2008).

1.1.2.2 *Astrocytes*

In the last century, ACs, stellate neuroglial cells, were considered to be passive cells whose main function was to provide structural support for neurons. However, it is now known that ACs play an important role in maintaining the neuronal environment (Kimelberg, 2004; Wang and Bordey, 2008; Carmignoto and Gómez-Gonzalo, 2010). The ACs' peripheral terminals surround the SCs of NEs and other ACs. The end-feet of the ACs are located in a layered fashion around vascular SMCs. One important function of the ACs

is their ability to buffer extracellular K^+ and other neurotransmitters. These buffered ions can be taken up and transported to the end-feet of the ACs and released into the perivascular space (PVS) and subsequently taken up by the SMCs of the perfusing arteriole.

In addition, ACs themselves seem to have key roles in central nervous system disorders from neuropathic pain and epilepsy to neurodegenerative diseases such as Alzheimer's Disease (AD) as well as schizophrenia, depression, and other psychiatric disorders. ACs are known to interact extensively with neuronal brain elements as well as the vasculature to form functional compartments controlling communication pathways (Østby et al., 2009).

In the brain, ACs greatly outnumber neurons, often 10:1, and occupy 25% to 50% of brain volume.

1.1.2.3 *Smooth Muscle Cells*

The outer layer of the arteriole consists of SMCs usually occupying ca. 90% of the arterial vessel wall, which are the contractile units of the vessel. All SMCs are aligned in a circumferential direction, causing either a diameter decrease or increase when the muscle contracts or relaxes. Similar to other muscles, contraction of the SMCs occurs by actin and myosin filaments forming cross bridges, but it lacks the striations characteristic of cardiac and skeletal muscle. The contractile function of SMCs is not under voluntary control. The rate of contraction is primarily dependent on the cytosolic Ca^{2+} concentration. Ca^{2+} interacts with the Ca^{2+}-binding messenger protein calmodulin (an abbreviation for 'Ca^{2+}-modulated protein') and stimulates the phosphorylation of the myosin light chain (MLC) (Hai and Murphy, 1988; Webb, 2003; Zlokovic, 2005).

1.1.2.4 *Endothelial Cells*

The endothelial cells form a monolayer on the luminal side of the vessel in which their surfaces are aligned perpendicularly to the direction of the flow. This layer, called the endothelium, prevents passive diffusion of bigger molecules, while small molecules such as O_2 can pass through. It can also sense wall shear stress (WSS) induced by the blood flow (Attwell et al., 2010). Together with the SMC layer the ECs form the BBB, the physical frontier which protects the brain from unwanted chemical substances in the blood.

1.1.3 *Cerebral Vasculature*

The four main arteries supplying the brain are two pairs of internal carotid arteries and vertebral arteries (see Figure 3a)). They deliver oxygenated blood and glucose to the brain while a network of veins remove carbon dioxide and metabolic products. The ring structure that connects the two internal carotid artery and the vertebrobasilar circulation by communicating arteries is called the cerebral arterial circle (or 'Circle of Willis' after Thomas Willis, 1621-1675, who gave a very detailed anatomic description of it) (Vrselja et al., 2014). It is located at the base of the brain and serves as the distribution point for arteries of the cerebral hemispheres, brainstem and cerebellum. From these distributing arteries smaller arteries arise and course to the surface of the brain running within the subarachnoid space, called pial arteries (see Figure 3b)). Penetrating or intracerebral arteries branching off pial arteries enter the brain tissue at right angles to its surface. They are separated from the brain by Virchow-Robin spaces. Then, they branch into numerous smaller arteries and arterioles within the cerebral parenchyma and termin-

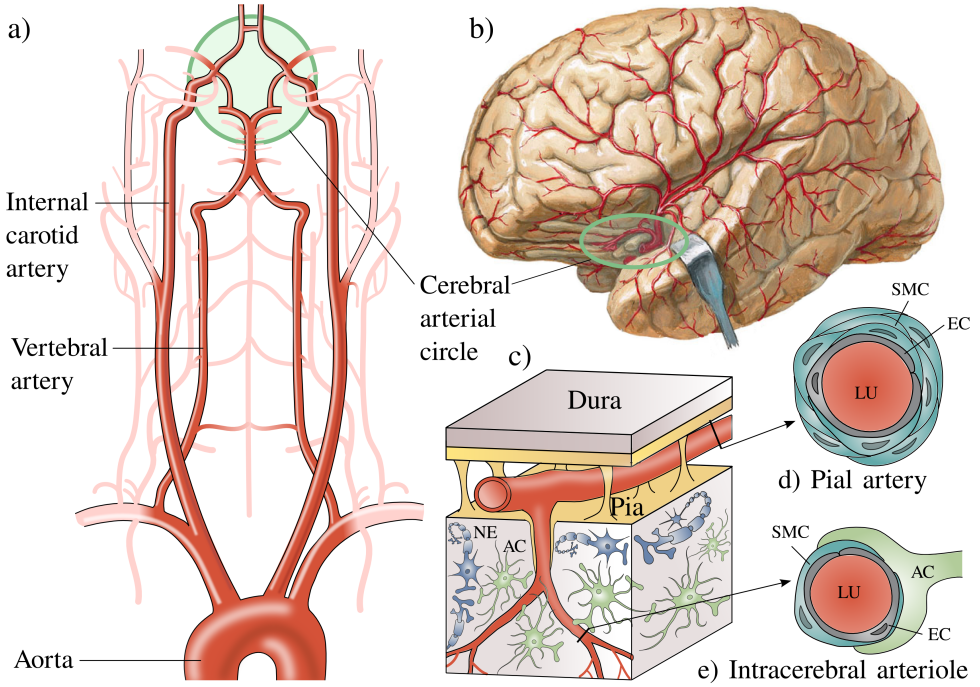

Figure 3: Different levels of cerebral vasculature system. a) Arteries to the brain. The main supplying arteries are represented in darker colour. The cerebral arterial circle (CAC) is marked in green. b) Pial arteries lie on the cerebral surface distributing blood from the CAC (marked in green). c) Penetrating arteries and arterioles orthogonally branch off pial arteries. d) Pial arteries are surrounded by one or two layers of endothelial cells (ECs) and multiple layers of smooth muscle cells (SMCs) and no astrocyte endfeet. e) Intracerebral arterioles only exhibit one layer of ECs and SMCs. Additionally, astrocytic endfeet are in close proximity to arterioles. Adapted from Netter (2014) and Zlokovic (2011).

ate as capillary beds. Capillary plexuses drain into intracerebral venule and vein systems (Zlokovic, 2005; Pantoni and Gorelick, 2014).

1.2 NEUROVASCULAR COUPLING

The concept of cerebral blood flow regulation by neuronal activity has been investigated with much interest (Butler and Nicholsson, 2003). Traditionally, it was thought that an increase in blood flow was triggered by a metabolic signal such as lower O_2 or glutamate (Glu) or a higher carbon dioxide (CO_2)

level in the blood. However recently, neurotransmitter-mediated signalling has been discovered to play a major role in regulating the blood flow *via* changes in arterial diameter.

Functional hyperæmia or neurovascular coupling (NVC) describes the local vasodilation and contraction due to neuronal activation (vasoreactivity). The change in the vessel diameter controls the blood flow and thereby the cerebral supply of O_2 and nutrients.

Each cell type plays an important specific role during the process of NVC. Communication between cells is based on an exchange of ions through pumps and channels. These ion fluxes contribute to changes in cytosolic and intercellular species' concentrations and cell membrane potentials.

There are manifold direct and indirect clearly defined signalling pathways at a molecular level that adjust local perfusion (Lok et al., 2007; Berridge, 2012). They are mediated by different signalling molecules, such as K^+, Ca^{2+}, epoxyeicosatrienoic acid (EET), arachidonic acid (AA), 20-hydroxyeicosatetraenoic acid (20-HETE) and nitric oxide (NO). Neurotransmitters are released by the NE into the SC and can bind to receptors at dendrites of other NEs and ACs. This leads to a cascade of chemical reactions and the opening and closing of ion channels which influences ion fluxes and concentrations.

The multicellular signalling between the neuronal and the vascular system is essential for the finely regulated blood supply needed for normal cerebral functioning (Quaegebeur et al., 2011).

1.3 MOTIVATION

Our understanding of the human brain is constantly deepening. However, crucial coherences and signalling pathways remain undiscovered. The reason

for the onset of many cerebral diseases and neurodegenerative conditions are still poorly understood and need to be further investigated in order to provide possible preventions and therapeutic strategies.

Research findings within the last decades have suggested that there exists a stronger link between cerebral function and vascular perfusion of the brain than previously thought (Girouard and Iadecola, 2006; Zlokovic, 2011; Aoi et al., 2012).

Many neurologic pathologies, such as hypertension, AD, cortical spreading depression, atherosclerosis and stroke, are associated with impaired NVC (Iadecola, 2004; Girouard and Iadecola, 2006; Zlokovic, 2011; Drewes, 2012). All of these pathologies exhibit an altered relationship between neural activity and the cerebral blood flow (CBF). These alterations affect the delivery of O_2 and nutrients to active brain cells and impair the removal of waste products from cerebral metabolism (Zlokovic, 2005). It is likely that this disruption contributes to brain dysfunction and therefore, it is crucial to fully understand the underlying cellular and biochemical mechanisms – both in the healthy as well as in the pathological brain.

AD is the most common form of dementia, a progressive neurodegenerative disease, and its prevalence increases dramatically as the global population ages (see Figure 4a)). Most cases of AD are sporadic, meaning that they are not genetically inherited, and therefore can be therapeutically addressed. AD patients exhibit characteristic senile plaques, neurofibrillary tangles, and neuronal loss (Zhang and Le, 2010). Plaques are formed by depositions of amyloid-β (A-β) peptides in the cerebral tissue and blood vessels (Girouard and Iadecola, 2006).

Interestingly, the accumulation of A-β in AD patients occurs at a pre-symptomatic stage, before cognitive impairment is observed (see Figure 4b)). Elucidating the onset of this accumulation on a molecular and cellular basis

is important for novel therapeutic strategies. Recent studies suggest moving away from the traditional "neuroncentric" view of AD towards a neurovascular hypothesis (Zlokovic, 2005; Girouard and Iadecola, 2006; Zlokovic, 2011). There is increasing evidence that vascular factors have a causal role in the pathological development of AD (Attwell et al., 2010).

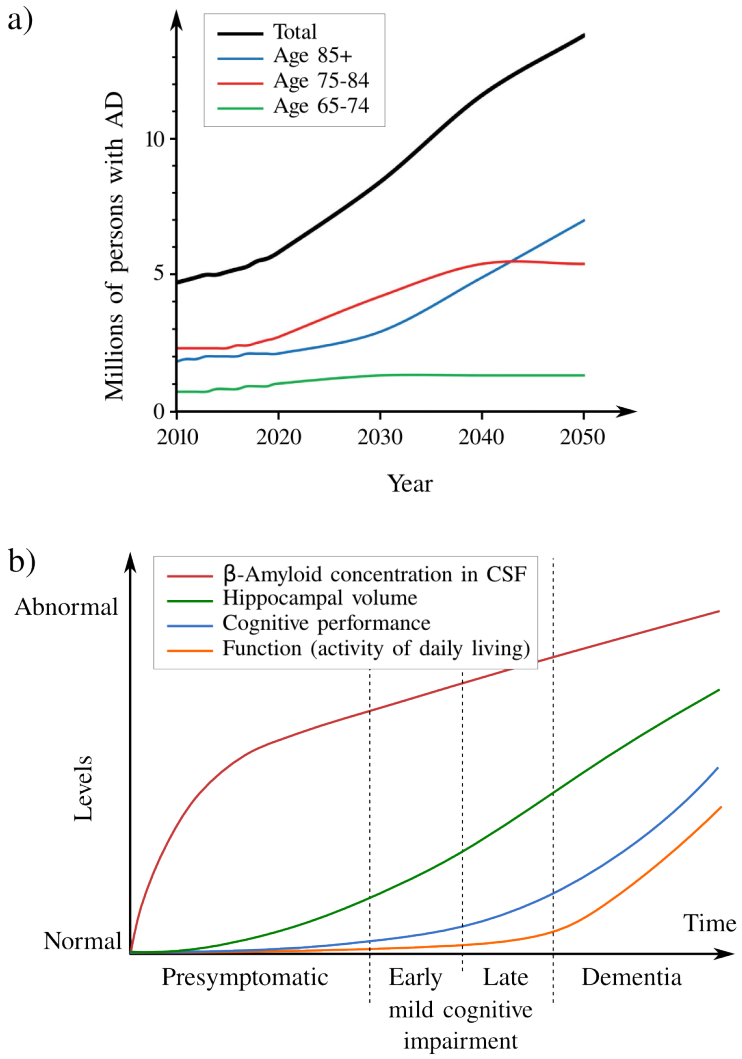

Figure 4: a) Estimated number of people with Alzheimer's Disease (AD) in the U.S., projections through 2015, adapted from Hebert et al. (2013). b) Progression of pathological and clinical events in AD, adapted from Petersen (2010)

The NVU is profoundly altered in AD patients ECs and SMCs are damaged and the number of microvessels is reduced (Girouard and Iadecola, 2006). Additionally, vessels show increased contractility and resting CBF is reduced (Bell and Zlokovic, 2009; Attwell et al., 2010). This may reduce A-β clearance *via* the BBB and promote ischæmic lesions, which exacerbate the dementia (Girouard and Iadecola, 2006).

The aim of the presented work is to provide a numerical model of the regulated blood supply with connected cells for the whole brain, which includes the complex cell-to-cell signalling in the NVU. We want to investigate the effect signalling molecules have on the NVC mechanism and how they are disturbed from their non-pathological equilibrium.

This research will reveal new insights into the NVC mechanism on a cellular and molecular basis. Computational models of several NVC pathways will be developed, which will facilitate the simulation of healthy and pathological scenarios. Results of such simulations provide a means for investigating NVC mechanisms in a non-invasive way, thereby overcoming the limitations of physiological experiments.

2

METHODOLOGY - MATHEMATICAL MODELLING IN CELL BIOLOGY

The development of mathematical models to help the understanding of physiological processes has been a known practice for over a century (e.g. Hodgkin and Huxley (1952), who modelled the basic mechanisms of action potentials in the squid giant axon). Mathematical and computational models can be powerful tools to analyse and predict physiological processes (Keener and Sneyd, 2009). Despite the fact that the interdisciplinary work between physiology and applied mathematics (like between any other two disciplines) bears complications due to barriers to communication, this field of research becomes increasingly important for the comprehensive understanding of normal and pathological situations as well as for the guidance of future key experiments (Keener and Sneyd, 2009).

2.1 MODEL COMPARTMENTS

Cells and spatial domains of the NVU like the SC or extracellular space (ECS) can be represented as virtual compartments (see Figure 13). They are assumed to have a homogeneous distribution of species, i.e. any measurable entity like ions, such as molecules and enzymes, inside. This so-called lumped parameter approach assumes that spatial gradients within the compartment are negligible. Therefore, every variable in each compartment has

only one specific value at a certain point in time, which simplifies the mathematical description of the physiological processes and will be applied for the development of our NVU model.

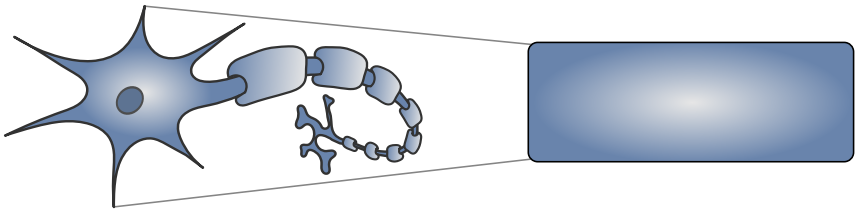

Figure 5: A cell can be modelled by a compartment with homogeneous concentration of species, depicted as spheres (lumped parameter approach).

2.1.1 *Molar Concentration*

Molecular concentration or molarity describes the amount of a solute, n (in moles), divided by the volume, V, of the mixture within one model compartment:

$$c = \frac{n}{V} \,. \tag{2.1}$$

n measures the size of an ensemble of elementary entities, such as atoms, molecules, electrons, and other particles and is proportional to the number of elementary entities present:

$$n = \frac{N}{N_A} \,, \tag{2.2}$$

where N_A is the Avogadro constant, approximately $6.022 \times 10^{23}\,\mathrm{mol}^{-1}$.

The SI unit of c is $\mathrm{mol/m^3}$, but more commonly the unit mol/L is used, typically denoted by a capital letter M ('molar'). Most concentrations of ions appearing in this work are of the order of magnitude of 1×10^{-6} M and are hence expressed in µM.

2.1.2 *Mass Conservation*

Inside each compartment in the NVU model the physical law of mass conservation, or in our case 'conservation of species', can be applied. It implies that the rate of change of a certain species' concentration is equal to the amount of species entering (influx, J_{in}) minus the amount leaving the compartment (efflux, J_{out}). For example, the differential equation for the rate of change of calcium concentration, $[Ca^{2+}]$, in a model compartment reads as follows:

$$\frac{d[Ca^{2+}]}{dt} = P + (J_{in} - J_{out})\,\gamma_{vol} - R\,, \tag{2.3}$$

where P is a production term, R a reaction term and γ_{vol} is the volume ratio between the compartment and the external space. A schematic representation can be found in Figure 6.

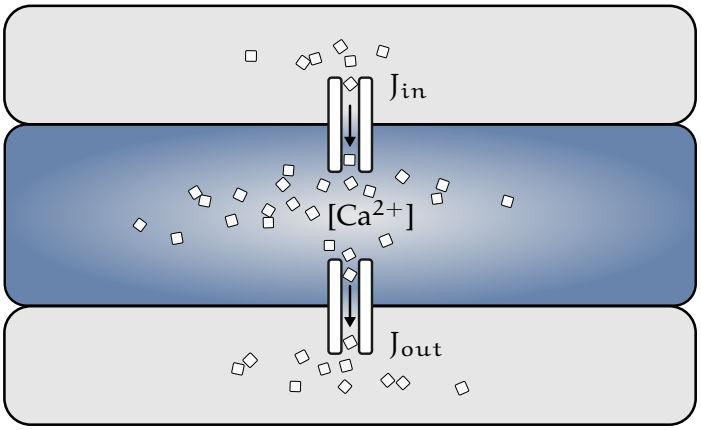

Figure 6: 'Conservation of species' in a model compartment. For example, the rate of change of calcium concentration, $[Ca^{2+}]$, in the compartment is equal to the amount of Ca^{2+} ions (represented by small squares) entering and leaving it through ion channels.

2.2 ENZYME KINETICS AND SUBSTRATE BINDING

Substrate binding, as it happens in the buffering processes of ions or ligands binding to ionotropic receptors, is one of the most common reversible reactions in biochemistry.

More complex biochemical reactions are often catalysed by enzymes, E, which are mostly proteins. They help and accelerate the conversion of substrates, S, into products, P, without being changed themselves by the reaction:

$$S + E \longrightarrow P + E \tag{2.4}$$

This enzymatic catalysis typically is a two-state reaction: First, S reversibly reacts with E to form a substrate-enzyme complex, SE. This then decomposes into P releasing the original enzyme in the process:

$$S + E \underset{k_b}{\overset{k_f}{\rightleftharpoons}} SE \tag{2.5}$$

$$SE \xrightarrow{k_{cat}} P + E \tag{2.6}$$

with the forward and backward reaction rates, k_f and k_b, respectively, and the catalysis rate, k_{cat}. The second step, which is known to determine the overall reaction rate, is assumed to be non-reversible as P is continually re-

moved preventing the reverse reaction from occurring. Mass conservation gives:

$$\frac{d[S]}{dt} = k_b[SE] - k_f[S][E] \tag{2.7}$$

$$\frac{d[E]}{dt} = k_b[SE] - k_f[S][E] + k_{cat}[SE] \tag{2.8}$$

$$\frac{d[SE]}{dt} = k_f[S][E] - (k_b + k_{cat})[SE] \tag{2.9}$$

$$\frac{d[P]}{dt} = k_{cat}[SE] \tag{2.10}$$

with the initial conditions $[E](0) = E_0$, $[S](0) = S_0$ and $[SE](0) = [P](0) = 0$. The total concentration of enzyme, $[E]_T$, is conserved:

$$[E]_T = [E] + [SE] \, . \tag{2.11}$$

Usually, the enzyme concentration is significantly lower than the substrate concentration, which limits the reaction rate and leads to non-linear behaviour.

2.2.1 *Michaelis-Menten Kinetics*

Michaelis and Menten (1913) proposed a model of enzyme kinetics explaining the non-linear behaviour of the reaction rate, relating it to the concentration of substrate, $[S]$, (Keener and Sneyd, 2009).

The SE concentration (Equation 2.9) will rapidly approach a steady-state value and can be assumed constant (steady-state approximation, Briggs (1925)). Therefore

$$\frac{d[SE]}{dt} = 0 = k_f[S][E] - (k_b + k_{cat})[SE] \, . \tag{2.12}$$

Rearranging gives:

$$k_f[S][E] = (k_b + k_{cat})[SE] \; . \tag{2.13}$$

Applying Equation 2.11 we get:

$$k_f(E_0 - [SE])[S] = (k_b + k_{cat})[SE] \tag{2.14}$$

$$[SE] = \frac{k_f E_0[S]}{k_b + k_{cat} + k_f[S]} \tag{2.15}$$

So, the reaction rate, ν, which is the rate at which P is released from the substrate-enzyme complex (Equation 2.10) can be written as:

$$\nu = \frac{d[P]}{dt} = \frac{V_{max}[S]}{K_M + [S]}. \tag{2.16}$$

Here, $V_{max} = k_{cat}E_0$ represents the maximum rate achieved by the system, at saturating substrate concentrations. $K_M = (k_b + k_{cat})/k_f$ is the Michaelis constant, which corresponds to the concentration of substrate at which ν is at half-maximum (see Figure 7).

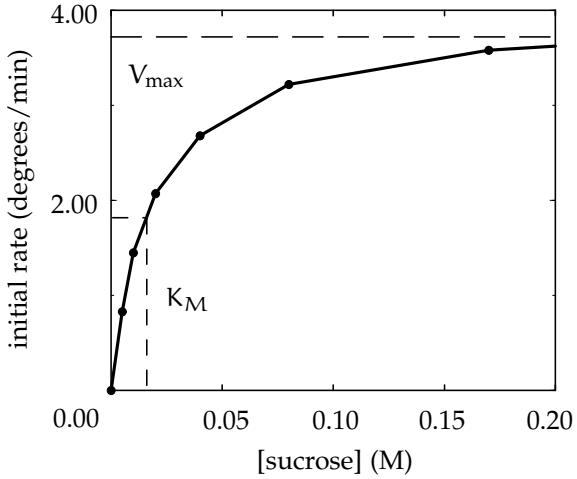

Figure 7: Experimental rate of loss of optical activity of sucrose for fixed initial concentrations of sucrose and of the enzyme. The initial rate of the invertase-catalysed reaction plotted as a function of sucrose concentration. Data of Michaelis and Menten (1913), figure adapted from Fall et al. (2002).

2.2.2 *Hill Equation*

For many enzymes, the reaction rate has a more sigmoidal than simple hyperbolic character as originally proposed by Michaelis and Menten (1913). Here, cooperative effects take place, in which the binding of single substrate molecules affect the binding of subsequent ones and Equation 2.5 can be modified as follows:

$$n[S] + [E] \underset{k_b}{\overset{k_f}{\rightleftharpoons}} [S_n E] \tag{2.17}$$

where n is the Hill coefficient, i.e. the total amount of binding sites on the enzyme for the substrate.

The resulting reaction rate, v, is described as:

$$v = k_f[S]^n[E] - k_b[S_n E] \tag{2.18}$$

When equilibrium is reached, $v = 0$:

$$[S_n E] = \frac{k_f}{k_b}[S]^n[E] \; . \tag{2.19}$$

This can be used to find an expression for θ, the fraction of bound sites with respect to all available binding sites:

$$\theta = \frac{[S_n E]}{[E] + [S_n E]} \; . \tag{2.20}$$

With Equation 2.19 we get:

$$\theta = \frac{\frac{k_f}{k_b}[S]^n[E]}{[E] + [S_n E]} = \frac{[S]^n}{\frac{k_b}{k_f} + [S]^n} \; . \tag{2.21}$$

The characteristic behaviour of the Hill equation depends on the apparent dissociation constant, $K_d = \frac{k_b}{k_f}$, and the Hill coefficient, n.

Note that the Hill equation is also used to describe other biochemical processes in which the Hill coefficient refers to other biological properties or is a fitting parameter in order to match experimental data.

For cooperative binding behaviour, three cases can be distinguished:

- $n = 1$ - non-cooperative binding: The amount of bound sites does not influence current binding rate.
- $n > 1$ - positively cooperative binding: An increasing amount of bound sites increases the rate of binding.
- $n < 1$ - negatively cooperative binding: The binding rate decreases when the amount of bound sites increases.

2.3 CELL MEMBRANE

The interior of a cell is separated from its environment (extracellular fluid) by a membrane. It consists of a phospholipid bilayer with proteins, water-filled and protein-lined pores, called ion channels, embedded in it and is approximately 7.5 nm thick. It is selectively permeable to ions and molecules and controls their movement in and out of cells.

At equilibrium there are substantial concentration differences for many species between the interior and the exterior of a cell. This gradient is maintained by energy-consuming transporters that pump chemical species against their electrochemical gradient. The most common and important ion pumps in cells are adenosine triphosphate (ATP)ase pumps, which occur on endoplasmic reticulums (ERs) and in cell membranes and which extract energy from the hydrolisis of ATP to adenosine diphosphate (ADP) molecules (Keener and Sneyd, 2009).

2.3.1 *Nernst Membrane Potential*

The voltage difference between the two sides of the membrane results in a non-zero membrane potential (also transmembrane potential or membrane voltage). This is important for the generation and transmission of electrical signals between different parts of the cell, e.g. action potentials along the axon of a neuron.

The equilibrium potential is called reversal or Nernst potential, V_{Nernst} (Fall et al., 2002). It is derived from the Gibb's free energy, G, which is the free enthalpy of the system. When one mole of ions of valence z is moved across a membrane, G changes as follows:

$$\Delta G = -RT \ln\left(\frac{[ion]_{out}}{[ion]_{in}}\right) + \Delta V F z \,, \tag{2.22}$$

where R, T and F are the gas constant, temperature and Faraday's constant, respectively.

At equilibrium, when electrical and osmotic forces are balanced, ΔG is zero. Rearranging gives the Nernst potential:

$$\Delta V = V_{Nernst} = \frac{RT}{zF} \ln\left(\frac{[ion]_{out}}{[ion]_{in}}\right) \tag{2.23}$$

When the actual membrane potential differs from the Nernst potential, a convergent rectifying diffusion flux tries to bring the membrane potential back to the Nernst potential. Kirchhoff's current law gives:

$$\frac{dV_{ion}}{dt} = \frac{g_{ion}}{C_{cell}}(V_{Nernst,ion} - V_m) \,, \tag{2.24}$$

where g_{ion} is the ion conductance, C_{cell} the capacity of the cell and V_m the membrane potential of the cell.

2.3.2 *Resting Membrane Potential*

The Nernst equation (Equation 2.23) allows us to calculate the equilibrium potential for a particular ion under specific concentration conditions. However, the membranes of most cells are permeable to more than one ion. The Goldman-Hodgkin-Katz (GHK) equation, sometimes called the constant field equation, considers the case where there are multiple conductances. It determines the resting membrane potential, at which different ions are entering and leaving the cell, but the net current is zero (Fall et al., 2002). For a cell whose membrane is permeable to K^+, sodium ion (Na^+), and chloride ion (Cl^-) the equation can be written as:

$$V_{GHK} = \frac{RT}{F} \ln \left(\frac{P_K[K^+]_{out} + P_{Na}[Na^+]_{out} + P_{Cl}[Cl^-]_{out}}{P_K[K^+]_{in} + P_{Na}[Na^+]_{in} + P_{Cl}[Cl^-]_{in}} \right) , \tag{2.25}$$

where P_i is the relative permeability for ion i, which can be determined experimentally.

The membrane potential for a cell containing K^+, Na^+, and Cl^- ions is:

$$V_m = \frac{V_K * g_K + V_{Na} * g_{Na} + V_{Cl} * g_{Cl}}{g_K + g_{Na} + g_{Cl}} , \tag{2.26}$$

where V_i is the Nernst or reversal potential for ion i (Equation 2.23) and g_i is the ion-specific conductance of the ion channel (the reciprocal of the resistance).

2.4 DIFFUSION

Molecules move passively from one compartment to another by diffusion. They can move through either open ion channels or gap junctions, and when

the molecule is very small also through water-filled pores in the membrane. One example for this is NO, which diffuses freely through cell membranes.

Molecules in gas and fluids constantly move, which is called Brownian motion. The two main driving forces for diffusion from one compartment to another are concentration gradients and electrical charge. Typically, there is a concentration *and* potential difference across the membrane (Fall et al., 2002).

Ficks's law of diffusion due to concentration difference states ions move from compartments with high concentration to compartments with low concentration, at a rate proportional to the concentration gradient. The resulting ion flux, J_i, is dependent on the diffusion distance, x, and time:

$$J_i(x,t) = -D_i \frac{\partial}{\partial x}[i](x,t) \; . \tag{2.27}$$

Here, D_i is the ion-and-medium-specific diffusion coefficient and $[i]$ the molar concentration of ionic species 'i'.

Additionally to the concentration-difference-induced ion motion, the potential difference across the membrane, $\Delta\phi$, influences the ion flux. The Nernst-Planck equation describes ion movements due to both the concentration gradient and the potential gradient:

$$J_i = -D_i \left(\frac{\partial [i]}{\partial x} + \frac{z_i F}{RT}[i] \frac{\partial \phi}{\partial x} \right) \tag{2.28}$$

For the ion flux through an ion channel of a given length, L, in steady state Equation 2.28 can be applied. For simplification, the potential gradient is assumed to be constant (Fall et al., 2002):

$$\frac{d\phi}{dx} = \frac{\Delta\phi}{L} \tag{2.29}$$

with

$$\Delta\phi = \phi(0) - \phi(L) \, . \tag{2.30}$$

The ion flux, J_i, through the channel can be determined as:

$$J_i = -\frac{D_i}{L}\frac{zFV}{RT}\left(\frac{c(L) - c(0)\exp(-\frac{zFV}{RT})}{1-\exp(-\frac{zFV}{RT})}\right) \, . \tag{2.31}$$

J_i can be converted to an ionic current I_c by multiplying by zF.

2.5 ION CHANNEL OPEN PROBABILITY

An ion channel is a specialised pathway that allows the passive transport of ions (see Equation 2.31). The opening and closing of ion channels is accomplished in different ways, known as gating (Purves et al., 2008).

- Voltage-gated ion channel - opens and closes in response to the membrane potential.
- Ligand-gated ion channel - directly linked to an ionotropic receptor and opens and closes in response to transmitter-binding (e.g. Glu, gamma-aminobutyric acid (GABA)).
- Mechanosensitive ion channel - opens and closes in response to mechanical stretch, pressure or shear (e.g. due to blood flow in the vessel).
- Second-messenger-activated ion channel - e.g. by intracellular ions.

A mathematical prediction of the average behaviour of many individual channels of a channel type is the open probability.

An ion channel can be in either of two conductance states: a closed state, c, or an open state, o. Kinetic transitions between the two states can be described with the rate constants k^+ and k^- (Fall et al., 2002):

$$c \underset{k^-}{\overset{k^+}{\rightleftharpoons}} o \ . \tag{2.32}$$

The fraction of channels in the open state, f_o , is defined as:

$$f_o = \frac{n_o}{n_o + n_c} \ , \tag{2.33}$$

where n_o and n_c refer to the total number of channels in the open and the closed state, respectively.

The flux from the open to the closed state, j_-, is proportional to the number of open channels and can be written as:

$$j_- = k^- f_o \ . \tag{2.34}$$

In a similar fashion and with $f_o + f_c = 1$ the reverse flux, j_+, is determined by

$$j_+ = k^+ f_c = k^+ (1 - f_o) \ . \tag{2.35}$$

Then

$$\begin{aligned} \frac{df_o}{dt} &= j_+ - j_- = k^+(1 - f_o) - k^- f_o \\ &= (k^+ - k^-) \left(f_o - \frac{k^+}{k^- + k^+} \right) \ . \end{aligned} \tag{2.36}$$

Let

$$\tau = \frac{1}{k^- + k^+} \ ; \ f_\infty = \frac{k^+}{k^- + k^+} \ , \tag{2.37}$$

then

$$\frac{df_o}{dt} = \frac{f_\infty - f_o}{\tau} \ , \tag{2.38}$$

where f_∞ is the equilibrium state open probability at a certain point in time and can be a function of other variables. The time constant τ gives an indication of the speed at which f reaches its steady state value, which can also depend on other variables (Fall et al., 2002).

2.6 NUMERICAL SOLVING METHODS

Systems of non-linear differential equations for the rate of change in cellular properties are often difficult or impossible to solve exactly using analytical techniques. Computational numerical analysis has made the solving of non-linear coupled systems of ordinary differential equations (ODEs) fast, accurate, and relatively easy (Fall et al., 2002). ODE solvers use a combination of implicit and explicit iterative methods, such as the Euler method or extended versions of it.

It can be useful to scale the model using characteristic dimensional quantities and relate the system to them. This non-dimensionalisation provides a way to determine the relative magnitudes of independent parameters of the system (parameter sensitivity). It also usually reduces the number of parameters, thereby leading to a significant simplification (Logan, 2013).

3

REVIEW OF EXISTING MATHEMATICAL MODELS

Over the past two decades several mathematical models have been developed to describe basic biochemical mechanisms and pathways within components of the NVU and the cerebral vasculature.

These models are based on physical, hæmodynamical and electrical laws paired with often very fundamental experiments and have been elucidating the role of certain cells and pathways in components of NVC. Our research group makes use of existing models, develops them further and combines different aspects of them to create new models. It is also an important part of research to analyse the work of others in a critical way and, where necessary, correct parts of it. The fact that some models, including ours, cannot correctly predict some physiological phenomena shows that we do not understand everything and emphasises the need for further research.

3.1 MODELS OF A NEUROVASCULAR UNIT

The NVU is comprised of many interconnected cell types with complex information exchange. Few mathematical models of a full NVU have been previously described. However, there are multiple models published that focus on parts of the NVU. By adding these segments together in a meaningful way and extending them, we can obtain a model of the whole NVC process.

3.1.1 *Neuron and Astrocyte*

NEs and ACs are the most numerous cell types in the brain. Information transmission in neuronal networks through electrical and chemical signals are essential for cerebral functioning.

ACs play an important role in maintaining the neuronal environment and interact with NEs on many different levels. They surround nearly all neuronal synapses with their processes. NEs and ACs are not connected to one another through gap junctions (GJs) as SMCs and ECs are, but use the narrow SC space between them for interactions (Magistretti and Ransom, 2002; Carmignoto and Gómez-Gonzalo, 2010).

ACs influence the ions, energy metabolites and neurotransmitters of the SC between two NEs. One of the best-established functions of ACs is the regulation of extracellular K^+, which is rapidly increased during neuronal activity. Uptake and redistribution of SC K^+, so-called spatial buffering, through ACs is essential for K^+ homeostatic control, because diffusion alone could not dissipate K^+ released from NEs fast enough (Magistretti and Ransom, 2002).

K^+ is taken up by the AC through two types of cotransporters, a subcategory of membrane transport proteins, namely Potassium chloride cotransporter type 1 (KCC1) and sodium-potassium-chloride cotransporter type 1 (NKCC1), that cotransport K^+ and Na^+ ions with Cl^- ions into the AC (Magistretti and Ransom, 2002; Østby et al., 2009).

Chang et al. (2013) presented a detailed biophysical NE model. The research group studied the pathological electrical, ionic, and metabolic disturbances in the grey matter of the brain that occur during cortical spreading depression (CSD). A mathematical model of the neuronal intracellular space (divided into two compartments, soma and dendrite), the ECS, and the vascular space is presented. The astrocytic K^+ buffering is modelled by

a simplified flux that accurately reproduces the K^+ dynamics of Farr and David (2011).

The model omits an axon domain, which does not influence their research findings, but could be an important component of models for information transduction in neuronal networks.

Furthermore, the Chang et al. model does not include Ca^{2+} dynamics in the NE. It is shown, however, that Ca^{2+} is an important signalling molecule and has influence on a wide range of intracellular processes in normal and pathological conditions. These include the release of transmitters, synaptic plasticity, activation of ion channels and intracellular Ca^{2+} store dynamics (Schutter and Smolen, 1998). There are indications that dysfunction of the NVU and disruption of the equilibrium of cytosolic Ca^{2+} in both the NEs and ACs are implicated in the pathogenesis of AD (Kuchibhotla et al., 2009). Additionally, LaFerla (2002) emphasised the destabilisation of neuronal Ca^{2+} homeostasis in the ER arising from altered amyloid precursor protein (APP) processing and increased A-β concentrations, typically associated with Alzheimer's Disease. Kuchibhotla et al. (2009) observed elevated resting astrocytic Ca^{2+} levels and intercellular Ca^{2+} waves in mice with A-β plaques.

Against this background the inclusion of a detailed biophysical model for the Ca^{2+} dynamics in the NE and AC with special focus on ER signalling mechanisms seems essential for studying Ca^{2+} signal-transduction cascades in the normal and in the AD brain.

An implementation of a rather simple Ca^{2+} model for the NE is carried out by Santucci and Raghavachari (2008), who model Ca^{2+} influx into the neuron through ionotropic N-methyl-D-aspartate receptors (NMDA-Rs). These are receptor complexes including transmembrane ion channels in the NE that are opened or closed in response to the binding of Glu (Benarroch, 2006).

In contrast to this, a very detailed neuronal Ca^{2+} model was presented by Schutter and Smolen (1998). One of its main features is that it includes an ER, which seems of essential importance as it is believed that Ca^{2+} release from this intracellular Ca^{2+} store plays an important role in excitable cells (Mattson et al., 2000). Ca^{2+} is released from the ER through inositol trisphosphate (IP_3)- and Ca^{2+}-gated channels and is taken up through sarcoplasmic/endoplasmic reticulum calcium-ATPase (SERCA) pumps. The NE exchanges Ca^{2+} ions with the SC through voltage-operated calcium channels (VOCCs) and ionotropic glutamate receptor (iGlu-R) complexes. The physiologically large equilibrium Ca^{2+} concentration gradient between intra- and extracellular space (0.1 µM and 1000 µM, respectively) is maintained by an ATPase pump and a Na^+/K^+ exchanger. The Schutter and Smolen model includes intracellular spatial electro-diffusion of Ca^{2+} and IP_3, hence comprises partial differential equations (PDEs).

Østby et al. (2009) investigate the shrinkage phenomenon of the extracellular space due to K^+ clearance followed by osmotically-driven water uptake by the AC.

Neuronal activity is modelled by a K^+ release from the NE and subsequent uptake by the AC through co-transporters. In the Østby et al. (2009) model the interactions of K^+, Na^+, Cl^- and bicarbonate (HCO_3^-) ions are taken into account. A graphical overview of all ion channels and pumps included in the Østby et al. model is given in Figure 8. Farr and David (2011) include astrocytic Ca^{2+} dynamics in their model, thereby following the model of Lemon et al. (2003) and Bennett et al. (2008). Nevertheless, only intracellular processes are taken into account and the model does not include Ca^{2+} exchange with the extracellular space. The cytosolic Ca^{2+} concentration, $[Ca^{2+}]_k$, is determined by the fluxes from and to the ER.

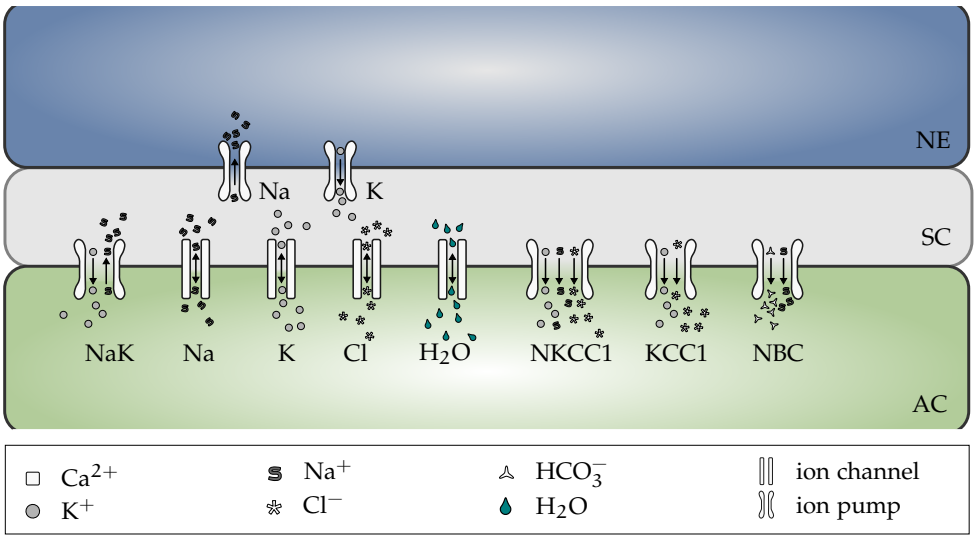

Figure 8: A graphical overview of the Østby et al. (2009) model.

Witthoft and Karniadakis (2012) and Witthoft et al. (2013) included mechanosensitive Ca^{2+} channels (transient receptor potential cation channel subfamily V member 4 (TRPV4)) at the endfoot of the AC. In this model vessel dilation activates TRPV4 channels, allowing an influx of Ca^{2+} from the PVS into the astrocytic cytosol. The channel is inhibited by intra- and extracellular Ca^{2+} concentration, it has a slow decay at a low extracellular and a fast decay at high extracellular Ca^{2+}. However,this is in contrast to the findings of Dunn et al. (2013), where moderate intracellular Ca^{2+} levels activate the TRPV4 channel.

3.1.2 *Smooth Muscle and Endothelial Cell*

The arteriolar vessel wall is formed of a layer of ECs surrounded by one layer of SMCs. The cells exhibit functional GJ contacts among each other (homotypic coupling) and between the two different cell types (heterotypic coupling).

The SMC is a contractile unit of the NVU and therefore directly impacts on the CBF by controlling the vessel diameter. The SMC cytosolic Ca^{2+} stimulates the phosphorylation of the light chain of myosin (for more detailed explanation, see Section 1.1.2.3).

Hai and Murphy (1988) were the first to describe a biophysical model of the contraction mechanism of a muscle cell. The model is validated with data from experiments on stimulated swine carotid artery SMCs (Singer and Murphy, 1987).

They formulated rate equations for all four states of the actin-myosin interactions: free nonphosphorylated cross bridges (M), free phosphorylated cross bridges (Mp), attached phosphorylated cross bridges (AMp) and attached dephosphorylated latch bridges (AM; see Figure 9). The dynamics

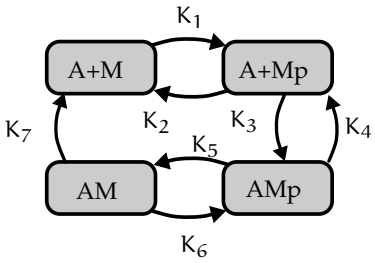

Figure 9: The kinetics of the four states of the actin-myosin interactions as mathematically described by Hai and Murphy (1988). K_1 to K_7 are rate constants, of which K_1 and K_6 are calcium-dependent.

of the fraction of myosin in a particular state is given by four differential equations:

$$\begin{aligned}
\frac{d[M]}{dt} &= -K_1[M] + K_2[Mp] + K_7[AM] \\
\frac{d[Mp]}{dt} &= K_4[AMp] + K_1[M] - (K_2 + K_3)[Mp] \\
\frac{d[AMp]}{dt} &= K_3[Mp] + K_6[AM] - (K_4 + K_5)[AMp] \\
\frac{d[AM]}{dt} &= K_5[AMp] - (K_7 + K_6)[AM]
\end{aligned} \tag{3.1}$$

with

$$[AM] + [AMp] + [Mp] + [M] = 1 \tag{3.2}$$

where the rate constants, K_n $(n = 1, ..., 7)$, regulate the phosphorylation and bridge formation. Note that this system is overdetermined and using equation (3.2) the model only needs to be solved for $[AM]$, $[AMp]$ and $[Mp]$.

One of the main assumptions of the Hai and Murphy (1988) model is that the Ca^{2+}-dependent myosin phosphorylation is the only regulatory mechanism. Yang et al. (2005) reduce the Hai and Murphy (1988) system to a two-state kinetic model and modify it to express the effect that the second messenger cyclic guanosine monophosphate (cGMP) has on MLC activity. The modified MLC dephosphorylation rate constant, K_2, associated with cGMP concentration reads:

$$K_2 = k^b_{mlcp} + k^c_{mlcp} \frac{[cGMP]^{n_H}}{[cGMP]^{n_H} + K^{n_H}_{m,mlcp}}, \tag{3.3}$$

where k^b_{mlcp} and k^c_{mlcp} represent rate constants, K_m is the Michaelis-Menten coefficient, and n_H is the Hill coefficient.

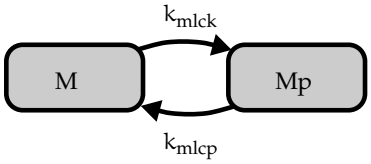

Figure 10: The reduced Hai and Murphy (1988) model (Yang et al., 2005).

Koenigsberger et al. (2004, 2005, 2006) constructed a mathematical model of a population of SMCs and ECs homo- and heterocellularly coupled through GJs on the basis of Parthimos et al. (1999). The focus of their research is the formation of intracellular SMC Ca^{2+} oscillations leading to arterial contraction and vasomotion when synchronising. Cell stimulation is obtained by

receptor-ligand agonists which, *via* the G protein, activate phospholipase C (PLC) and induce the release of the second messenger IP_3 (Clapham, 1995). The Koenigsberger et al. model extends that of Parthimos et al. (1999), in which the equations for Ca^{2+} concentrations are based on the two-compartment lumped parameter model of Goldbeter et al. (1990).

The Koenigsberger et al. (2006) model comprises nine differential equations describing the rate of change of intracellular Ca^{2+} concentration, IP_3 concentration and membrane potential of EC and SMC, the ER and sarcoplasmic reticulum (SR) Ca^{2+} concentration, respectively, and the open probability of the big potassium (BK) channel in the SMC.

Koenigsberger et al. (2006) include stretch-activated channels (SACs) in their model, which react to circumferential stress created by blood pressure. The channels are permeable to Ca^{2+} and other ions. However, they were not considered in the model. Data for the SACs are obtained from *in vitro* experiments conducted on isolated rat kidneys by Takenaka et al. (1998).

A graphical representation of the Koenigsberger et al. model is given in Figure 11.

The Koenigsberger et al. (2006) model can be used to form an important basis of an NVU model because it comprises the two cell types that make up the arteriolar wall. This model includes the most important ion channels and pumps, and incorporates conservation equations for voltage, Ca^{2+} and IP_3, but not for K^+. However, there are a number of simplifying assumptions made in the model. The authors omit the introduction of volume ratios for the cytosol and the intracellular Ca^{2+} stores. These "effective volumes" are introduced by Parthimos et al. (1999) and take into account that the ratio of 'free' (unbuffered) Ca^{2+} ions in the cytosol to the ones in the intracellular stores is similar to the physiological volume ratio of the two compartments.

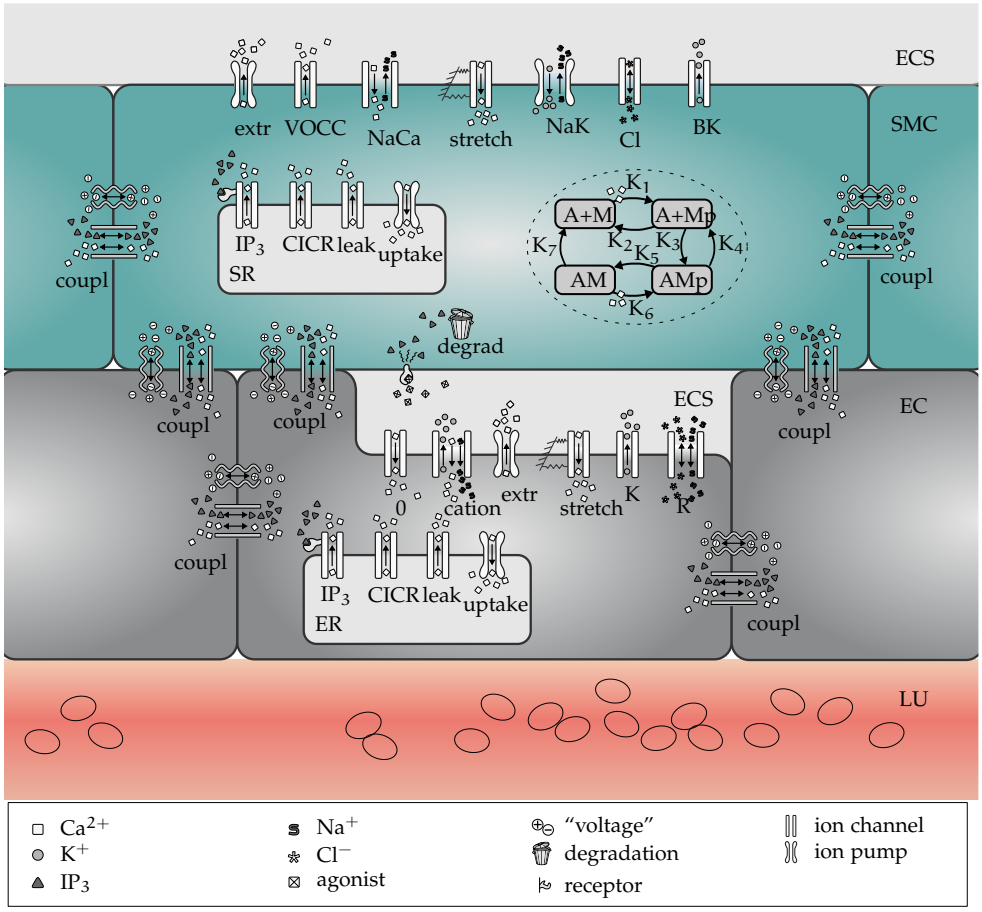

Figure 11: Representation of the Koenigsberger et al. (2006) model

Furthermore, the IP_3-induced Ca^{2+} release from the ER and SR is not accounted for in the conservation equation of the Ca^{2+} concentration in the stores.

3.2 MODELS OF NEUROVASCULAR COUPLING

NVC has been studied for over 100 years (Roy and Sherrington, 1890). However, few mathematical models can be found in the literature.

The presented work is based on the work of Farr and David (2011), who were the first to publish a mathematical model that describes complete com-

munication pathways between NEs and the vasculature. Their model includes the base principles of K^+ and EET signalling in the NVU. This model simulates neuronal activity by a K^+ efflux. It also includes astrocytic Ca^{2+} variations induced by Glu release into the SC and the subsequent efflux of K^+ into the PVS from the Ca^{2+}-mediated BK channel. Although the model provides a qualitative description of NVC the rate of change of perivascular K^+ is slow and the dilation of the associated arteriole takes too long to reach even small dilations. In addition, the perivascular K^+ concentration, at which the SMC membrane potential is maximally hyperpolarised, is too high. However, it does predict constriction for large K^+ concentrations qualitatively similar to the experimental work of Edwards et al. (1988).

The extension of the Farr and David (2011) model by Witthoft and Karniadakis (2012) and Witthoft et al. (2013) introduces bi-directional NVC (also called "inversion of NVC"). This is due to the feedback of the vascular radius *via* the stretch-activated TRPV4 channels to the NEs. In addition to this, it has not yet been studied how many of the signalling pathways include backward feeding segments. One unquestionable fact is that all cells in an NVU are closely linked with their adjacent cells and complex mechanisms like NVC would not be possible without this.

Chang et al. (2013) present a phenomenological model of NVC. The arterial radius, R, is given as a function of only the extracellular K^+ concentration, including terms for constriction and dilation:

$$R = R_0 \overbrace{\exp\left(-\left(\frac{[K^+]_{ecs} - 3.5}{a}\right)^2\right)}^{\text{constriction}} \times \overbrace{\frac{1 + b\exp\left(-(([K^+]_{ecs} - 10)/c)^2\right)}{1 + b\exp\left(-(6.5/c)^2\right)}}^{\text{dilation}}, \tag{3.4}$$

where R_0 is the equilibrium radius and the parameters a, b, and c are fit to the radius versus extracellular K^+ plot of the Farr and David model.

The arterial radius determines the CBF, well-modelled by Poiseuille flow, and therefore the O_2 delivery to the tissue, S. The following reaction-diffusion equation describes the time- and space-dependent tissue O_2 concentration:

$$\frac{\partial [O_2]}{\partial t} = D_{O_2} \frac{\partial^2 [O_2]}{\partial x^2} + S \,, \tag{3.5}$$

where D_{O_2} is the O_2 diffusion coefficient. The ATPase pump behaviour, in turn, is dependent on the availability of O_2.

Chander and Chakravarthy (2012) present a biophysical NVU model that comprises NEs, ACs and SMCs focussing on neuro-glial-vascular loop interactions. Their NE model is based on the Hodgkin and Huxley model and modified to generate firing rates below 100 Hz. The AC compartment follows the formulation of EET dynamics of Bennett et al. (2008). Interestingly, they include a metabolic feedback mechanism, including glucose release from the blood vessel, an astrocyte-neuron lactate shuttle and a simplified tricarboxylic acid (TCA) cycle that produces ATP for the Na^+/K^+ ATPase pump in the neuron.

The Chander and Chakravarthy (2012) model, however, omits the inclusion of ECs, which are known to play an important role in the dynamics of the NVU, including modulatory effects (Lok et al., 2007). Furthermore, ECs express transporters that facilitate the BBB transport of nutrients, ions and peptides (Zlokovic, 2011).

3.3 MODELS OF CEREBRAL VASCULATURE

There are numerous models for cerebral hæmodynamics of different levels of detail. These models describe either parts of or the whole cerebro-vascular tree, reaching from the carotid and vertebral arteries down to the capillary

plexuses. An excellent review of existing models of perfusion in the cerebral vasculature is presented by David et al. (2008).

Most relevant for the present work are models that focus on the space-filling geometry of the cerebral arterial sub-tree comprising the arteriolar and capillary bed level, which is needed to perfuse tissue evenly.

3.3.1 *Spatial Tree Layout*

The vascular network exhibits a tree-like structure with large vessels branching into successively shorter and narrower vessels. Due to the high surface-to-volume ratio most of the blood-tissue exchange of O_2 and CO_2 occurs in the terminating arterioles and capillaries. Arterial trees have been optimised for their task of transporting blood to the respective perfusion sites. To imitate this space-filling geometry Schreiner and Buxbaum (1993) have developed a method to adaptively 'grow' vascular trees *in silico* following optimisation principles for branching angles, pressure profiles, segment radii, and perfusion homogeneity. For a given cerebral tissue volume considered to be perfused this method is called constrained constructive optimisation (CCO) and an example of a three-dimensional vascular tree by Karch et al. (1999) is given in Figure 12.

CCO generated arterial trees very closely resemble the even distribution of terminal segments over the perfusion area imitating a homogeneous supply of blood (Schreiner et al., 2000). However, the fact that they are not symmetric and have adaptive vessel lengths and radii makes it difficult to simulate blood flow through these models and implement them in tissue-like structures, especially in parallel, which is one of the objectives of this work (section 1.3).

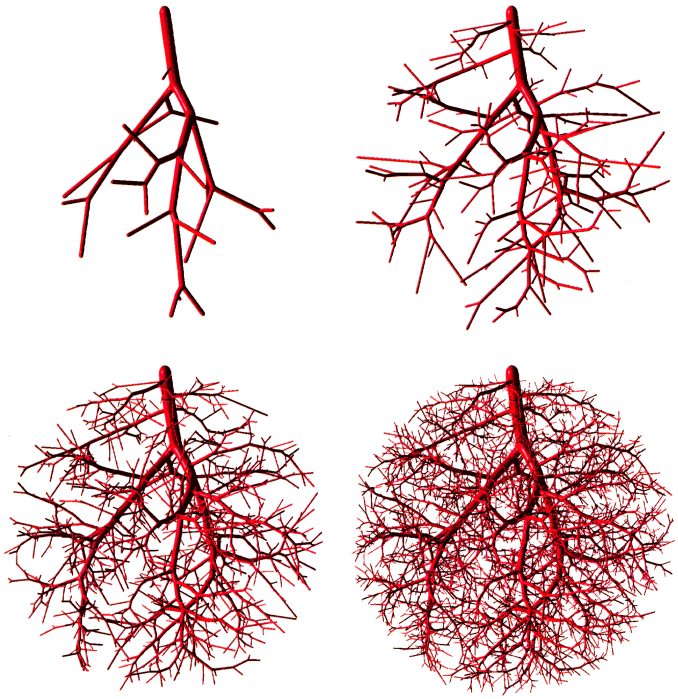

Figure 12: Constrained constructive optimisation technique for adaptive arterial tree growth. (Reproduced with friendly permission from Karch et al. (1999)).

3.3.2 *Blood Flow in the Vascular Tree*

Blood is composed of blood cells (erythrocytes, leukocytes and thrombocytes) suspended in plasma. Its colloidal character makes it a complex fluid with non-Newtonian properties. The blood flow in a non-deformable circulatory system can be described by three-dimensional numerical simulation based on the Navier-Stokes equations:

$$\frac{\partial \mathbf{u}}{\partial t} + \mathbf{u} \cdot \nabla \mathbf{u} = -\nabla p + \nu \nabla^2 \mathbf{u} \,, \quad \nabla \cdot \mathbf{u} = 0 \,, \tag{3.6}$$

where $\mathbf{u}$ is a velocity vector, $\mathbf{p}$ the pressure, and ν is the kinematic viscosity, (e.g. Grinberg et al., 2011).

Patient-specific models and models for local phenomena, like carotid bifurcation or stented artery, are better described by three-dimensional simulations (Gabrys et al., 2006). For example, Cebral et al. (2001) simulate variations of the cerebral arterial circle (CAC) using an unsteady pulsatile flow in a three-dimensional rigid walled model.

From a computational point of view, however, three-dimensional models of a complete arterial tree are hardly affordable, because they require complicated methods of model and mesh generation, which makes them very computationally expensive.

Many authors have described simplified zero-, one- or two-dimensional models of blood flow through vessels. The simplest form of the governing equations arises when blood flow is described by Hagen-Poiseuille flow. This assumes Newtonian, fully developed, steady, axisymmetric flow in a straight rigid pipe. For a vessel of length l and radius r:

$$u(t) = \frac{\pi r^4}{8\mu l} \Delta p f(t) \, , \tag{3.7}$$

where μ is the blood viscosity and Δp is the pressure difference over l, and where $\Delta p / l$ is a constant. The time-dependent function $f(t)$ describes changes in blood flow, e.g. due to the heart beat.

The Womersley number, N_w, is a dimensionless measurement for biofluids and describes the ratio between the transient internal and the viscous force (Fung, 1993):

$$N_w = \frac{\text{transient internal force}}{\text{viscous force}} = \frac{\rho \omega U}{\mu U d^{-2}} = \frac{\rho \omega d^2}{\mu} \, , \tag{3.8}$$

where ρ is the fluid density, ω the angular frequency of oscillations, U the characteristic velocity, d the diameter of the pipe (characteristic length) and μ the dynamic viscosity.

When N_w is smaller than 1, the frequency of pulsations is sufficiently low that a parabolic velocity profile has time to develop and the flow can be given to a good approximation by Poiseuille's law (Nichols et al., 1992). For blood flow in arterioles we have a typical diameter of 10 µm to 20 µm (Bell and Zlokovic, 2009), $\rho = 1060\,\mathrm{kg\,m^{-3}}$ and $\mu = 3\times10^{-3}\,\mathrm{Pa\,s}$ to $4\times10^{-3}\,\mathrm{Pa\,s}$. ω is equal to 2π times the heart rate frequency (60 to 100 beats per minute), therefore $\omega = 1\,\mathrm{s^{-}}1$ to $1.7\,\mathrm{s^{-}}1$. With these values we obtain a N_w of the order of magnitude of 0.01, which is small enough to assume Hagen-Poiseuille flow (Equation 3.7).

Moore et al. (2005) and Grinberg et al. (2011) compare one- and three-dimensional models of the CAC. Results show good correlation between the two models for the transient efferent flux profile (Moore et al., 2005) and also for pressure drop along the arteries (Grinberg et al., 2011). One-dimensional models have a much faster solution time, however, predicting less resistance in geometrically complex arteries than three-dimensional models (Moore et al., 2005).

4

SINGLE NEUROVASCULAR UNIT FOUNDATION MODEL

4.1 INTRODUCTION

The brain consumes high amounts of energy for neuronal firing and cycling of neurotransmitters. It relies on continuous supply of blood providing nutrients and O_2 and clear metabolic products such as CO_2, lactate, and heat. It is essential that the blood flow is well-regulated, because cerebral tissue is extremely sensitive to decreased perfusion and the brain does not comprise a local energy reserve (Lok et al., 2007).

NVC is a complex cerebrovascular control mechanism that ensures adequate perfusion distribution and increased blood flow in active brain regions. The NVU is an assembly of brain cells dynamically performing together and functioning as a major contributor to NVC. These cells, namely NEs, ACs and the vascular cells ECs and SMCs, generate, coordinate and transduce molecular signals underlying the changes in blood flow (Iadecola, 2004).

There are a number of primary and secondary signalling pathways that couple neuronal activity to vascular response, many of which are still not fully understood. During activation NEs release vasoactive substances, such as the neurotransmitters acetylcholine, GABA, catecholamines, and neuropeptides, into the SC. Other released substances are not vasoactive themselves, but act indirectly on the vessel by stimulating the production of vasodilators and

-constrictors. Such mediators include Glu, hydron (H^+) ions, K^+, Ca^{2+}, adenosine, and prostaglandins (Lok et al., 2007).

For NVC signalling, glial cells are of particular importance, specifically ACs. These are known to have an important role in maintaining the neuronal environment and in the control of the vessel diameter. ACs surround SCs with their peripheral ends and take up extracellular K^+ released from NEs. K^+ ions are then transported to the end-feet of the ACs, released into the PVS through BK channels and subsequently taken up by the SMCs.

The SMCs form the centre of the NVU since they receive input from both neuronal activity *via* the ACs and indications of the state of blood flow from the endothelium. These inputs are in the form of voltage coupling via ionic transport, release of SMC cytosolic Ca^{2+} from the SR due to IP_3 transported from the EC, and finally Ca^{2+} from the EC itself. The SMCs and ECs exhibit intracellular communication via hetero-cellular connexin gap-junctions (Haddock et al., 2006). Cells can change their dynamical state by transporting messenger molecules, such as IP_3 and Ca^{2+}, through these gap-junctions.

The primary pathways in NVC all seem to be regulated to a large extent by the K^+ concentration in the PVS (Filosa et al., 2006). K^+ elevations during neuronal activation set into motion a series of events which changes intracellular Ca^{2+} in the SMC. Here, the response of arterioles under normal physiological conditions depends on the amount of K^+ released from the ACs. Higher concentrations lead to vasoconstriction, while lower concentrations lead to vasodilation (Lok et al., 2007).

Nevertheless, many of the underlying mechanisms that govern NVC have not been fully elucidated (Iadecola, 2004). Investigating the relationship between neuronal activity and the resulting variation in the radius of the perfusing arteriole in addition to the role of EC/SMC connectivity and the resulting effects of flowing blood is crucial to further understanding of NVC.

To gain more insight into these complex pathways computational models based on physical, hæmodynamical and electrical laws have been helpful in elucidating the role of certain cells and pathways in components of NVC. Over the past two decades, several mathematical models have been developed to mimic components of certain chemical pathways within the NVC (see chapter 3).

The present model extends the Farr and David (2011) model to include a more sophisticated neuronal activity simulation using the work of Østby et al. (2009), which includes the time-dependent efflux and influx of K^+ and Na^+ ions, respectively, during neuronal activity. Furthermore, an additional BK channel at the end-foot of the AC is included, which allows K^+ to move out of the AC and into the PVS inducing vessel response (Filosa et al., 2006).

The present model does not include a Ca^{2+} mediated BK channel since the Ca^{2+} concentration reaches only about 180 nM and data from Cox et al. (1997) shows that the activation and deactivation times vary very little at such low concentrations, similarly for tail currents at physiological membrane potentials. Additionally, as noted in the model development, work by Gonzalez-Fernandez and Ermentrout (1994) has indicated that the dynamics of the BK channel are essentially unchanged if an average astrocytic Ca^{2+} is assumed. BK channels are also mediated by membrane potential (Chung et al., 2007; Gonzalez-Fernandez and Ermentrout, 1994). However, this is not to mean that astrocytic Ca^{2+} is not an important pathway for BK channel activation, just that it may not be the only one.

The model is based on experimentally validated ion channel parameters providing it with the ability to describe the full NVC phenomenon. The model contains that which we believe to be the fundamental ingredients of NVC, but it also has the ability to include other pathways.

4.2 METHODS

The NVU, as defined in this model, includes the following compartments: NE, AC, SMC coupled to an EC. These cell types along with the SC and the PVS are represented in the model by separate subdomains. These subdomains are assembled together using a lumped parameter approach, where spatial variations in the compartments are considered negligible, thus allowing intercellular interactions.

It should be noted that although each compartment is assumed to contain a number of homotypic cells and to have differing volumes, they are considered to be an aggregate of cells and therefore act as a single entity. A graphical overview of these lumped domains is shown in Figure 13.

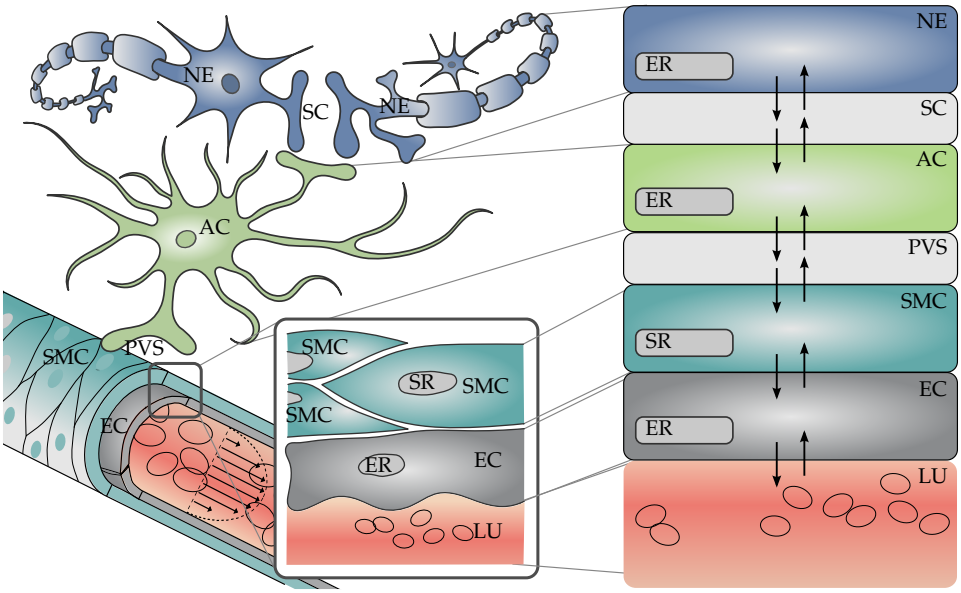

Figure 13: Compartment model of an NVU using a lumped parameter approach. Aggregates of homotypic cells are assumed to act as single entities with uniform concentrations throughout. NE - neuron, SC - synaptic cleft, AC - astrocyte, PVS - perivascular space, SMC - smooth muscle cell, EC - endothelial cell, ER - endoplasmic reticulum, SR - sarcoplasmic reticulum, LU - lumen. Intercellular communication is indicated by arrows.

To understand the connectivity of the full system we consider four "subsystems", the NE/AC subsystem including the PVS and SC, the SMC/EC subsystem, which couples the SMC and EC together, the Arteriolar Contraction subsystem and the Arteriolar Wall Mechanical subsystem. We treat each subsystem as having a "triggering" input and subsequent output that provides connectivity and a further "triggering" input to the other linked subsystems, essentially a coupling influence across all subsystems providing a holistic model.

A full list of equations and parameters used for this model can be found in the Appendix (section A.1).

4.2.1 *Neuron/Astrocyte Subsystem*

The model for this subsystem describes the crucial biochemical processes within the NE, the SC, the AC and the PVS. It extends the model of Østby et al. (2009) by adding a large conductance K^+ channel in the astrocytic wall and directing K^+ into the PVS with flux J_{BK}. The Østby et al. (2009) model was chosen since it provides a basic model for K^+ efflux. We use this on the basis of the work of Filosa et al. (2006), which showed that K^+ efflux into the SC is one of the dominant effects of neuronal activity.

An illustration of the NE/AC subsystem is shown in Figure 14. All of the ion channels and pumps that are implemented in this model are listed in Table 1.

The mathematical formulations for the BK channel are based on those presented by Gonzalez-Fernandez and Ermentrout (1994). We model the open probability of the BK channel, w_k, as a membrane-voltage-mediated process given by

$$\frac{dw_k}{dt} = \phi_w \left(w_\infty - w_k \right) \ , \tag{4.1}$$

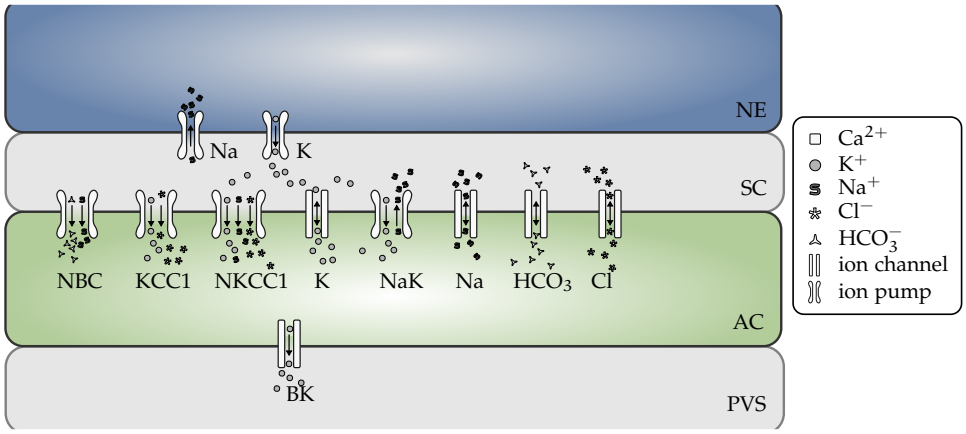

Figure 14: Detail of the NE/AC subsystem.

Table 1: Table of ion pumps and channels used in the Neuron/Astrocyte subsystem.

Flux	name	permeable to	mediated by
$J_{K,s}$	Potassium pump	K^+	K^+
$J_{Na,s}$	Sodium pump	Na^+	Na^+
$J_{NBC,k}$	Sodium bicarbonate pump	Na^+, HCO_3^-	v_k, Na^+, HCO_3^-
$J_{KCC,k}$	Potassium chloride co-transporter	K^+, Cl^-	K^+, Cl^-
$J_{NKCC,k}$	Sodium Potassium chloride co-transporter	Na^+, K^+, Cl^-	Na^+, K^+, Cl^-
$J_{K,k}$	Potassium channel	K^+	v_k, K^+
$J_{NaK,k}$	Sodium potassium pump	Na^+, K^+	v_k, Na^+, K^+
$J_{Na,k}$	Sodium channel	Na^+	v_k, Na^+
$J_{HCO_3,k}$	Bicarbonate channel	HCO_3^-	v_k, HCO_3^-
$J_{Cl,k}$	Chloride channel	Cl^-	v_k, Na^+, HCO_3^-
$J_{BK,k}$	Large conductance K^+ channel	K^+	v_k, K^+

where the equilibrium state BK-channel open probability, w_∞, is a function of the membrane potential, v_k:

$$w_\infty = 0.5\left(1 + \tanh\left(\frac{v_K + v_6}{v_4}\right)\right) \tag{4.2}$$

and the time constant ϕ_w associated with the opening of BK channels as

$$\phi_w = \psi_w \cosh\left(\frac{v_k + v_6}{2v_4}\right) . \tag{4.3}$$

In the normal manner we write the K^+ flux through the BK channel

$$J_{BK,k} = \frac{g_{BK,k}}{F} w_k \left(v_k - E_{BK,k}\right) , \tag{4.4}$$

here $E_{BK,k}$ is the Nernst potential for the BK channel given by

$$E_{BK,k} = \frac{R_{gas} T}{z_K F} \ln\left(\frac{K_p}{K_k}\right) \tag{4.5}$$

with K_p and K_k designated as the K^+ concentrations in the PVS and AC compartments, respectively. z_K is the ionic valence for K^+, and F is the Faraday's constant. In contrast to both Filosa et al. (2004) and Farr and David (2011) the characteristic time scale for the BK channel is independent of Ca^{2+}. Unpublished results from our own group and the analysis of Gonzalez-Fernandez and Ermentrout (1994) show that the dynamics of the BK channel are essentially unchanged when an average value of the astrocytic Ca^{2+} is assumed. This allows investigations into the sensitivity of the model to membrane potential and other pathways.

The NE model of Østby et al. (2009) is used to provide a time-dependent input for the NE/AC subsystem simulating neuronal activity. It is a simplified model, however it is sufficient in providing the essential qualities and quantities; that is the production of K^+ into the SC and its re-distribution back to the NE *via* the Na/K ATPase pump. Other more detailed NE models could be used, such as that given by Chang et al. (2013), but essentially synaptic K^+ dominates the system input for this NVC foundation model.

Østby et al. (2009) model neuronal activity as a time-dependent input signal, $f_{K/Na}(t)$, describing the release of K^+ into the SC and a simultaneous equal influx of Na^+ into the NE. For the profile of $f_{K/Na}(t)$ Østby et al. (2009) assumed a beta distribution with the governing parameters α_n and β_n fulfilling the following two criteria:

1. The time from the starting input until the attained maximum level of the K^+ concentration in the SC should be 5 s.

2. The level of K^+ concentration in the SC at $t = t_0 + 30$ s should be 70% of the maximum level.

The present model uses the Østby et al. (2009) input with $\alpha_n = 2$ and $\beta_n = 5$.

The amplitude of the input signal is scaled by the value F_{input} to reach the same order of magnitude of K^+ efflux proposed by experiments (Filosa et al., 2006).

Beside this neuronal input signal, the NKCC1 (sodium-K^+-chloride) and KCC1 (K^+-chloride) co-transporters are enabled when the neuronal ion release and spatial buffering are applied. This behaviour is modelled by a simple step function with the value 1 when both are activated and with a default value of 0. The input signal and the co-transporter behaviour is shown in Figure 15.

For the PVS, the volume ratio between the AC and the SMC compartments is (unlike the surface-volume ratio for the SC and the AC in the Østby et al. (2009) model) not a function of time and is kept constant. It is known by Nagelhus et al. (1999) that the length scale of the PVS is in order of several nanometres, while the length scale for cells like ACs and SMCs is in the order of micrometres. For this reason, we have chosen the volume ratio between the cells and PVS to be 0.001.

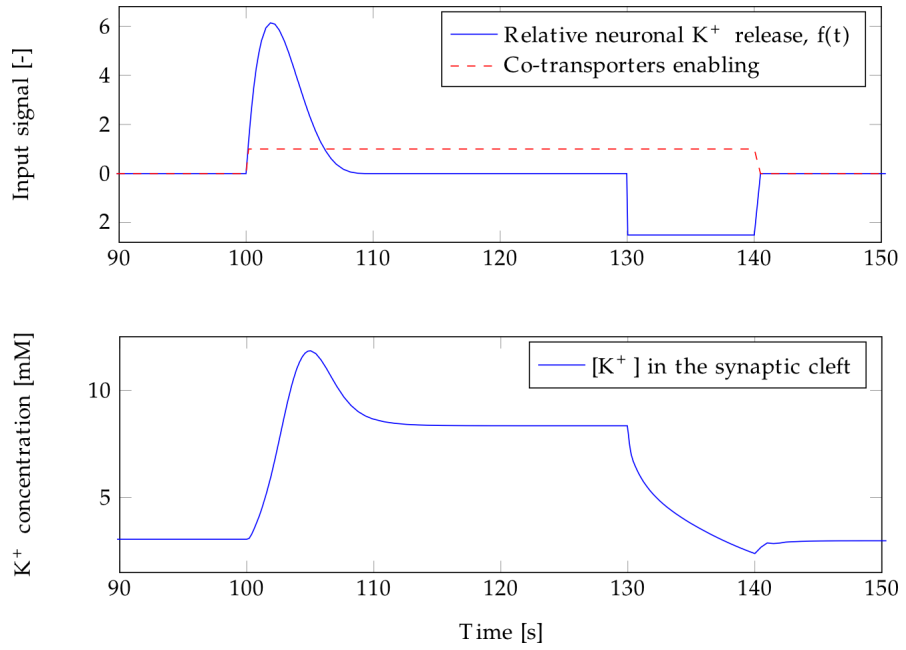

Figure 15: Input signals and the K^+ concentration in the synaptic cleft. Top: Neuronal release function $f_{K/Na}(t)$ of K^+. Blue continuous line - The K^+ efflux is modelled by a beta distribution and buffered back afterwards. Red dashed line - The co-transporters are enabled when the neuronal ion release and spatial buffering is applied, modelled by a block function. Bottom: The K^+ concentration in the synaptic cleft.

The increase of K^+ in the SC during neuronal activity results in an increased K^+ uptake by the AC, which consequently undergoes depolarisation. This results in a K^+ efflux in order to repolarise the compartment ("cell") membrane back to its steady state potential. Since physiologically most of the astrocytic K^+ conductance channels are located at the end-feet, the outward current-carrying K^+ would flow out largely through these processes. These end-feet K^+ conductance channels are modelled by the BK channel flux $J_{BK,k}$ and are given by Equation 4.1 to Equation 4.5.

Consequently, the K^+ is 'siphoned' from the SC to the end-feet of the AC and released into the PVS by the BK channel. This efflux increases the PVS K^+ concentration, which is an input variable for the SMC/EC subsystem, therefore giving the addition of the BK channel particular importance.

4.2.2 *Smooth Muscle/Endothelial Cell Subsystem*

The SMC/EC subsystem model extends the work of Koenigsberger et al. (2006) by adding an inward-rectifying potassium (KIR) channel (with flux J_{KIR}) at the interface between the SMC and the PVS. It allows a K^+ flux in and out of the cell, but is named "inwardly-rectifying", because it passes K^+ ions more easily in the inward direction than in the outward direction at membrane potentials negative to K^+ reversal potential. The KIR channel models the connection between the NE/AC and SMC/EC subsystems via the PVS. The biochemical behaviour of the KIR channel is modelled and implemented according to experimental data by Filosa et al. (2006).

A graphical overview of the SMC/EC subsystem is shown in Figure 16. All of the ion channels and pumps that are implemented in this model are listed in Table 2.

The KIR channel is mediated by K^+ concentration in the PVS, $[K^+]_p$, which varies with neuronal activity. The rise in K^+ activates the KIR channel on the SMC causing release of more K^+ into the PVS. The efflux of cytosolic K^+ *via* the KIR channel hyperpolarises the SMC, causing the voltage-operated Ca^{2+} channel to close and preventing any further influx of Ca^{2+} into the SMC cytosol. The formulation of the KIR channel uses the data of Filosa et al. (2006).

The flux $J_{KIR,i}$ through the KIR channel in the SMC compartment (in $\mu M\,s^{-1}$) is written as

$$J_{KIR,i} = \frac{F_{KIR,i}\, g_{KIR,i}}{\gamma_{conv}} \left(v_i - v_{KIR,i}\right) , \tag{4.6}$$

where γ_{conv} is a conversion parameter relating the net movement of ions to the membrane potential, providing $J_{KIR,i}$ in the correct units of $\mu M\,s^{-1}$ (Koenigsberger et al., 2006).

Table 2: Table of ion pumps and channels used in the SMC/ EC subsystem.

Flux	name	permeable to	mediated by
$J_{KIR,i}$	Inward-rectifier potassium channel	K^+	v_i, K_p^+
$J_{CICR,i}$	Calcium induced calcium release channel	Ca^{2+}	Ca_i^{2+}, $\widehat{Ca}_i^{2+}$
$J_{IP_{3,i}}$	IP_3 sensitive calcium channel	Ca^{2+}	IP_{3_i}
$J_{SR_{leak,i}}$	Sarcoplasmic leak channel	Ca^{2+}	$\widehat{Ca}_i^{2+}$
$J_{SR_{upt,i}}$	Sarcoplasmic uptake channel	Ca^{2+}	Ca_i^{2+}
$J_{NaK,i}$	Sodium potassium pump	Na^+, K^+	-
$J_{K,i}$	Potassium channel	K^+	v_i, Ca_i^{2+}
$J_{extr,i}$	Calcium extrusion pump	Ca^{2+}	v_i, Ca_i^{2+}
$J_{VOCC,i}$	Voltage operated calcium channel	Ca^{2+}	v_i
$J_{stretch,i}$	Stretch activated channel	Ca^{2+}	v_i, Δp, R
$J_{NaCa,i}$	Sodium calcium exchange pump	Na^+, Ca^{2+}	v_i, Ca_i^{2+}
$J_{Cl,i}$	Chloride channel	Cl^-	v_i
$J_{degrad,i}$	IP_3 degradation	IP_3	$IP_{3,i}$
$J_{Ca_{cpl}^{2+}}$	Heterocellular calcium coupling channel	Ca^{2+}	Ca_i^{2+}, Ca_j^{2+}
$J_{V_{cpl}}$	Heterocellular voltage coupling channel	v	v_i, v_j
$J_{IP_{3_{cpl}}}$	Heterocellular IP_3 coupling channel	IP_3	IP_{3_i}, IP_{3_j}
$J_{CICR,j}$	Calcium induced calcium release channel	Ca^{2+}	Ca_j^{2+}, $\widehat{Ca}_j^{2+}$
$J_{IP_{3,j}}$	IP_3 sensitive calcium channel	Ca^{2+}	IP_{3_j}
$J_{ER_{leak,j}}$	Endoplasmic leak channel	Ca^{2+}	$\widehat{Ca}_j^{2+}$
$J_{ER_{upt,j}}$	Endoplasmic uptake channel	Ca^{2+}	Ca_j^{2+}
$J_{0,j}$	Calcium channel	Ca^{2+}	-
$J_{cation,j}$	Non selective cation channel	Ca^{2+}	v_j, Ca_j^{2+}
$J_{extr,j}$	Calcium extrusion pump	Ca^{2+}	Ca_j^{2+}
$J_{stretch,j}$	Stretch activated channel	Ca^{2+}	v_j, Δp, R
$J_{K,j}$	Large conductance potassium channel	K^+	v_j, Ca_j^{2+}
$J_{R,j}$	Residual current regrouping channel	Na^+, Cl^-	v_j
$J_{degrad,j}$	IP_3 degradation	IP_3	IP_{3_j}
J_{PLC}	IP_3 production	IP_3	agonist

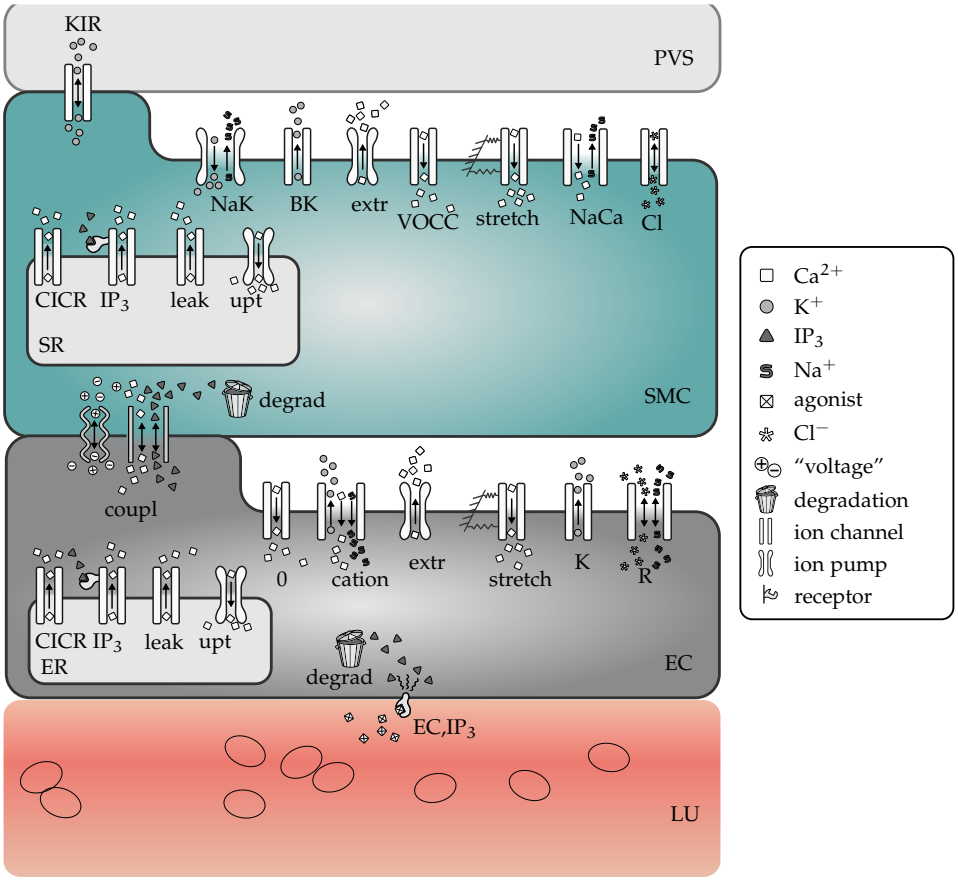

Figure 16: Detail of the SMC/EC subsystem.

Here the Nernst potential (in mV) is a function of $[K^+]_p$ and given as

$$v_{KIR,i} = z_1[K^+]_p - z_2 \ , \tag{4.7}$$

where z_1 and z_2 are derived by fitting a linear function to the data of Filosa et al. (2006). The conductance of the KIR channel is a function of both membrane potential, v_i, and $[K^+]_p$. It is formulated as

$$g_{KIR,i} = \exp\left(z_5 v_i + z_3[K^+]_p - z_4\right) \ , \tag{4.8}$$

again with fitting parameters to the data of Filosa et al. (2006). Figure 17 shows the experimental data of Filosa et al. (2006) and $g_{KIR,i}(v_i, [K^+]_p)$ for $[K^+]_p \in [3, 6, 10]$ mM. The parameter values and units can be found in Table 3.

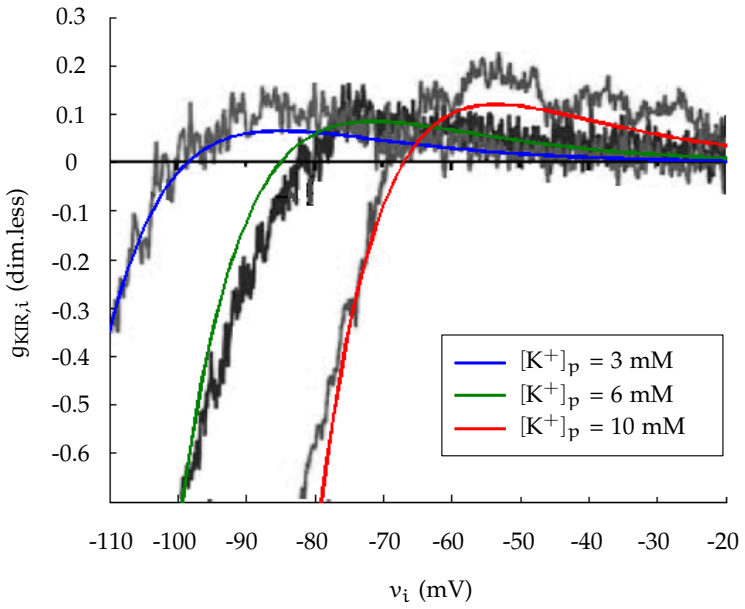

Figure 17: Experimental data of Filosa et al. (2006) and $g_{KIR,i}(v_i, [K^+]_p)$ for $[K^+]_p \in [3, 6, 10]$ mM.

A second important input signal to the SMC/EC subsystem is that of IP_3 generation in the EC. IP_3 is an important messenger molecule and its production in the endothelium is triggered by luminal agonists such as ATP, which bind onto P2Y membrane receptors on the luminal side of the endothelium. For the present foundation model the production of IP_3 is treated as a constant. However, more attention will be paid to variations of it in the following model extensions (see chapter 5).

Physiologically, ECs and SMCs are connected by hetero- and homocellular gap junctions that allow an intercellular exchange of molecules and voltage. Since in the present NVCs model only one compartment of aggregated cells

is modelled, the homocellular exchange between cells is neglected. The heterocellular exchange, however, is implemented by the following linearised coupling fluxes: $J_{Ca^{2+}_{cpl}}$, $J_{V_{cpl}}$ and $J_{IP_{3_{cpl}}}$ for Ca^{2+}, voltage and IP_3 coupling, respectively. These coupling functions are given by

$$\begin{aligned} J_{Ca^{2+}_{cpl}} &= -P_{Ca^{2+}}([Ca^{2+}]_i - [Ca^{2+}]_j) \\ J_{V_{cpl}} &= -G_v(V_i - V_j) \\ J_{IP_{3_{cpl}}} &= -P_{IP_3}([IP_3]_i - [IP_3]_j)\,, \end{aligned} \tag{4.9}$$

where the subscripts i, j correspond to EC and SMC, respectively.

Barrio et al. (1997) investigated the voltage-gating properties of connexin-43 junctions and indicated that the conductance of the hemi-channel was voltage mediated. However for this particular model, we treat $P_{Ca^{2+}}$, G_v and P_{IP_3} as constants. This can be seen as modelling the simple diffusional flux rather than the more complete electro-diffusional flux which allows for ion drift.

In the SMC/EC subsystem, Ca^{2+} buffering is implemented, and corrects for the fact that approximately 1 % of the intracellular Ca^{2+} is "free" (Parthimos et al., 1999).

4.2.3 *The Arteriolar Contraction Subsystem*

The formation of cross bridges between the actin and myosin filaments in the SMC provides the contraction force and is mediated by cytosolic Ca^{2+}. The arteriolar contraction subsystem model is based on the work of Hai and Murphy (1989), and uses the SMC compartmental cytosolic Ca^{2+} concentration as an input signal.

There are four possible states for the formation of myosin: free nonphosphorylated cross bridges (M), free phosphorylated cross bridges (Mp), attached phosphorylated cross bridges (AMp) and attached dephosphorylated latch bridges (AM; see Figure 18).

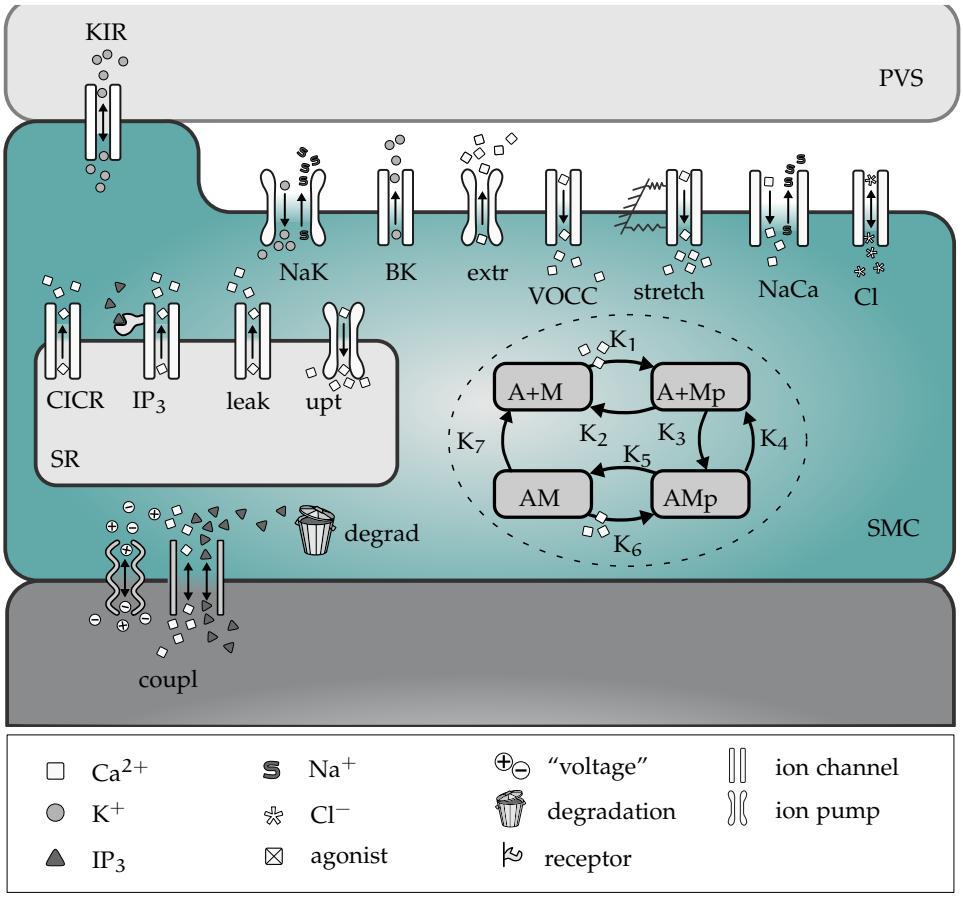

Figure 18: SMC detail with actin and myosin filament contraction system.

The dynamics of the fraction of myosin in a particular state is given by four differential equations:

$$\begin{aligned}
\frac{d[M]}{dt} &= -K_1[M] + K_2[Mp] + K_7[AM] \\
\frac{d[Mp]}{dt} &= K_4[AMp] + K_1[M] - (K_2 + K_3)[Mp] \\
\frac{d[AMp]}{dt} &= K_3[Mp] + K_6[AM] - (K_4 + K_5)[AMp] \\
\frac{d[AM]}{dt} &= K_5[AMp] - (K_7 + K_6)[AM]
\end{aligned} \tag{4.10}$$

with

$$[AM] + [AMp] + [Mp] + [M] = 1 \tag{4.11}$$

where the rate constants, K_n $(n = 1, ..., 7)$, regulate the phosphorylation and bridge formation. Using Equation 4.11 we need only to solve for $[AM]$, $[AMp]$ and $[Mp]$.

The Ca^{2+}-dependence of the cross bridge model is modelled by rate constants K_1 and K_6. The total phosphorylation of myosin is a function of the SMC compartmental Ca^{2+} (Koenigsberger et al., 2006) so that K_1 and K_6 are given by:

$$K_1 = K_6 = \gamma_{cross}[Ca^{2+}]_i^3 \,, \tag{4.12}$$

in which γ_{cross} is a constant characterising the Ca^{2+} sensitivity of calcium-activated phosphorylation of myosin.

The active stress of a smooth muscle cell is directly proportional to F_r, the fraction of attached cross bridges, and is given by Equation (4.13). This is used as an input parameter for the Mechanical subsystem.

$$F_r = \frac{[AMp] + [AM]}{([AMp] + [AM])_{max}} \tag{4.13}$$

4.2.4 *The Arteriolar Wall Mechanical Subsystem*

As an initial and simple representation the basis for the Mechanical subsystem is a Kelvin-Voigt model, which describes the visco-elastic mechanical behaviour of the arterial wall. The model consists of a Newtonian damper and Hookean elastic spring connected in parallel. The fraction of attached myosin cross bridges, F_r, is the input signal for the Mechanical subsystem and corresponds with the active stress state of the smooth muscle cells in the circumferential direction.

This circumferential stress in the arterial wall, $\sigma_{\theta\theta}$, is given by:

$$\sigma_{\theta\theta} = E\epsilon_{\theta\theta} + \eta\frac{d\epsilon_{\theta\theta}}{dt} , \tag{4.14}$$

where E is the Young's modulus, η the viscosity and $\epsilon_{\theta\theta}$ the strain in the arterial wall.

Assuming that the acceleration of the vessel wall due to changes in $\sigma_{\theta\theta}$ is negligible, Laplace's law is used in order to relate the circumferential stress to the change in radius:

$$\sigma_{\theta\theta} = \frac{r\Delta p}{h} , \tag{4.15}$$

where Δp is the transmural pressure, r the vessel radius and h the vessel thickness. For simplicity we treat the wall thickness as a constant fraction of the radius, $h = 0.1r$.

To obtain the Young's modulus, E, and initial radius, r_0, as a function of the attached myosin cross-bridges, experimental data of Gore and Davis (1985) is used. For the Mechanical subsystem a linear function is utilised, mapping the fully activated state to the fully relaxed state. The linear fit is based on the radii between 10 µm and 30 µm, since the full model only models small strains.

The Young's modulus and initial radius is assumed to be a continuous function of F_r and a linear interpolation is used between two known experimental data states (active E_{act} and passive E_{pas}) taken from Gore and Davis (1985) of the smooth muscle cell. We can therefore write

$$E(F_r) = E_{pas} + F_r \left(E_{act} - E_{pas}\right) \tag{4.16}$$

In a similar manner the initial radius is given by

$$r_0(F_r) = r_{0,pas} + F_r \left(r_{0,act} - r_{0,pas}\right) \ , \tag{4.17}$$

where $r_{0,act}$ is the arteriolar radius in the active and $r_{0,pas}$ in the passive state.

From Equation (4.14), using Laplacian's law (Equation 4.15) and Equations (4.16) and (4.17) for the Young's modulus and initial radius, respectively, as a function of the F_r, an expression for the time-dependent vessel radius can be derived:

$$\frac{r\Delta p}{h} = E(F_r)\left(\frac{r - r_0(F_r)}{r_0(F_r)}\right) + \eta \frac{d}{dt}\left(\frac{r - r_0(F_r)}{r_0(F_r)}\right) \tag{4.18}$$

giving

$$\frac{dr}{dt} = \frac{r_{0,pas}}{\eta}\left(\frac{r\Delta p}{h} - E(F_r)\frac{r - r_0(F_r)}{r_0(F_r)}\right) \tag{4.19}$$

4.2.5 *Numerical Solution Method*

The model was implemented in MATLAB R2014b. A total of 36 coupled ordinary differential equations (ODEs) make up the entire system and are solved using the stiff solver "ode15s". The system was solved over a time interval of [0,1000] seconds with default relative and absolute tolerances (1e-

3 and 1e-6, respectively). Initial conditions for all state variables can be found in the Appendix.

The three core classes, the `Astrocyte`, `SMCEC` and `WallMechanics`, correspond to the components of the NVU model, namely the astrocyte model, the SMC and EC model, and the mechanical contraction cell model. For a given model component, all fluxes and ODEs are grouped together in the code of the corresponding class. The `NVU` class uses the three core component classes to collect the state variables and derivatives values and pass them to the `ode15s` solver for stiff problems. All classes in OO-NVU code are subclasses of MATLAB's inbuilt `handle` class which makes them appear as reference object to avoid unnecessary object duplication on assignment.

The following features apply to the `Astrocyte`, `SMCEC` and `WallMechanics` classes:

1. The core classes rely on the class constructors to initialise the parameters with the help of the class-specific function parse_inputs(varangin). The constructors also initialise the variable indices, initial conditions and the output indices.

2. In every core class the `rhs` method contains the algebraic and state variables, as well as the corresponding equations.

3. The `shared(self, ~, u)` method, where present, provides access to the shared algebraic or state variables used as input variables in the other model components where appropriate.

Table 3: Parameters used in this model.

Parameter	value	unit	ref.
v_6	22	mV	(Gonzalez-Fernandez and Ermentrout, 1994)
v_4	14.5	mV	(Gonzalez-Fernandez and Ermentrout, 1994)
ψ_w	2.664	s^{-1}	(Gonzalez-Fernandez and Ermentrout, 1994)
$g_{BK,k}$	1.16×10^3	$\Omega^{-1}m^{-2}$	(Gonzalez-Fernandez and Ermentrout, 1994)
F	9.649×10^4	C mol^{-1}	
R_{gas}	8.315	J $mol^{-1}K^{-1}$	
T	300	K	
z_K	1	dim.less	
$F_{KIR,i}$	750	mV μM^{-1}	(Gonzalez-Fernandez and Ermentrout, 1994)
γ_{conv}	1970	mV μM^{-1}	(Koenigsberger et al., 2006)
z_1	4.5×10^3	mV μM^{-1}	(Filosa et al., 2006)
z_2	112	mV	(Filosa et al., 2006)
z_3	4.2×10^2	$mV^{-1}s^{-1}$	(Filosa et al., 2006)
z_4	12.6	$\mu M\ mV^{-1}s^{-1}$	(Filosa et al., 2006)
z_5	-7.4×10^{-2}	$\mu M\ mV^{-2}s^{-1}$	(Filosa et al., 2006)
K_2	0.5	s^{-1}	(Hai and Murphy, 1989)
K_3	0.4	s^{-1}	(Hai and Murphy, 1989)
K_4	0.1	s^{-1}	(Hai and Murphy, 1989)
K_5	0.5	s^{-1}	(Hai and Murphy, 1989)
K_7	0.1	s^{-1}	(Hai and Murphy, 1989)
γ_{cross}	17	$\mu M^{-3}\ s^{-1}$	(Hai and Murphy, 1989)
F_i	0.23	$\mu M\ s^{-1}$	(Koenigsberger et al., 2006)
K_{ri}	1	μM	(Koenigsberger et al., 2006)
C_i	55	$\mu M\ s^{-1}$	(Koenigsberger et al., 2006)
s_{ci}	2.0	μM	(Koenigsberger et al., 2006)
c_{ci}	0.9	μM	(Koenigsberger et al., 2006)
η	10^4	Pa s	(Koenigsberger et al., 2006)
$r_{0,pas}$	20	μm	model estimation (ME)
$h_{0,pas}$	3	μm	ME
P_T	4×10^3	Pa	ME
E_{pas}	66×10^3	Pa	(Gore and Davis, 1985)
E_{act}	167×10^3	Pa	(Gore and Davis, 1985)

4.3 RESULTS

Results are presented from the full model (all subsystems coupled together) that describe the K^+ and Ca^{2+} NVC pathway, starting from a neuronal input signal to the mechanical vessel response.

4.3.1 *Neurovascular Coupling via Potassium Signalling*

The results of the full NVC model are shown in Figure 19. During neuronal stimulation (t = 100 s to 200 s) K^+ is pumped into the SC (see Figure 19a). This results in an increased K^+ concentration in the SC until the NE starts buffering K^+ out of the SC at the end of the stimulus. The elevated K^+ concentration hyperpolarises the AC cell membrane (Figure 19b) resulting in a K^+ efflux through the BK channel into the PVS, in order to repolarise the cell (see Figures 19c and 19d). The increased K^+ concentration in the PVS causes the KIR channel on the SMC to open, extruding more K^+ into the PVS (Figure 19e). This efflux of K^+ is very small compared to the efflux through the BK channel. However, it is large enough to hyperpolarise the SMC (Figure 19f). SMC hyperpolarisation decreases the influx of Ca^{2+} through the voltage-operated Ca^{2+} channel (Figure 19g). The SMC cytosolic Ca^{2+} concentration decreases (Figure 19h) and the SMC contraction force diminishes (Figure 19i) allowing the artery to dilate (Figure 19j).

4.3.2 *Characteristic Vasoreaction Rate*

The original reaction rate constants for the Arteriolar Contraction subsystem given by Hai and Murphy (1989) were developed using a carotid artery,

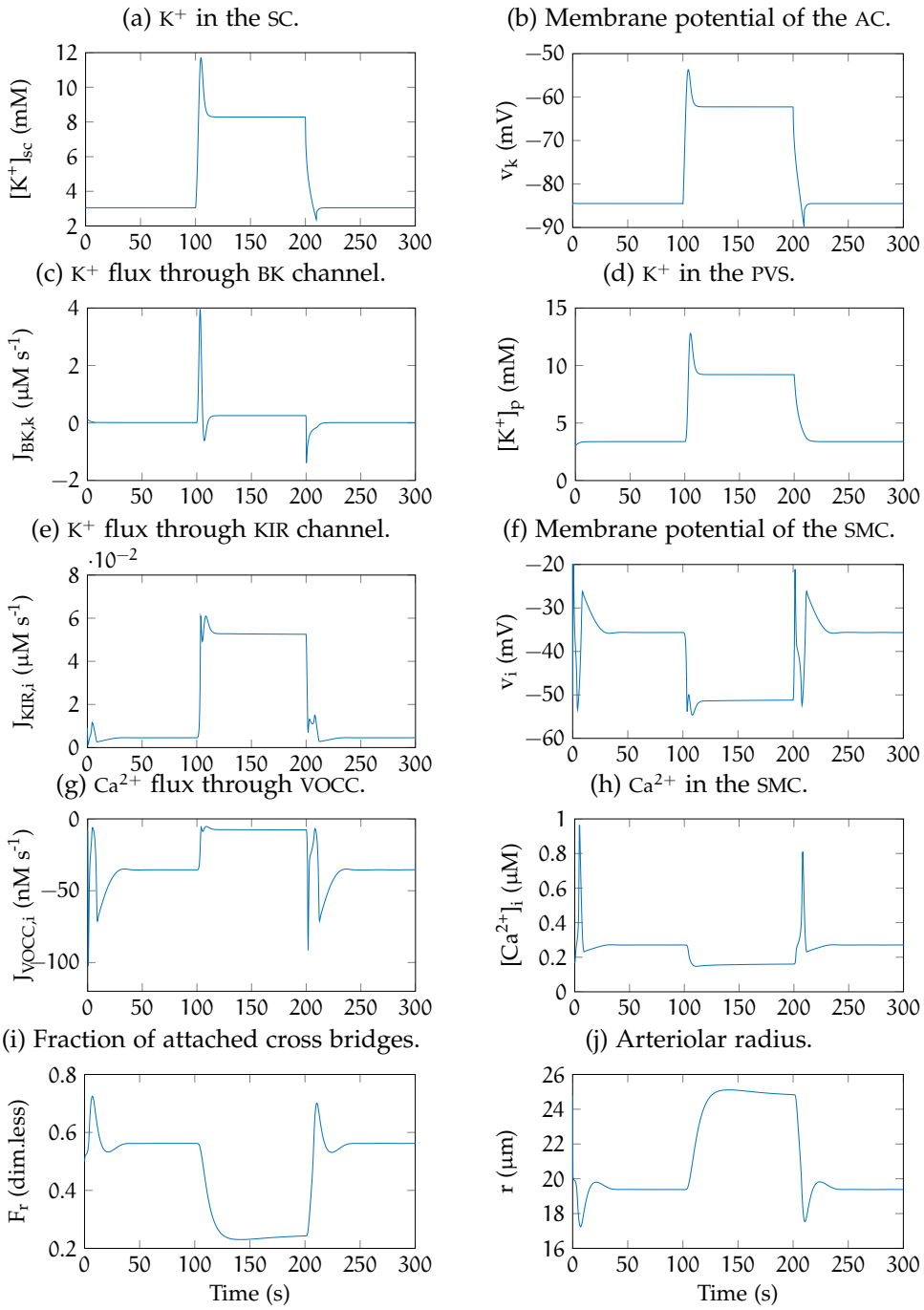

Figure 19: Overview of the NVU dynamics.

which has a larger wall thickness than a cerebro-vascular arteriole. In this case the force exerted by the SMC contained in the carotid wall media is such as to develop a relatively large characteristic time for dilation (or contraction). Experiments with cerebral arterioles have shown the characteristic times to be much shorter. Figure 20 shows the radius as a function of time when the Hai and Murphy (1989) constants have been scaled to allow the rise time of a cerebro-vascular arteriole to be favourably compared with the experiments of Chen et al. (2011). This single scaling factor was found to be 6 to obtain a rise time of approximately 12 seconds, such as found experimentally by forepaw or hindlimb stimulation in the cortex of a rat (Chen et al., 2011).

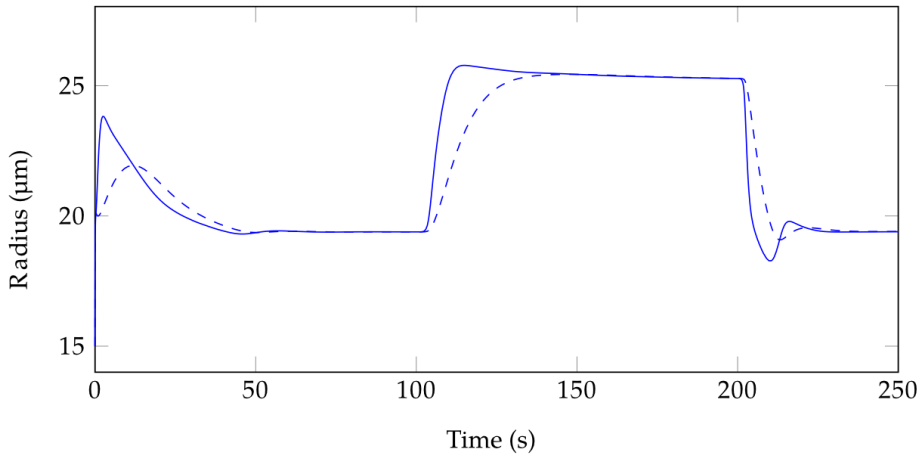

Figure 20: Scaling of the Hai and Murphy (1989) reaction rate constants; dashed line - no scaling factor, solid line - scaling factor of 6.

4.3.3 *Extracellular Potassium*

The neuronal input function $f_{Na/K}(t)$ was scaled and a series of simulations run to produce an increasing concentration of K^+ in the PVS and the associated SMC membrane voltage, v_i, as shown in Figure 21. This indicates the membrane potential change as a function of potassium concentration in the

PVS for the model compared with the experimental data of Edwards et al. (1988).

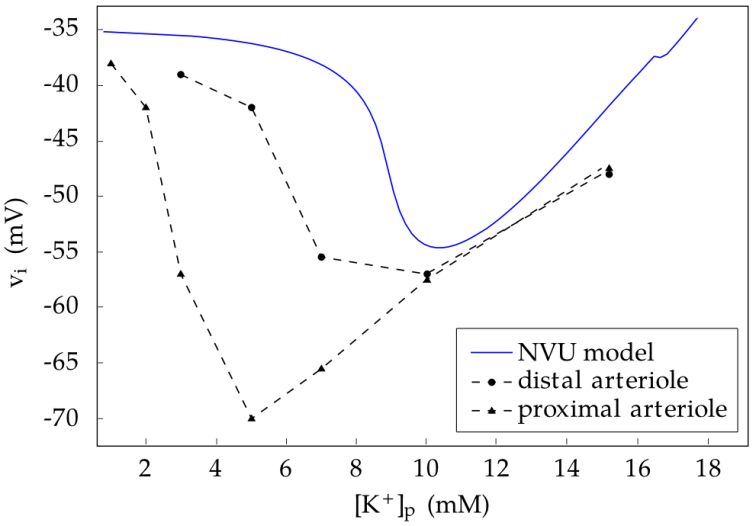

Figure 21: SMC membrane potential dependence on perivascular potassium concentration. Experimental data from Edwards et al. (1988) in comparison with the simulation results of the present model (at a J_{EC,IP_3} production rate of 0.18 µM s^{-1}).

Figure 22 shows the relationship between the K^+ concentration in the synaptic cleft and the induced radial change in the perfusing arteriole. This compares well with the results of Farr and David (2011) varying between 19 and 25 microns over the range of 0.3 µM.

4.3.4 *Calcium in the Smooth Muscle Cell*

The contractile force of SMCs is directly dependent on the intracellular Ca^{2+} concentration (Hai and Murphy, 1988). The resting steady state Ca^{2+} concentration in the SMC cytosol of 0.27 µM is mostly determined by the balance between the calcium-induced calcium release (CICR) influx from the SR and the effluxes $J_{extrusion}$ and J_{uptake} (results not shown). Neuronal activation induces hyperpolarisation of the SMC and a decrease in cytosolic Ca^{2+} (see

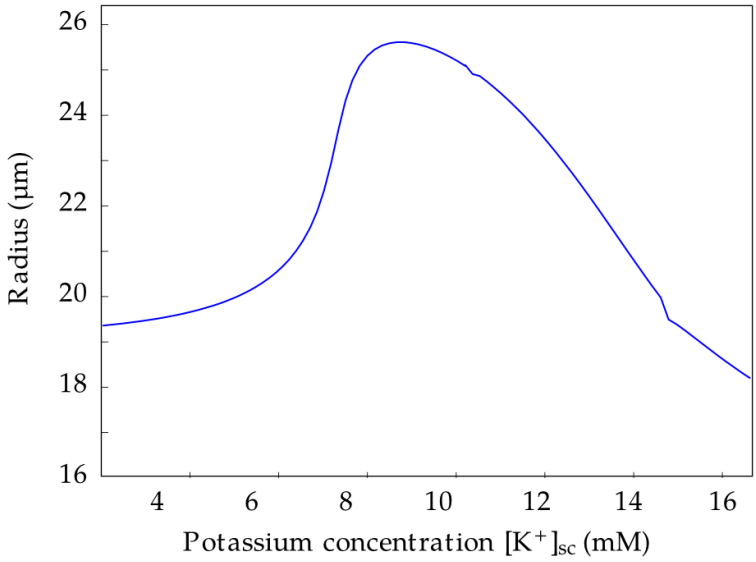

Figure 22: Perfusing artery radius variation as a function of K^+ in the synaptic cleft.

Figure 19h). Figure 23 shows the contribution of fluxes in and out of the SMC through Ca^{2+} channels and pumps. In the interest of clarity they are grouped into fluxes through the cell membrane (blue line) and fluxes in and out of the SR (red line). The sum of both shows that they balance each other for the steady state basal Ca^{2+} concentration and during the plateau activation phase (black line).

The first transient is determined by both the fluxes through the cell membrane and the SR fluxes (see Figure 23 b)). Here, the most influential flux of the former group is $J_{VOCC,i}$ and of the latter one is $J_{CICR,i}$ (results not shown). The second $[Ca^{2+}]_i$ transient is started by the membrane fluxes, but, with a delay of 5 s, mostly determined by the SR fluxes. This pronounced second spike leads to an overshoot of $[Ca^{2+}]_i$, but is balanced by a negative spike in the total flux at 609 s (see Figure 23 c)).

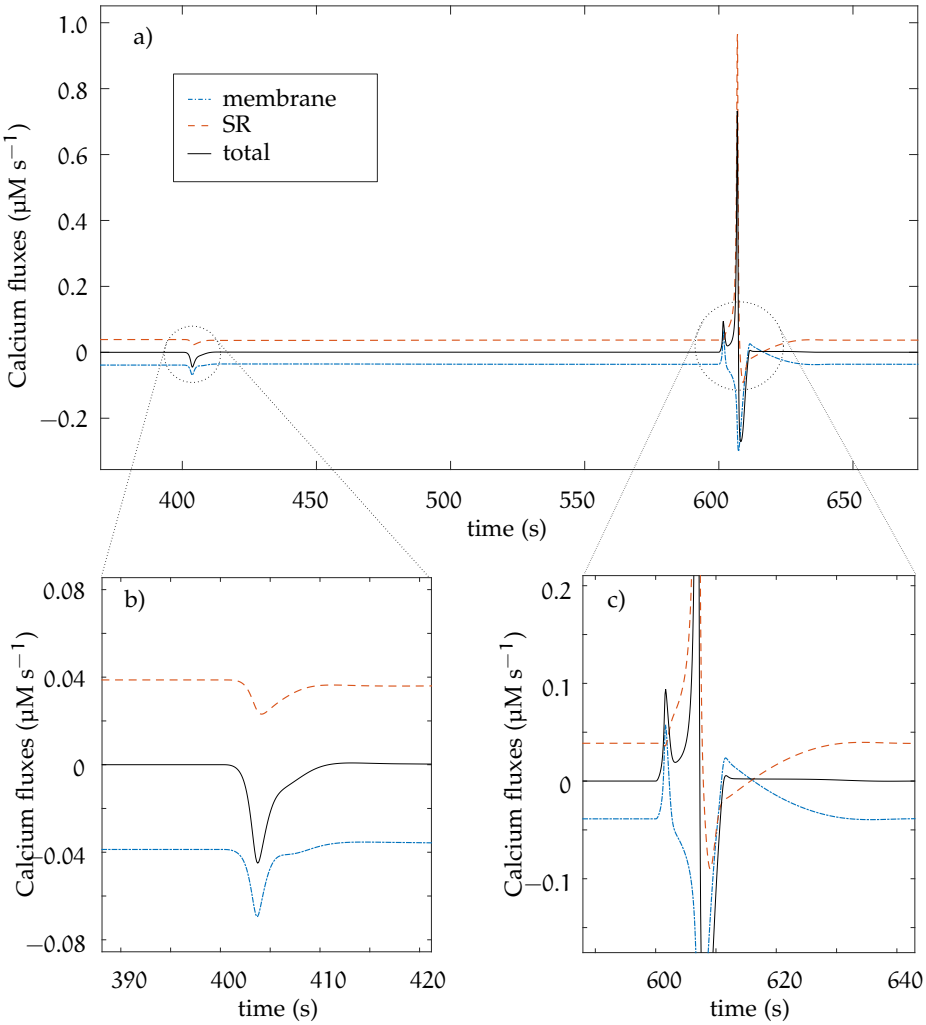

Figure 23: Ca^{2+} fluxes contributing to the cytosolic Ca^{2+} concentration. Neuronal activation occurs from 400 s to 600 s.

4.4 DISCUSSION

The present detailed biophysical model based on the K^+ and SMC Ca^{2+} pathway successfully simulates the vascular response upon neuronal activation. This was accomplished by further developing available models found in the literature and extending them to include additional ion channels, intercellular coupling and a mechanical model to describe temporal variations in

vessel diameter. It can be used to investigate different components and pathways of the complex NVC process.

This foundation model intentionally omits the Ca^{2+} dynamics in the AC and can therefore be used to investigate whether or not Ca^{2+} is a necessary ingredient in the set of neurovascular pathways for effective NVC.

Zonta et al. (2003) have indicated through experiment and Filosa and Blanco (2007) have suggested that arteriolar dilations are dependent on Glu-mediated Ca^{2+} in the AC. In complete contrast Nizar et al. (2013) have suggested through experiment with IP_3 type-2 receptor knock-out mice that astrocytic Ca^{2+} does not mediate NVC and that stimulus-induced dilation precedes Ca^{2+} variations.

The current model does not include Ca^{2+} dynamics in the astrocyte in contrast to the experiments of Filosa et al. (2004) and the model of Farr and David (2011). However, in comparison to the published work by Filosa et al. (2004) where *in vitro* studies showed that astrocytic cytosolic Ca^{2+} increased under neuronal stimulation and inhibited spontaneous vasomotion, the work by Nizar et al. (2013) using IP_3 receptor knock-out mice indicated that Ca^{2+} is not necessary for neurovascular coupling. Our model supports this. This is not however to assert that Ca^{2+} is not required at all since it plays a crucial role in the production of EET and 20-HETE, mediators of dilation and contraction of the arteriole, respectively (Hadfield et al., 2013). Unpublished work by our group and the analysis of Gonzalez-Fernandez and Ermentrout (1994) indicates that the dynamics of the BK channel when an average value of cell Ca^{2+} is assumed is essentially the same as when cell Ca^{2+} is fully taken into account. This provides some indication that Ca^{2+}, although varying in the astrocyte during neuronal activation, may not be necessary for NVC, in support of Nizar et al. (2013).

Additionally, there has been a considerable number of experiments outlining the importance of astrocytic Ca^{2+} in NVC, whereas the current model makes clear that this pathway is not the only one mediating NVC. Indeed LeCrux and Hamel (2011) have made clear the non-additive effects of pathways indicating possible parallel mediation of the perfusion response. This implies a careful development and subsequent study of more complex mathematical models to include the activation of phospholipases, production of arachidonic acid (AA) mediating both COX and cytochrome P450 pathways for dilation as well as the production of 20-HETE for constriction and that of the vasodilator NO. The VOCC channels are, due to the hyperpolarisation from K^+ SMC efflux, almost entirely closed and do not seem to play a significant role during neuronal activity.

The dilation of the blood vessel, as a result of neuronal activity, is of the expected order of magnitude. As determined from experimental data in the literature (Berridge, 2008), the time between neuronal activation and the vessel response is around 5 seconds. However, in the initial NVC Model the time between a neuronal input signal and the maximum vessel response is approximately 20 seconds. This longer response time is caused by the Hai and Murphy latch state model reaction rates, where the intracellular Ca^{2+} concentration influences the fraction of phosphorylated myosin cross bridges. The rate constants in this model are based on experimental results from swine carotid smooth muscle cells (Hai and Murphy, 1989), and although there is no evidence to strengthen this suggestion it is likely that human cerebral vascular smooth muscle cells compared to the carotid artery have different rate constants for the phosphorylation of myosin cross bridges.

4.5 CONCLUSION

A numerical model of NVC is presented based on neuronal activity coupled to vasodilation/contraction models *via* the astrocytic mediated perivascular K^+ and the SMC Ca^{2+} pathway. The model is able to relate a neuronal input signal to the corresponding vessel reaction.

This 'foundation' model of an NVU can be used to investigate the basic mechanisms found in NVC and it also forms a framework for model extensions to further investigate the complexities of NVC, and importantly its relationship to neuro-degenerative diseases such as Alzheimer's disease.

The present model shows that astrocytic Ca^{2+} is not necessary for neurovascular coupling to occur, in contrast to a number of experiments outlining the importance of astrocytic Ca^{2+} in NVC, whereas the current model makes clear that this pathway is not the only one mediating NVC.

Future work will include other signalling pathways and the growing importance of cerebral arteriolar blood fluid dynamics on cerebral perfusion. Finally, work will need to progress in the important area of blood flow and its feedback effect *via* agonists such as ATP and adenosine.

5

MODEL EXTENSION: LUMINAL AGONISTS INFLUENCE

5.1 INTRODUCTION

The flow of blood provides a spatially varying concentration of agonists, such as ATP, *via* convection and diffusion and the release from red blood cells by fluid shear stress. These agonists activate P2Y receptors, a family of purinergic G protein-coupled receptors, situated on the luminal side of the ECs surface. Upon activation P2Y receptors provide an IP_3 signalling pathway *via* the membrane bound PLC (Keizer and De Young, 1992), thus allowing information on the blood flow environment to pass to the NVU and influencing the NVC mechanism. The SMC, which forms the contractile unit of the system, therefore receives input from both neuronal activity *via* the AC and indications of the state of blood flow from the endothelium. ATP is one of the most important luminal agonists. It acts on P2Y receptors, providing a flux of IP_3 into the endothelial cytosol. This concentration of IP_3 is transported *via* hetero-cellular connexin GJs between ECs and SMCs (Haddock et al., 2006). Cells can change their dynamical state by transporting IP_3 through these gap-junctions. IP_3 can mediate CICR from intracellular Ca^{2+} stores (SR). This was originally mathematically described by Endo et al. (1970) and used subsequently by a number of models, notably that of Goldbeter et al. (1990) and Parthimos et al. (1999). Work on the coupling of ECs and SMCs by Koenigs-

berger et al. (2005, 2006) is based on the model developed by Parthimos et al. (1999). CICR provides a mechanism for the oscillatory behaviour of the cytosolic Ca^{2+} concentration in the SMC (Keener and Sneyd, 2009).

The NVU foundation model (chapter 4) can be extended with the luminal agonist and IP_3 signalling pathway to investigate the influence of agonist concentration in flowing blood, thereby providing information on the role that endothelial receptors play in NVC.

5.2 METHODS

For this model extension the SMC/EC subsystem of the NVU foundation model is most relevant (see subsection 4.2.2).

There are effectively two inputs to this subsystem: The KIR channel on the SMC facing the PVS and allowing a flux of K^+ into the cytosol, and the influx of IP_3 into the EC by virtue of the luminal agonist P2Y receptors on the EC membrane.

The input from KIR channel, which models the connection between the NE/AC and SMC/EC subsystems *via* the PVS, is discussed in chapter 4. The second input to the SMC/EC subsystem is that of IP_3 generation in the EC due to the activation of membrane receptors by agonists flowing in the arteriolar lumen. IP_3 mediates the J_{IP_3} channel in both the EC and SMC, situated on the surface of the endoplasmic (EC) and sarcoplasmic reticulum (SMC). This allows Ca^{2+} to be released from the reticulum. With certain IP_3 concentrations inside either the SMC or EC compartments, Ca^{2+} oscillations can occur due to CICR from intracellular Ca^{2+} stores (Goldbeter et al., 1990; Koenigsberger et al., 2005). We treat the production of IP_3 in the EC given by J_{EC,IP_3} as

emanating from the P2Y receptors (via a membrane bound G-protein and PLC).

Physiologically, endothelial cells and smooth muscle cells are connected by hetero- and homocellular gap junctions that allow an intercellular exchange of molecules and voltage. Since in the NVC model only one compartment is modelled, the homocellular exchange between cells is neglected. The heterocellular exchange is implemented by the following linearised coupling fluxes: $J_{Ca^{2+}_{cpl}}$, $J_{V_{cpl}}$ and $J_{IP_{3_{cpl}}}$ for Ca^{2+}, voltage and IP_3 coupling, respectively. These coupling functions are given by

$$\begin{aligned} J_{Ca^{2+}_{cpl}} &= -P_{Ca^{2+}}([Ca^{2+}]_i - [Ca^{2+}]_j) \\ J_{V_{cpl}} &= -G_v(V_i - V_j) \\ J_{IP_{3_{cpl}}} &= -P_{IP_3}([IP_3]_i - [IP_3]_j) \end{aligned} \tag{5.1}$$

where the subscripts i and j correspond to EC and SMC, respectively.

Barrio et al. (1997) investigated the voltage-gating properties of connexin-43 junctions and indicated that the conductance of the hemi-channel was voltage mediated. However, for this particular model, we treat $P_{Ca^{2+}}$, G_v and P_{IP_3} as constants. This can be seen as modelling the simple diffusional flux rather than the more complete electro-diffusional flux which allows for ion drift. In the SMC/EC subsystem, calcium buffering is implemented, and corrects for the fact that approximately 1% of the intracellular Ca^{2+} is "free" (Parthimos et al., 1999).

We chose two representative values ((Shaikh et al., 2011)) for each coupling coefficient giving 8 cases which are listed in Table 4.

Haddock et al. (2006) have shown the existence of myoendothelial gap junctions comprised of connexins 37 and 40 in the rat basilar artery. However, there is very little information on the values of coupling permeabilities

Table 4: Coupling coefficients for Ca^{2+} coupling, voltage coupling and IP_3 coupling, respectively (Shaikh et al., 2011; Koenigsberger et al., 2005; Diep et al., 2005).

CASE	G_V (s^{-1})	$P_{Ca^{2+}_{cpl}}$ (s^{-1})	P_{IP_3} (s^{-1})
0	0	0	0
1	0.5	0	0.05
2	0.5	0.05	0.05
3	0	0	0.05
4	0.5	0.05	0
5	0.5	0	0
6	0	0.05	0
7	0	0.05	0.05

for these connexins. In addition, Diep et al. (2005) suggested that IP_3 coupling is favoured over both membrane or Ca^{2+} coupling. Additionally, Charles et al. (1992) showed very little in Ca^{2+} coupling (albeit in astrocytes) and later Charles et al. (2002) indicated that ATP transport through hemichannels mediated Ca^{2+} coupling. In the light of this we have chosen the coupling coefficients to reflect the evidence so far available in the public domain. Shaikh et al. (2011) has used coupling coefficients for connexins 37 and 40 and we take these as values for the cases presented below. We should note that the coupling coefficient given by Koenigsberger et al. (2006) for membrane coupling is high, with a value of 50 s^{-1}. Tests showed that using a value of this magnitude effectively clamped the SMC at the membrane voltage of the EC and shut off the voltage operated calcium channels. This would cause full dilation of the arteriole regardless of any neuronal input. In addition the myo-endothelial junction conductance is to a great extent proportional to the surface area of the junction itself. In the light of this and the work by Diep et al. (2005) we reduce this figure to 0.5 s^{-1}.

5.3 RESULTS

5.3.1 *Luminal Agonist Influence on Neurovascular Coupling*

The results of the full NVC model for CASE 2 are shown in Figures 24a to 24d with the IP_3 production rate of J_{EC,IP_3} set at 0.18 $\mu M s^{-1}$ and at 0.4 $\mu M\ s^{-1}$. For the case presented in this figure the coupling fluxes $P_{Ca^{2+}_{cpl}}$, G_V and P_{IP_3} have values 0.5, 0.05 and 0.05 (s^{-1}), respectively.

During neuronal stimulation (t = 100 s to 200 s) SMC hyperpolarisation decreases the influx of Ca^{2+} through the voltage operated calcium channel (Figure 24b). It is at this point that the variation in the J_{EC,IP_3} makes itself felt. For the J_{EC,IP_3} = 0.18 $\mu M\ s^{-1}$ simulation the VOCC flux is small and the influx of IP_3 into the EC and hence into the SMC *via* coupling is too low to induce the SMC into an oscillatory state. The SMC cytosolic Ca^{2+} remains low and the SMC contraction force diminishes, allowing the artery to dilate as shown in Figure 24d. For the case where J_{EC,IP_3} = 0.4 $\mu M\ s^{-1}$, the IP_3 concentration in the SMC is high enough to induce an efflux of Ca^{2+} from the stores and mediate the CICR process, providing an oscillatory state even though the VOCCs are effectively closed. In this contrasting situation the "average" Ca^{2+} is higher and thus the contraction force greater, thereby reducing the radius to a lower value as shown in Figure 24d.

5.3.2 *IP_3 Production Rate Constant and Myoendothelial Coupling*

From the results shown in Figures 24a to 24d we see that IP_3 has a significant influence on the time dependent radial profiles of the arteriole. Figure 25 shows two cases (2 and 4) where the IP_3 coupling between the EC and SMC

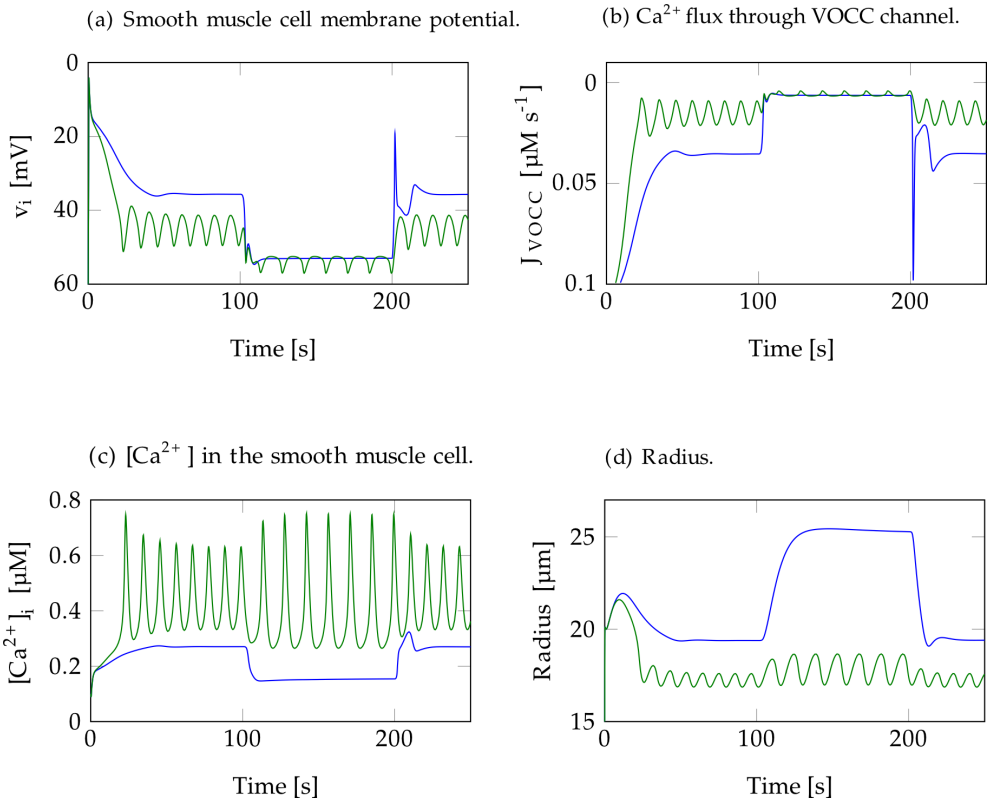

Figure 24: CASE 2 - G_V = 0.5 s^{-1}, $P_{Ca^{2+}}$ = 0.05 s^{-1}, P_{IP_3} = 0.05 s^{-1}; blue line: J_{EC,IP_3} = 0.18 µM s^{-1}, green line: J_{EC,IP_3} = 0.4 µM s^{-1}

is changed from 0.05 s^{-1} (CASE 2) to 0.0 s^{-1} (CASE 4). Where the coupling is zero the profiles for both J_{EC,IP_3} production rates are similar with that for J_{EC,IP_3} = 0.18 µM s^{-1}, providing a slightly lower maximum radius change. Since the coupling coefficients are non-zero (CASE 2; Figure 25a), the EC is diffusing IP_3 into the SMC for non-zero values of the J_{EC,IP_3} flux. At a higher production rate of J_{EC,IP_3} = 0.4 µM s^{-1} the basal radius is lower and the relative dilation is smaller compared to that obtained at J_{EC,IP_3} = 0.18 µM s^{-1}. It is also in a permanent oscillatory state.

The intracellular Ca^{2+} concentration in the smooth muscle cell is either constant or in an oscillatory state for different IP_3 production rate constants. As a result of these oscillations, the radius, membrane voltage and all the

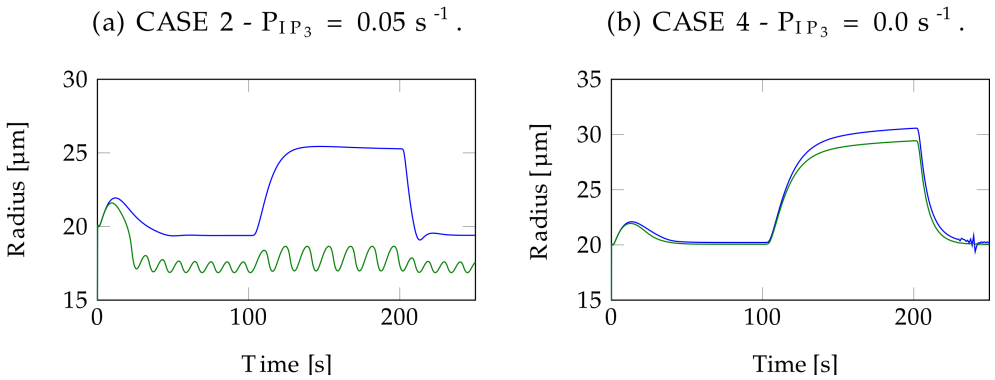

Figure 25: Radius profiles at different CASEs 2 and 4 showing the influence of IP_3 coupling. Blue line - J_{EC,IP_3} = 0.18 µM s^{-1}, green line - J_{EC,IP_3} = 0.4 µM s^{-1}.

fluxes through the Ca^{2+} and voltage mediated channels also oscillate. These intracellular Ca^{2+} oscillations in the smooth muscle cell start when the Ca^{2+} efflux through the IP_3 mediated Ca^{2+} channel in the sarcoplasmic reticulum, J_{IP_3}, is large enough to activate the calcium induced calcium release (CICR) channel residing on the sarcoplasmic reticulum membrane. This activation results in a large efflux of Ca^{2+} from the stores in the sarcoplasmic reticulum into the cytosol, which is represented by an increase in frequency of the Ca^{2+} oscillations (Berridge, 2008; Wu and Marx, 2010).

However, due to the increase of intracellular Ca^{2+} concentration, the Ca^{2+} mediated K^+ channel, J_{K_i}, starts pumping out more K^+. Again, this hyperpolarises the membrane voltage and decreases the flux through the voltage operated calcium channel (VOCC), decreasing the cytosolic Ca^{2+} concentration. The CICR channel initially relies on the flux of IP_3 via the myoendothelial gap junction coupling between SMC and EC, since this flux increases the release of cytosolic Ca^{2+} from the SR stores. Oscillations occur under relatively large values of J_{EC,IP_3} (for some non-zero value of the IP_3 coupling coefficient).

To examine which IP_3 production rate, J_{EC,IP_3}, is large enough to activate the CICR channel, the model is run for J_{EC,IP_3} from 0 to 0.8 µM s^{-1}. The

results of these simulations are shown in Figure 26.

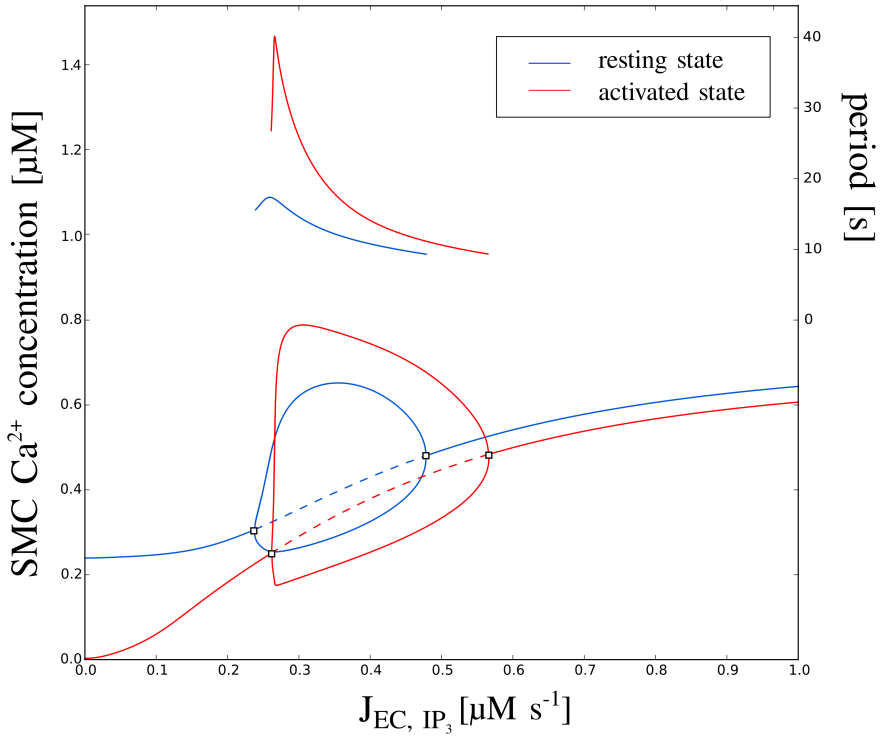

Figure 26: Calcium bifurcation diagramm for CASE 2. Squares show Hopf bifurcations. Red - activated state, blue - resting state. (Figure was produced using the continuation and bifurcation software AUTO-07P.)

The blue line in Figure 26 represents the intracellular Ca^{2+} concentration as a function of J_{EC,IP_3} without the presence of a neuronal pulse and the red line represents the Ca^{2+} concentration during a neuronal pulse. It is not yet clear as to whether the initiation of oscillations (J_{EC,IP_3} = 0.223 µM s^{-1} for blue and J_{EC,IP_3} = 0.26 µM s^{-1} for red) are Hopf bifurcations although they seem to be supercritical in form.

To investigate the relationship of the arteriolar radial motion the model is run using the data of CASE 2 for various values of the IP_3 coupling flux $J_{IP_{3_{cpl}}}$. Figure 27 shows the maximum and minimum radius values of the arteriole plotted against the IP_3 coupling coefficient for both cases (with and

without neuronal input). Again, we find constant and oscillatory domains for the radius values during, and without, neuronal pulse.

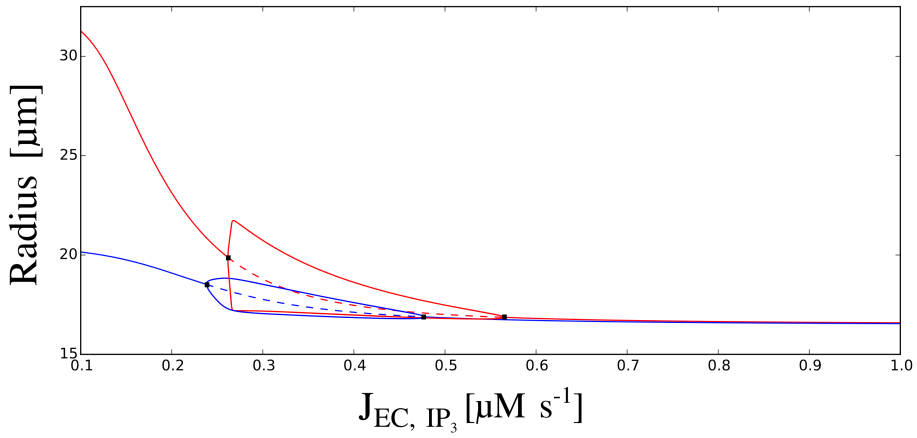

Figure 27: Radius bifurcation diagramm for CASE 2. Squares show Hopf bifurcations. Red - activated state, blue - resting state. (Figure was produced using the continuation and bifurcation software AUTO-07P.)

5.4 DISCUSSION

This model extension further develops the NVC 'foundation' model of chapter 4 by extending it to include variations in luminal agonist concentrations and coupling coefficients between the SMC and EC using different combinations (coupling cases).

Significant mathematical analysis of the dynamics of this large and complex system is not possible. However, wherever possible discussion will provide some indications of dynamic behaviour, including points of bifurcation.

In the interests of comparison CASE 2 is considered to be a "standard", though this does not necessarily imply a normal physiological condition, but one by which other states may be analysed. Results show that the time-dependent profiles for K^+ in the synaptic cleft and the perivascular space

(see Figure 19a and Figure 19d) follow each other and are independent of the value of J_{EC,IP_3}. This is to be expected as the model does not include diffusion through the cell (lumped parameter assumption). In contrast to the membrane potential, significant differences arise for the cytosolic Ca^{2+} concentration and the CICR Ca^{2+} flux (see Figure 28) when the J_{EC,IP_3} values vary between 0.18 µM s^{-1} (shown in blue in the figures) and 0.4 µM s^{-1} (shown in green). For J_{EC,IP_3} = 0.18 µM s^{-1} no oscillations occur and the arteriole vessel dilation during the neuronal activity is considerable, being of the order of 40%. The SMC VOCC and CICR fluxes (mediated by the coupled IP_3) are small (almost zero) incurring a low cytosolic Ca^{2+} concentration of approximately 0.3 µM. This allows the smooth muscle cell (via the 4-state latch model (Hai and Murphy, 1989)) to dilate. Figure 24b shows the VOCC flux for both J_{EC,IP_3} = 0.18 µM s^{-1} and 0.4 µM s^{-1}. We see no significant difference in VOCC flux between these two cases since the membrane potential remains essentially the same. Haddock et al. (2006) state that myoendothelial voltage coupling mediates vasomotion. However, their experiments utilised brain slices and are therefore considered to be of type *in vitro*, excluding the influence of the luminal agonists in flowing blood. Additionally, the present model shows that the membrane potential of the SMC varies very little between the two values of the J_{EC,IP_3}, whilst comparisons of results from CASE 2 versus CASE 7, CASE 1 versus CASE 3, CASE 6 versus CASE 4 and CASE 5 versus CASE 0 (results not shown) show no difference, strengthening the argument for IP_3 coupling as the major contributor.

For the case of J_{EC,IP_3} = 0.4 µM s^{-1} a completely different dynamic state is apparent. Oscillatory behaviour occurs especially for cytosolic Ca^{2+} with variations between 0.3 µM and 0.7 µM. Although large Ca^{2+} variations exist their average value varies very little and induces only a small increase in radius. It is noted that during steady state prior to neuronal activity (50 <

$t < 100$) Ca^{2+} levels are significantly higher than for the case of J_{EC,IP_3} = 0.18 μM s^{-1}. The membrane potential, although oscillatory in form, does not vary significantly from the J_{EC,IP_3} = 0.18 μM s^{-1} case.

We ascribe these differences in Ca^{2+} concentration to the influence of the IP_3 coupling. Since for a wide range of physiological values of J_{EC,IP_3} the VOCC and leak flux are small both before and during neuronal activation thus any variations in $[Ca^{2+}]$ emanate from the sarcoplasmic reticulum.

The rate of change of $[Ca^{2+}]$ is directly proportional to the concentration of IP_3 in the SMC, $[IP_3]_i$, with the release of calcium from IP_3-sensitive stores in the SMC given as

$$J_{IP_{3i}} = F_i \frac{[IP_3]_i^2}{K_{ri}^2 + [IP_3]_i^2} \tag{5.2}$$

whilst the calcium-induced calcium release (CICR) is

$$J_{CICR_i} = C_i \frac{[\widehat{Ca^{2+}}]_i^{\,2}}{s_{ci}^2 + [\widehat{Ca^{2+}}]_i^{\,2}} \frac{[Ca^{2+}]_i^{\,4}}{c_{ci}^4 + [Ca^{2+}]_i^{\,4}}\,, \tag{5.3}$$

were $[Ca^{2+}]_i$ and $[\widehat{Ca^{2+}}]_i$ are the Ca^{2+} concentration in the cytosol and in the stores, respectively, as noted in equations given in the Appendix.

Oscillations from the CICR mechanism first stated by Endo et al. (1970) are due to the positive feedback by cytosolic Ca^{2+}. That is, oscillations were regulated by the cycling of calcium between the IP_3-insensitive store and the cytosol. Calcium released from the IP_3-sensitive pool regulated the cyclic calcium release from the IP_3-insensitive pool. For the oscillatory condition the frequency decreases during neuronal activity. The above equations (5.2) and (5.3) show clearly the influence that IP_3 has on the cytosolic Ca^{2+} and thus any vessel radius variation. Figure 28 compares the (CASE 2) CICR flux for J_{EC,IP_3} = 0.18 μM s^{-1} and 0.4 μM s^{-1}. The time-averaged Ca^{2+} is approximately 0.41 μM prior to neuronal activity and 0.54 μM during

activity for J_{EC,IP_3} = 0.4 µM s^{-1} and for J_{EC,IP_3} = 0.18 µM s^{-1} is 0.1 µM prior, 0.013 µM during activity.

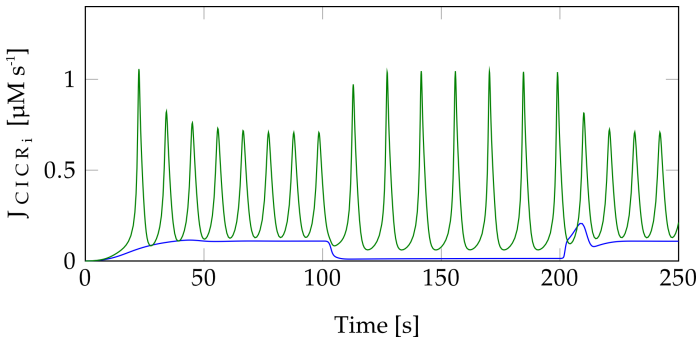

Figure 28: CICR flux for CASE 2. Blue line - J_{EC,IP_3} = 0.18 µM s^{-1}, green line - J_{EC,IP_3} = 0.4 µM s^{-1}.

For CASE 3 (voltage and Ca^{2+} coupling turned off, results not shown) similar comparisons occur although the oscillations are of a slightly higher magnitude. Experimental work in the feline thalamus by Rivadulla et al. (2011) indicate a dominant frequency of 0.14 Hz which is double that in our results as shown in Figure 24. This indicates the influence that the endothelium has through both IP_3 coupling and the IP_3 influx from J_{EC,IP_3}.

To complete the analysis of the influence of the endothelium, CASE 0 essentially removes this influence by decoupling the SMC and EC. For this case the basic profiles are profoundly different from the previous two cases. Firstly, we note that the steady state condition (no neuronal activity) is clearly the same for both values of J_{EC,IP_3} since there is no coupling from the EC. Secondly, the dilation caused by the neuronal input causes a change of vessel radius from 20 µm to approximately 33 µm compared to CASE 2 where the radius change is from 19 µm to 25.5 µm for J_{EC,IP_3} = 0.18 µM s^{-1}, and 17 µm to 18.5 µm for J_{EC,IP_3} = 0.4 µM s^{-1}. It is here that we see the direct influence of the agonist concentration in the lumen affecting the dilation/contraction characteristics of the cerebral vessel. Figures (25a) and (25b) clearly show that for a higher J_{EC,IP_3} value the dilation for a constant neur-

onal input signal produces a lower radial change. From previous studies (David, 2003; Comerford and David, 2008b) it is known that there is a distinct relationship between wall shear stress and the concentration of agonists (e.g. ATP) at the vessel wall (endothelial surface). In addition, there is evidence to suggest that P2Y (ATP) and P1 (adenosine) purinergic receptors exist in the cerebral vasculature and that ATP concentration is an increasing function of wall shear stress (Comerford and David, 2008a).

As shown in Figure 26, for low J_{EC,IP_3} the SMC Ca^{2+} increases monotonically and will clearly reduce any further dilation. As the arteriolar radius increases to allow an increase in oxygen and glucose to perfuse to the cerebral tissue, the wall shear stress increases and thereby induces a higher concentration of Ca^{2+} in the SMC *via* the J_{EC,IP_3}/ATP pathway. Additionally, fluid shear stress can cause ATP to be released from red blood cells, enhancing even further the ATP concentration and thus the cytosolic IP_3 concentration in the SMC. However, we recognise that this receptor function may act in concert with stretch activated channels located in the SMC, and additionally in opposition to the stress activated production of eNOS (Comerford and David, 2008b).

Increasing the concentration of IP_3 via the P2Y pathway induces oscillations in the arteriolar radius. Sakurai and Terui (2006) and Rücker et al. (2000) have shown that vasomotion can induce an increase in, or maintain perfusion into, the capillary bed under critical conditions, even though the perfusing arteriolar radius is effectively reduced. It is unclear as to whether this occurs in the cerebro-vasculature, but it is not unreasonable to suggest that this may happen. Therefore, the model supports a number of competing effects, all of which seem to suggest that perfusion is paramount under neuronal activity.

Our results indicate that for low values of the rate of IP_3 production (J_{EC,IP_3}) vasomotion is absent, whilst in the higher ranges an oscillatory phenomenon occurs. To understand this, there are essentially two pathways by which the smooth muscle cell can be induced to oscillate. Firstly, that of the relative rate of opening of calcium mediated potassium channels where the potassium open probability function acts as a relaxation parameter and the equilibrium state of the calcium channel is shifted to higher or lower values (Gonzalez-Fernandez and Ermentrout, 1994), and secondly, to the calcium-induced calcium release mechanism (CICR) from the sarcoplasmic reticulum first elucidated by Endo et al. (1970). In both cases L-type voltage mediated calcium channels play an important role since they allow the influx of calcium into the cell but depend on the concentration of extracellular calcium as shown in the *in vivo* experiments by Fuji et al. (1990).

In vivo experiments allow a "natural" condition to prevail. However, *in vitro* perfused brain slice experiments require a carefully defined Ca^{2+} concentration. The present model investigates predominantly the role of the CICR mechanism since it relies on the IP_3 concentration in the SMC emanating from the coupled EC. Further exploration is required to determine the balance between Ca^{2+} influx via L-type channels and SMC IP_3 concentration.

The complete NVC model shows, both with and without a neuronal input signal, one oscillatory domain as a function of varying J_{EC,IP_3} as indicated in Figure 26. However, the action of the neuronal signal shifts the oscillatory domain to the right (critical bifurcation points increased in J_{EC,IP_3} value). The dilation of the blood vessel, as a result of neuronal activity, is of the expected order of magnitude. As determined from experimental data in the literature (Berridge, 2008), the time between neuronal activation and the vessel response is around 5 seconds. However, in the initial NVC Model the time between neuronal input signal and the maximum vessel response is ap-

proximately 20 seconds. This larger response time is caused by the Hai and Murphy latch state model reaction rates, where the intracellular Ca^{2+} concentration influences the fraction of phosphorylated myosin cross bridges. The rate constants in this model are based on experimental results from swine carotid smooth muscle cells (Hai and Murphy, 1989) and although there is no evidence to strengthen this suggestion it is most likely that human cerebral vascular smooth muscle cells compared to the carotid artery have different rate constants for the phosphorylation of myosin cross bridges.

The present model shows the considerable effects of luminal agonists *via* the IP_3 pathway on neurovascular coupling.

5.5 CONCLUSION

In this study, we have presented an NVC model based on neuronal activity coupled to vasodilation/contraction *via* the AC-mediated perivascular K^+ and the smooth muscle cell Ca^{2+} pathway. The advantage of this NVC model is that it is able to relate a neuronal input signal to the corresponding vessel reaction. The model indicates that induced vasomotion by increased IP_3 induced calcium from the SMC stores and the resulting CICR oscillations would seem to inhibit neurovascular coupling. However, from previous results from Sakurai and Terui (2006) and Rücker et al. (2000) this may even enhance perfusion in the capillary bed. From results presented IP_3 seems to be important in the dynamics of the smooth muscle cell. The VOCC channels are, due to the hyperpolarisation from K^+ SMC efflux, almost entirely closed and do not seem to play a significant role during neuronal activity.

6

MODEL EXTENSION: NITRIC OXIDE SIGNALLING

6.1 INTRODUCTION

Cellular signalling involves numerous pathways and transmitter molecules. In 1980 Furchgott and Zawadzki discovered an endothelium-derived relaxing factor (EDRF) in the cardiovascular system. They found that this unknown signal molecule was only produced by an intact endothelium. Ignarro et al. (1987) later proved that EDRF was nitric oxide (NO) and that cyclic guanosine monophosphate (cGMP) is its second messenger. For these discoveries Robert F. Furchgott, Louis J. Ignarro and Ferid Murad were awarded the Nobel Prize in Medicine or Physiology in 1998.

The identification of NO as a vasodilating signalling molecule in cardiovascular, and especially also in neurovascular systems was a surprise to the scientific community, because it did not fit into the traditional definition of neurotransmitters since it is not produced in advance and stored. Furthermore, due to its small size NO diffuses widely and readily in all three dimensions and is not limited to local effects, which sets it apart from other central nervous system signalling molecules. It is extremely diffusible in both aqueous and lipid environments which allows rapid spreading even through membranes. Nevertheless, NO is an unstable gaseous free radical

and therefore has a very short half-life, which limits its activity temporally (Garthwaite and Boulton, 1995; Dobutovic et al., 2011).

NO is known to be produced in a large number of different tissues playing a wide variety of physiological roles, including relaxation of blood vessels (Dawson et al., 1991; Alderton et al., 2001). However, it still is not fully understood as to how exactly NO contributes to NVC and particularly which source of NO plays the major role (Butler and Nicholsson, 2003). The biochemical reaction that synthesises NO is catalysed by the enzyme family of nitric oxide synthases (NOS) (Förstermann et al., 1998; Alderton et al., 2001; Rafikov et al., 2011).

In mammals, three isoforms of NOS have been identified: neuronal (nNOS), mainly expressed in neurons, endothelial (eNOS), mainly expressed in EC, and inducible (iNOS), a transcriptionally regulated enzyme, which is present in multiple cell types (Förstermann et al., 1998). Literature suggests different NO production rates ranging from $0.035\,\mu M\ s^{-1}$ up to $68\,\mu M\ s^{-1}$ (Chen and Popel, 2006). All isoforms have important biological functions, strongly linked with their location and output, and it has been suggested that changes in their expression may have physiological and pathophysiological consequences (Förstermann et al., 1998). Their layout of catalytic domains is similar to a C-terminal reductase and an N-terminal oxygenase section, including binding sites each for calmodulin (CaM), L-arginine (L-Arg) and for several cofactors (Mayer and Hemmens, 1997). The catalytic activity of the constitutively expressed isoenzymes, nNOS and eNOS, is regulated by the intracellular calcium (Ca^{2+}) that builds a complex with CaM, but evidence indicates that these enzymes are also regulated by other factors such as physical stimuli (Forsythe et al., 2001).

The physiological role of NO is still a matter of debate (Attwell et al., 2010) and the molecule has been described to have a "Janus-faced" character (För-

stermann, 2006; Calabrese et al., 2007): NO can act either neuroprotectively by controlling the vascular smooth muscle tone and blood flow, thereby preventing ischaemic cell injury, or neurotoxically leading to severe cerebral degeneration. Literature suggests that the production source and quantity determines the character of its functioning (Zorrilla-Zubilete et al., 2010). This emphasises the necessity of a functional model that predicts NO release from different cell types and its biophysical influence, ideally including vessel control and interaction with feedback from wall shear stress (wss), intracellular Ca^{2+} levels, and oxygen delivery and consumption (Buerk, 2001).

Because of its high diffusivity, it is difficult to measure the exact NO production and concentration experimentally. Mathematical modelling can hence be a useful tool to elucidate physiological processes and guiding directions for further experiments.

6.2 MODEL DEVELOPMENT

The potential of NO as an important vasodilating messenger molecule is assessed using a holistic mathematical model that includes the dynamics of NO in the NVU. With the help of this model the most crucial signalling pathways are analysed and the influence of NO in NVC investigated, including the localisation of the main contributing source.

Therefore, our previous foundation NVU model (Farr and David, 2011; Dormanns et al., 2014) is extended by mathematical equations that represent production, diffusion and consumption of NO in different cell types, as well as the interaction of NO with other biochemical species and ion channel open probabilities.

As in the previous models of an NVU (Farr and David, 2011; Dormanns et al., 2014) we divide the full model into seven compartments: the neuron (NE), the synaptic cleft (SC), the astrocyte (AC), the perivascular space (PVS), the smooth muscle (SMC) and endothelial (EC) compartments, and the arteriolar lumen (LU). The compartments are coupled predominantly by ion fluxes through ion channels, and membrane potential differences.

Our NO model focusses on NO production by the two constitutive isoforms of nitric oxide synthase, nNOS and eNOS (Fleming and Busse, 1999). Both enzymes' activation is mediated by intracellular Ca^{2+} in the NE and EC, respectively. In addition, eNOS gets activated by blood flow induced wall shear stress in cerebral arterioles (Joannides et al., 1995).

Due to its high diffusion coefficient NO diffuses rapidly into other compartments, shown in experiments (Malinski et al., 1993) and in kinetic simulations (Lancaster, 1994). When NO reaches the SMC it interacts with intracellular enzyme activation and regulates SMC relaxation (Yang et al., 2005).

A schematic representation of the compartments and the NO signalling pathway in the NVU is given in Figure 29, spanning NO synthesis in the NE and the EC through to the relaxation of the SMC.

The dynamics of NO in the involved compartments are described mathematically using mass balance formulations. The concentration of NO in each domain is determined by the balance between production flux $p_{NO,m}$, consumption flux $c_{NO,m}$ within the cell, i.e. the reaction with oxygen or other molecules, and the diffusive flux $d_{NO,m}$ from and into other compartments.

The NO concentration $[NO]_m$ is given by the solution of the following generic first-order non-linear differential equation:

$$\frac{d[NO]_m}{dt} = p_{NO,m} - c_{NO,m} + d_{NO,m} \,, \tag{6.1}$$

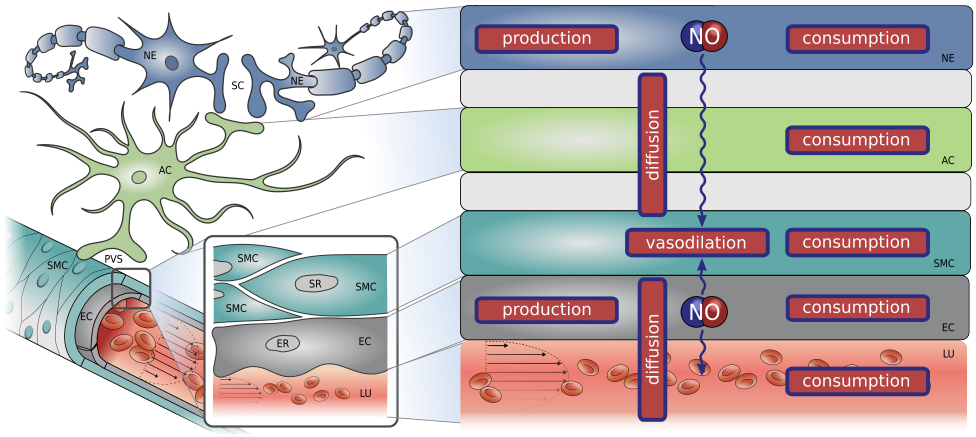

Figure 29: NO signalling pathway in NVC. NO is produced in the neuron (NE) and the endothelial cell (EC) and diffuses into other compartments, where it gets consumed by chemical reactions. In the smooth muscle cell (SMC) it leads to relaxation and therefore vasodilation. SC - Synaptic cleft, AC - Astrocyte, ER - Endoplasmic reticulum, PVS - Perivascular space, SR - Sarcoplasmic reticulum, LU - Lumen.

where $m \in \{n, k, i, j\}$ denotes the cell indices for NE, AC, SMC and EC, respectively.

6.2.1 *Nitric Oxide Production*

The production rate of NO is dependent on the concentration of activated nitric oxide synthase. L-Arginine (L-Arg), oxygen (O_2) and nicotinamide adenine dinucleotide phosphate (NADPH) are the biochemical substrates needed for the NO production (Chen and Popel, 2006), where L-Arg is the requisite and sole nitrogen donor (Forsythe et al., 2001). L-Arg is oxidated to L-Citrulline and the biochemical reaction leads to the production of $NADP^+$, water and NO. This five-electron oxidation reaction takes place in two steps. The overall stoichiometric chemical formula reads as follows:

$$\text{L-Arg} + 2O_2 + \frac{3}{2}\text{NADPH} \xrightarrow{\text{NOS}} \text{L-Citrulline} + \frac{3}{2}\text{NADP}^+ + 2H_2O + \text{NO}\,.$$

For the reaction several biomolecule cofactors such as flavin mononucleotide (FMN), flavin adenine dinucleotide (FAD) and tetrahydrobiopterin (H_4B) are needed.

The constitutive NOS isoforms nNOS and eNOS are thought to be the most influential NO producers and are critical for maintenance of homeostasis (Fleming and Busse, 1999; Forsythe et al., 2001). For this reason we assume NEs and ECs to be the predominant producers of NO and assume no production in other cell types, hence $p_{NO,k}$, $p_{NO,i} = 0$.

6.2.1.1 *Neuronal Nitric Oxide Production*

NO synthesis in the NE is catalysed by nNOS in response to glutamate-induced calcium influx into the post-synaptic neuron. An overview of the model detail is given in Figure 30.

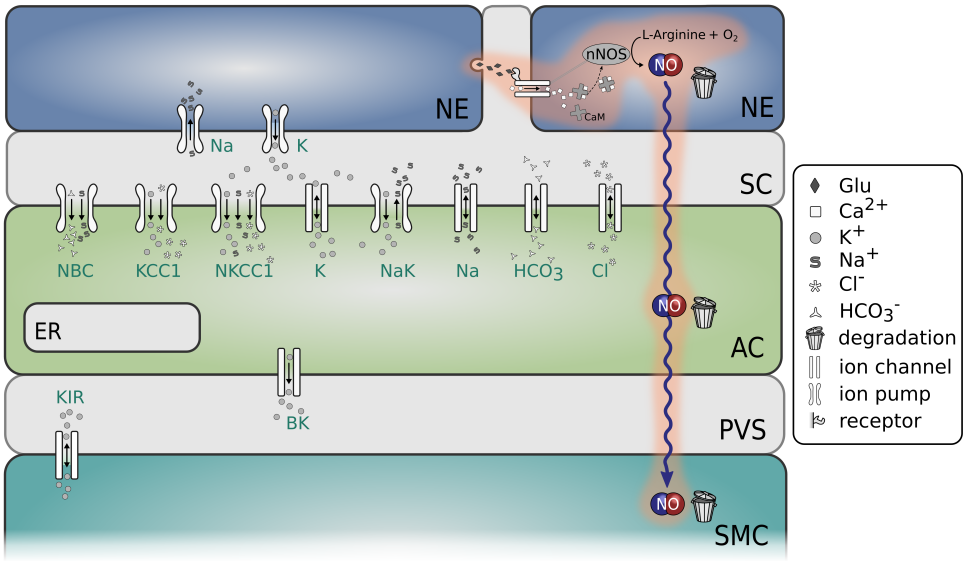

Figure 30: Graphical representation of the mathematical model, detail. The biochemical reaction that produces NO in the NE is catalysed by the enzyme nNOS and depends on the available concentration of L-Arg and O_2. The model addition to our previous foundation model (Dormanns et al., 2014) is highlighted. NE - Neuron, SC - Synaptic cleft, AC - Astrocyte, PVS - Perivascular space, SMC - Smooth muscle cell.

The NO production in the NE depends on the amount of activated nNOS $[nNOS_{act}]$ (Förstermann et al., 1998) and is limited by the availability of the substances O_2 and L-Arg (Chen and Popel, 2006). We express it mathematically as

$$p_{NO,n} = p_{max} \frac{[O_2]_n}{K_{m,O2,n} + [O_2]_n} \frac{[\text{L-Arg}]_n}{K_{m,\text{L-Arg},n} + [\text{L-Arg}]_n} , \tag{6.2}$$

where p_{max} is the maximum neuronal production rate and given by

$$p_{max} = V_{max,NO,n} [nNOS_{act}]_n , \tag{6.3}$$

with the maximum nNOS catalytic rate $V_{max,NO,n}$ and the neuronal O_2 and L-Arg concentrations, $[O_2]_n$ and $[\text{L-Arg}]_n$, respectively. $K_{m,O2,n}$ and $K_{m,\text{L-Arg},n}$ are the associated Michaelis constants (Chen and Popel, 2006, 2007).

The nNOS activation in the NE is triggered by the chemical neurotranstimnter glutamate (Glu) in response to neuronal activation. In a chemical synapse, when an action potential reaches the axon terminal of the presynaptic NE, it allows the release of Glu from vesicles into the SC which then binds to Glu-sensitive receptors of the postsynaptic NE's dendrite and is subsequently removed from the SC by diffusion and hydrolysis (Keener and Sneyd, 2009).

As a stimulation input to the model we give a Glu concentration of 1850 µM into the SC during neuronal activation, which corresponds to the release of a Glu vesicle into the SC with a volume of 0.0018 μm^3 (Santucci and Raghavachari, 2008). Before and after stimulation we assume a zero value of $[Glu]_{sc}$.

Neuronal NOS is often colocalised with ionotropic N-methyl-D-aspartate receptors (NMDA-Rs, Mayer and Hemmens, 1997; Förstermann et al., 1998; Bredt, 2003), which are receptor complexes including transmembrane ion channels in the NE that are opened or closed in response to the binding of

Glu (Benarroch, 2006). These channels provide Ca^{2+} influx into the cytosol. The two subtypes of NMDA-Rs, NR2A and NR2B, show different opening probability kinetics and expressed values. Within different subunits we model the open probabilities w of NMDA-Rs with dependencies on neuronal Glu concentration using Michaelis-Menten kinetics to fit the experimental data from Santucci and Raghavachari (2008):

$$w_{NR2,i} = \frac{[Glu]_{sc}}{K_{m,i} + [Glu]_{sc}} \; i \in \{A, B\}\,, \tag{6.4}$$

where $K_{m,A}$ and $K_{m,B}$ are fitted Michaelis constants.

At open state NMDA-Rs are highly permeable to calcium ions (Jahr and Stevenst, 1993). The equation for the neuronal inward calcium current I_{Ca} in femtoamps (fA) per open NMDA-R is given by Santucci and Raghavachari (2008):

$$I_{Ca} = \frac{4\nu_n G_M (P_{Ca}/P_M)([Ca^{2+}]_{ex}/[M])}{1 + \exp(\alpha_\nu(\nu_n + \beta_\nu))} \frac{\exp(2\nu_n F/(R_{gas}T))}{1 - \exp(2\nu_n F/(R_{gas}T))} \tag{6.5}$$

where F is Faraday's constant, ν_n is the neuronal membrane potential (assumed to be constant during activation, an average value of the neuronal spiking activity of multiple action potentials. This is a simplified mathematical description, but suitable for our purpose as the model is focusing on Glu-effected Ca^{2+} changes in the NE), G_M is the conductance, P_{Ca}/P_M the ratio of the NMDA-R permeabilities to Ca^{2+} and to monovalent ions, respectively, $[Ca^{2+}]_{ex}$ the external Ca^{2+} concentration, [M] the concentration of monovalent ions (intra- and extracellular), α_ν and β_ν are translation factors, T is the temperature, and R_{gas} is the universal gas constant.

Santucci and Raghavachari (2008) arrive at estimates of 0.63 NR2A- and 11 NR2B-NMDA-Rs, on average, per synapse (Santucci and Raghavachari, 2008). Therefore, the total calcium current $I_{Ca,tot}$ reads as follows:

$$I_{Ca,tot} = I_{Ca}(0.63w_{NR2,A} + 11w_{NR2,B}) \, . \tag{6.6}$$

The rate of change in neuronal cytosolic Ca^{2+} concentration in µM s^{-1} is given by Santucci and Raghavachari (2008):

$$\frac{d[Ca^{2+}]_n}{dt} = \frac{I_{Ca,tot}/(2FV_{spine}) - \kappa_{ex}([Ca^{2+}]_n - [Ca^{2+}]_{rest})}{1 + \lambda_{buf}} \, , \tag{6.7}$$

where V_{spine} is the volume of the neuronal dendritic spine (used together with F to convert the electrical flux $I_{Ca,tot}$ (in fA) into a molar flux (in µM s^{-1})), the decay rate constant of internal Ca^{2+} concentration κ_{ex}, the resting Ca^{2+} concentration $[Ca^{2+}]_{rest}$ and the buffer capacity λ_{buf} (Santucci and Raghavachari, 2008).

We formulate the concentration of activated neuronal NO synthase $[nNOS_{act}]_n$ in µM s^{-1} as the solution of the following rate equation (Hayashi et al., 1999):

$$\frac{d[nNOS_{act}]_n}{dt} = \frac{V_{max,nNOS}[CaM]_n}{K_{m,nNOS} + [CaM]_n} - \mu_{deact,n}[nNOS_{act}]_n \, , \tag{6.8}$$

where $V_{max,nNOS}$ is the maximal rate of nNOS activity, $\mu_{deact,n}$ is the deactivation rate (Comerford et al., 2008), and $K_{m,nNOS}$ is the corresponding Michaelis constant (Hayashi et al., 1999).

The concentration of calmodulin / calcium complexes is given by Crouch and Klee (1980):

$$[CaM]_n = \frac{[Ca^{2+}]_n}{m_c} \tag{6.9}$$

with m_c, the number of Ca^{2+} ions bound per calmodulin:

$$m_c = \frac{[Ca^{2+}]_n}{\phi_{mc}} \frac{d\phi_{mc}}{d[Ca^{2+}]_n}, \tag{6.10}$$

where ϕ_{mc}, the sum of all states of bound Ca^{2+} with respect to free $[Ca^{2+}]_n$, is

$$\phi_{mc} = 1 + Q_1[Ca^{2+}]_n + Q_1Q_2[Ca^{2+}]_n^2 + Q_1Q_2Q_3[Ca^{2+}]_n^3 + Q_1Q_2Q_3Q_4[Ca^{2+}]_n^4 \tag{6.11}$$

with the binding constants Q_1 to Q_4 (Crouch and Klee, 1980).

6.2.1.2 *Endothelial Nitric Oxide Production*

NO production in the EC is catalysed by the constitutive enzyme isoform eNOS, whose catalytic activity is sensitive to the availability of the substances O_2 and L-Arg (Chen and Popel, 2006). An overview of the model detail is given in Figure 31.

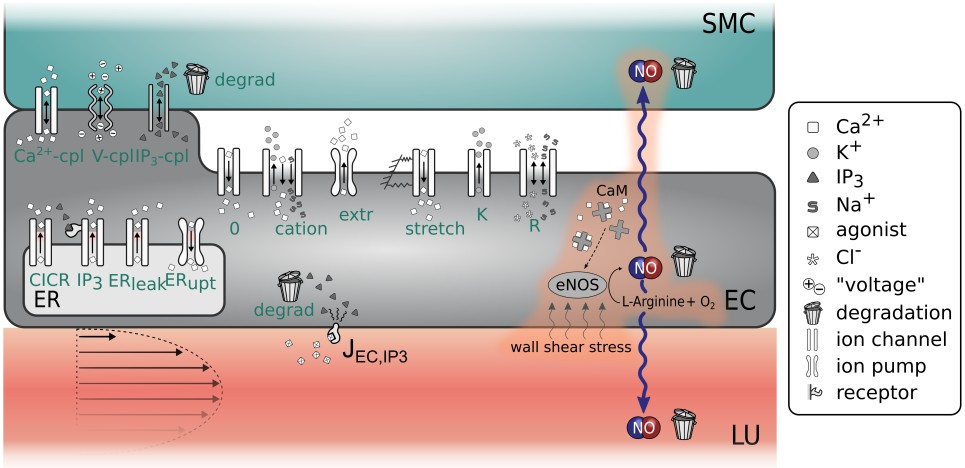

Figure 31: Graphical representation of the mathematical model, detail. The biochemical synthesis of NO in the EC is catalysed by the enzyme eNOS. It depends on the available concentration of the substances L-Arg and O_2 and is mediated by wall shear stress. The model addition to our previous foundation model (Dormanns et al., 2014) is highlighted. SMC - Smooth muscle cell, EC - endothelial cell, LU - lumen.

The endothelial NO production can be mathematically expressed as

$$p_{NO,j} = V_{max,NO,j}[eNOS_{act}]_j \frac{[O_2]_j}{K_{m,O2,j} + [O_2]_j} \frac{[L\text{-}Arg]_j}{K_{m,L\text{-}Arg,j} + [L\text{-}Arg]_j} . \quad (6.12)$$

The maximal activity of eNOS $V_{max,NO,j}$ is controlled by the intracellular calcium concentration $[Ca^{2+}]_j$ (Chen and Popel, 2006) and additionally it depends on wss, which occurs due to the blood flow through the perfusing arteriole (Comerford et al., 2008).

Fluid shear stress activates a pathway involving phosphatidylinositol 3-kinase (PI3K) and the serine/threonine-specific protein kinase enzyme, which phosphorylates eNOS (Fisslthaler et al., 2000).

Comerford et al. (2008) describe the elastic strain energy stored within the vessel membrane and quantify exogenous Ca^{2+}entry *via* shear stress-gated ion channels. The concentration of activated eNOS is given by the solution of the following differential equation (Comerford et al., 2008):

$$\frac{d[eNOS_{act}]_j}{dt} = \gamma_{eNOS} \frac{K_{dis}[Ca^{2+}]_j}{K_{m,eNOS} + [Ca^{2+}]_j} + (1 - \gamma_{eNOS}) g_{max} F_{wss} - \mu_{deact,j}[eNOS_{act}]_j . \quad (6.13)$$

The activation of eNOS by the cytosolic free calcium concentration in the EC, $[Ca^{2+}]_j$, is given by the first term of the equation, where K_{dis} describes the eNOS-caveolin disassociation rate and $K_{m,eNOS}$ is the Michaelis constant. g_{max} is the maximal wss-induced eNOS activation rate, and $\mu_{deact,j}$ denotes the deactivation rate (Comerford et al., 2008).

The function F_{wss} describing the elastic strain energy stored within the membrane is given by Wiesner et al. (1997):

$$F_{wss} = \frac{1}{1 + \alpha_{wss} \exp(-W_{wss})} - \frac{1}{1 + \alpha_{wss}} . \quad (6.14)$$

Here α_{wss} is a zero shear open channel constant (Comerford et al., 2008). Note that we have added the term $1/(1+\alpha_{wss})$ in order to deactivate the endothelial synthase of NO in the presence of no wss.

The strain energy density function W_{wss} is taken from Wiesner et al. (1997):

$$W_{wss} = W_0 \frac{(\tau_{wss} + \sqrt{16\delta_{wss}^2 + \tau_{wss}^2} - 4\delta_{wss})^2}{\tau_{wss} + \sqrt{16\delta_{wss}^2 + \tau_{wss}^2}} \tag{6.15}$$

with W_0, a shear gating constant and δ_{wss}, the membrane shear modulus (Comerford et al., 2008).

The wss, τ_{wss}, in the arteriolar wall depends on the regional cerebral blood flow (rCBF), Q. We assume Hagen-Poiseuille flow for cerebral arterioles:

$$Q = \frac{\Delta P \pi r^4}{8\eta L}\,, \tag{6.16}$$

where $\Delta P/L$ is the pressure drop over a given length of pipe (arteriole) and η is the dynamic viscosity of the fluid (blood), both assumed to be constant. The radius r of the arteriole is determined by the dynamics of the actin-myosin phosphorylation model by Hai and Murphy (1988) used in our NVU model (Dormanns et al., 2014).

The wss, i.e. the frictional force per unit area, reads as follows:

$$\tau_{wss} = \frac{4\eta Q}{\pi r^3} = \frac{r\Delta P}{2L}\,. \tag{6.17}$$

This creates a positive feedback mechanism, since increased wss will result in higher NO production from the EC, leading to vasodilation and further variation in wss.

6.2.2 *Nitric Oxide Diffusion*

The mathematical description of the NO diffusion is approached in many references (Wood and Garthwaite, 1994; Laurent et al., 1996; Lancaster, 1997). It can be derived from Fick's second law describing a general diffusion of a substance over time in space. Steady-state conditions can be assumed, because diffusivity of NO is very high (diffusion coefficient $D_{c,NO}$ = 3300 µm^2 s^{-1}, Malinski et al., 1993), whereas the consumption of NO, represented by $c_{NO,m}$ in Equation 6.1, is shown to be rather slow (Vaughn et al., 1998). Instead of using complex partial differential equations, we simplify the diffusion formulation, using the Einstein-Smoluchowski equation to describe the characteristic time $\tau_{\Delta x}$ that is needed for NO to diffuse over a certain distance, Δx_m, from the centre of one cell to another, which reads as:

$$\tau_{\Delta x,m} = \frac{(\Delta x_m)^2}{2D_{c,NO}} \,. \tag{6.18}$$

The distance between the centre of the EC layer and the centre of the SMC layer, x_{ji}, is 3.75 µm (Kavdia et al., 2002) and the distance between the centre of the NE layer and the one of the SMC layer is estimated to be 50 µm with the astrocyte in the middle between them.

For the diffusive flux of NO from one compartment into another, we assume linear diffusion, similar to Sneyd et al. (1995a,b); Bindschadler and Sneyd (2001):

$$d_{NO,m} = \frac{[NO]_{out} - [NO]_{in}}{\tau_{\Delta x,m}};\ m \in \{n, k, i, j\} \,. \tag{6.19}$$

NO diffusivity is assumed to be constant even though Vaughn et al. (1998) propose that the value of the effective diffusion coefficient $D_{c,NO}$ varies for

different regions. Furthermore, we do not consider concentration gradients within the cytosol (lumped parameter approach).

The compartment model describes the diffusion between the different domains, but does not consider the amount of NO that is released in the lumen and is scavenged by reactions with haemoglobin. Butler et al. (1998) and Kavdia and Popel (2003), who base their results on numerical simulations, find that the NO concentration in the lumen is zero after a distance of approximately half of the radius. Therefore, the diffusion flux J_{lumen}, i.e. the amount of ions leaving the EC per unit area and time, described by Fick's first law can be approximated by:

$$J_{lumen} = -D_{c,NO}\frac{\partial [NO]_j}{\partial x} \approx -D_{c,NO}\frac{\Delta [NO]_j}{\Delta x} \approx -D_{c,NO}\frac{[NO]_j}{r/2} \tag{6.20}$$

J_{lumen} is converted into a concentration leaving the region per unit time by multiplying with the arteriolar surface area and dividing by the volume. The arteriole is treated as a hollow cylinder with radius r and a given length δz. So, the diffusive flux $d_{NO,j}$ into the lumen reads as:

$$d_{NO,j} = \frac{2\pi r \delta z}{\pi r^2 \delta z}\left(-D_{c,NO}\frac{[NO]_j}{r/2}\right) \approx \frac{-4D_{c,NO}[NO]_j}{r^2} \tag{6.21}$$

6.2.3 *Nitric Oxide Consumption*

As a free radical, NO reacts readily with biochemical species containing unpaired electrons, such as molecular oxygen, superoxide anions and metals (Mayer and Hemmens, 1997). NO gets scavenged in the cytosol of all cell types through which it diffuses. Mathematically, the scavenging term for all

model compartments (except for SMC, see Equation 6.23) is given as (following Kavdia et al. (2002)):

$$c_{NO,m} = k_m [NO]_m C_m; \; m \in \{n, k, j\} \, , \tag{6.22}$$

where C_m is the concentration of reactive species in the cell type and k_m represents the reaction rate constant.

6.2.4 *Nitric Oxide in the Smooth Muscle Cell*

NO diffuses through all cell types and reaches the SMC, which forms the contractile core of the NVU model (Dormanns et al., 2014). NO, *via* its second messenger cGMP, influences the SMC contraction mechanism and the open probability of the BK channel (see Figure 32).

The time dependent rate of change of NO concentration in the SMC $[NO]_i$ is the sum of the diffusive fluxes from the NE and the EC less the amount of NO that is scavenged. This is written as:

$$\frac{d[NO]_i}{dt} = \frac{[NO]_n - [NO]_i}{\tau_{ni}} + \frac{[NO]_j - [NO]_i}{\tau_{ij}} - k_{dno}[NO]_i \, , \tag{6.23}$$

where k_{dno} denotes the lumped NO consumption rate constant that reflects the activity of various NO scavengers like sGC (Yang et al., 2005).

In the SMC NO activates soluble guanylyl cyclase (sGC), an enzyme catalysing the formation of the second messenger cGMP. The kinetics of sGC and its complexes are described by Yang et al. (2005) with reaction rate constants from Condorelli and George (2001). The sGC system with E_b, the fraction of sGC in the basal state, E_{6c}, the fraction of sGC in the intermediate form

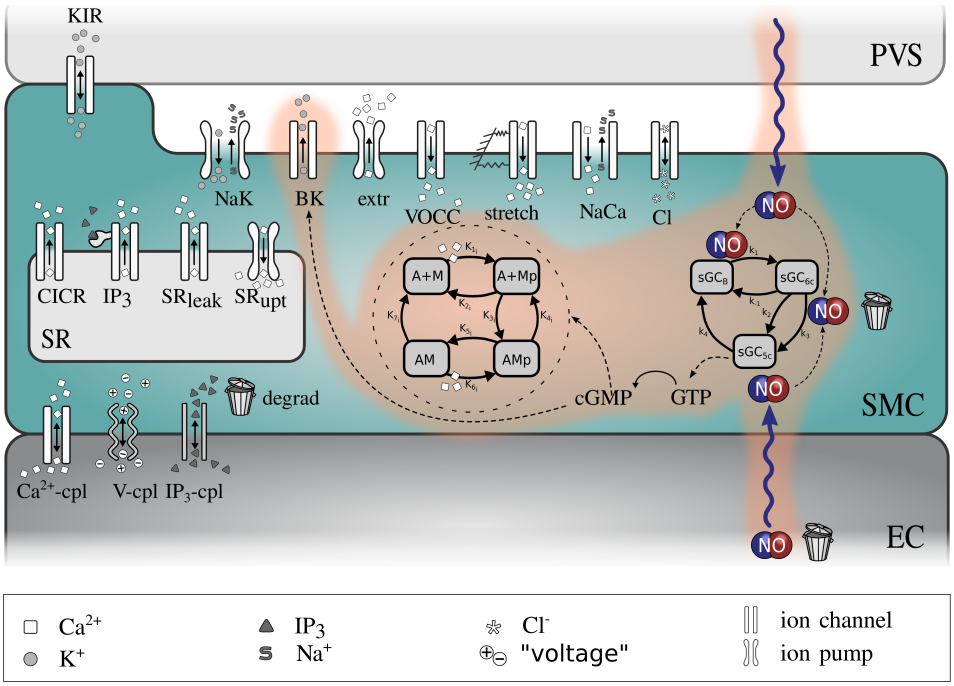

Figure 32: Graphical representation of the mathematical model, detail. NO in the smooth muscle cell (SMC) influences the contraction mechanism and the open probability of the big potassium channel (BK). The model addition to our previous foundation model (Dormanns et al., 2014) is highlighted. PVS - Perivascular space, EC - Endothelial cell.

and E_{5c}, the fraction of sGC in the fully activated form, is described by the following set of equations (Yang et al., 2005):

$$\begin{aligned}
\frac{dE_b}{dt} &= (-k_1[NO]_i - k_{-1})E_b + (k_4 - k_{-1})E_{5c} + k_{-1} \\
\frac{dE_{6c}}{dt} &= k_1 E_b [NO]_i - (k_{-1} + k_2)E_{6c} - k_3 E_{6c}[NO]_i \\
E_{5c} &= 1 - E_b - E_{6c} \,,
\end{aligned} \tag{6.24}$$

where k_{-1} to k_4 are rate constants, of which k_4 depends on the cGMP concentration:

$$k_4 = C_4[cGMP]_i^{m_4} \,. \tag{6.25}$$

Here m reflects the strength of the cGMP feedback and C_4 is a rate constant (Yang et al., 2005). The cGMP concentration is determined by

$$\frac{d[cGMP]_i}{dt} = V_{max,sGC} E_{5c} - \frac{V_{max,pde}[cGMP]_i}{K_{m,pde}[cGMP]_i} , \tag{6.26}$$

where $V_{max,sGC}$ is the maximum cGMP production rate, $V_{max,pde}$ the phosphodiesterase rate constant, and $K_{m,pde}$ the Michaelis constant (Yang et al., 2005).

6.2.5 *Nitric Oxide Mediated Dilation*

Yang et al. (2005) suggested two pathways by which NO can lead to local vasodilation of arterioles in the brain. The first pathway is by indirectly influencing the SMC contractile system that is determined by the formation of cross bridges between the actin and myosin filaments and that was first described by Hai and Murphy (Hai and Murphy, 1988). There are four possible states for the formation of myosin: free nonphosphorylated cross bridges (M), free phosphorylated cross bridges (Mp), attached phosphorylated cross bridges (AMp) and attached dephosphorylated latch bridges (AM). The second messenger of NO, cGMP changes the rate constants K_2 and K_5 for the dephosphorylation of Mp to M and AMp to AM by myosin light-chain phosphatase (MLCP) (Yang et al., 2005). In our previous fundamental NVU model (Dormanns et al., 2014) we used the rate constants based on the model of (Koenigsberger et al., 2006) where K_2, $K_5 = 0.5\,s^{-1}$. Yang et al. (2005) used the following reduced two-state model to describe the phosphorylation kinetics:

$$M \underset{k_{mlcp}}{\overset{k_{mlck}}{\rightleftharpoons}} M_p , \tag{6.27}$$

where

$$k_{mlcp} = k_{mlpc,b} + k_{mlpc,c} \frac{[cGMP]^2}{[cGMP]^2 + K_{m,mlcp}^2} \tag{6.28}$$

To adjust the reduced model to the Hai and Murphy (1988) model used by Koenigsberger et al. (2006), we scale the two factors $k_{mlpc,b}$ and $k_{mlpc,c}$ in order to achieve K_2, $K_5 = 0.5\,s^{-1}$ for no NO production.

The second pathway concerns the open probability, w_i, of the BK channel in the SMC, which is a function of the membrane potential, v_i, and is shifted to the left (in the membrane potential space) by cGMP (Stockand and Sansom, 1996).

In the NVU model (Dormanns et al., 2014) the open probability of the BK channel in the SMC is described by the equation of Koenigsberger et al. (2006):

$$\frac{dw_i}{dt} = \lambda_i \left(K_{act_i} - w_i \right) , \tag{6.29}$$

with the equilibrium state K_{act_i} given by

$$K_{act,i} = \frac{([Ca^{2+}]_i + c_{w,i})^2}{([Ca^{2+}]_i + c_{w,i})^2 + \beta_i \exp(v_{Ca3,i} - v_i / R_{K,i})} . \tag{6.30}$$

Here the constants β_i, $v_{Ca3,i}$ and $R_{K,i}$ describe the channel activation. We assume that in the v_i range of interest there is an approximately constant shift of w_i when activated by cGMP that can be modelled by making $c_{w,i}$ a function of cGMP, so that:

$$c_{w,i} = \frac{1}{\epsilon_i + \alpha_i \exp(\gamma_i [cGMP]_i)} \tag{6.31}$$

with ϵ_i, α_i and γ_i as translation factors that are chosen to give the desired shift of w_i upon cGMP stimulation as observed in experiments (Stockand and Sansom, 1996).

6.3 RESULTS

A numerical model of the NO signalling pathway in NVC is presented, which is based on our previous NVU models (Farr and David, 2011; Dormanns et al., 2014). It includes NO derived from neurons and endothelial cells, catalysed by the enzymes nNOS and eNOS, respectively.

6.3.1 *Nitric Oxide Signalling Pathway under non-Pathological Conditions*

To assess the influence of the NO signalling pathway in NVC, the model was tested using a neuronal activation (stimulation) input from 400 s to 600 s simulation time. This stimulus consisted of the neuronal K^+ release (see Dormanns et al. (2014)) and a simultaneous [Glu] increase in the SC. The stimulus was given after the model had reached steady state conditions.

Figure 33 shows the key components of the NO pathway and the resulting radius change. Neuronal NOS activation is mediated by an increased intracellular Ca^{2+} concentration and endothelial NOS is activated by Ca^{2+} and as a response to increased wss due to arteriolar blood flow (see Figure 33a)). In a non-activated state there is constant [NOS_{act}] in both cells, NE and EC, which is known to maintain basic homoeostasis (Chen and Popel, 2007). The baseline value of [$eNOS_{act}$] (0.71 µM) is approximately twice as high as that of nNOS (0.32 µM).

Steady state baseline values of [NO] vary for different cell types (see Figure 33b)). The distribution is shifted towards the NE with a basal [NO] of 0.18 µM, followed by the AC with 0.13 µM. In the SMC and EC we find only marginally different NO concentrations (0.068 µM and 0.067 µM). At 400 s stimulation starts and [NO] in all cell types increases immediately (in less

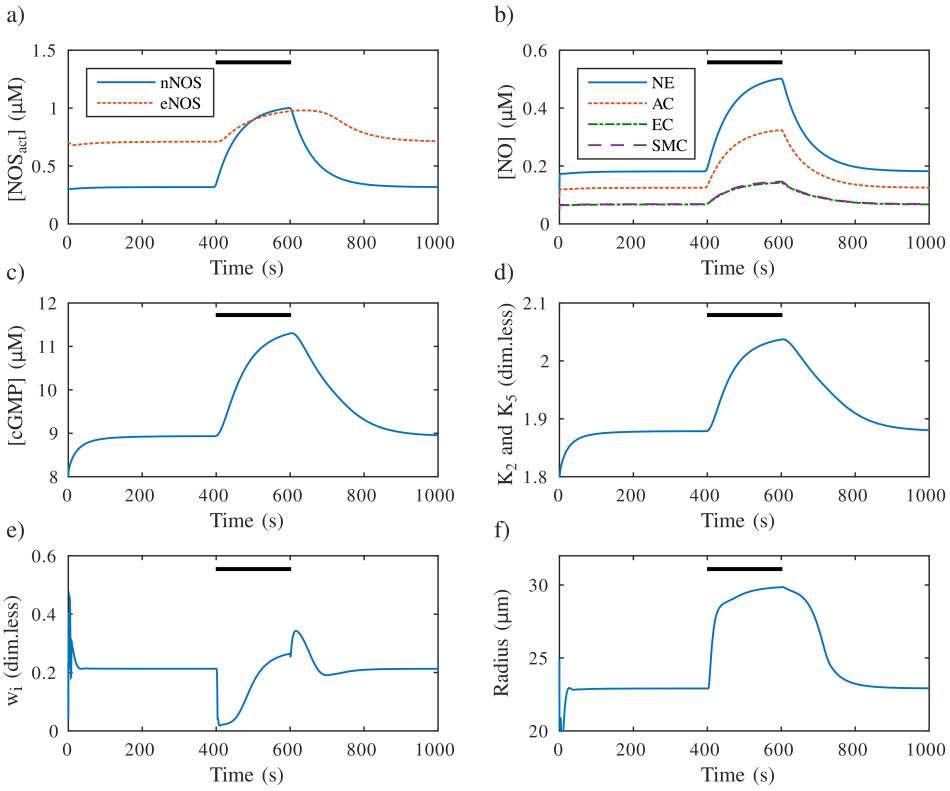

Figure 33: The nitric oxide (NO) signalling pathway in neurovascular coupling (NVC) - key components and radius change. Black bar shows the time period of stimulation (see text for description).

than 1 s). We observe that the increase is rapid at the beginning and then gradually slows down with an inverse exponential decay profile. Within the period of stimulation none of the profiles reach steady state, but they reach their maximum at 600 s when the stimulation ends. The highest [NO] obtained in the NE is 0.50 μM (2.8-fold increase), followed by 0.32 μM in the AC and 0.15 μM in both, the SMC and EC (2.1-fold increase). After the stimulation ends, all profiles show an exponential decay until they reach the initial steady state baseline value (approximately 300 s after the end of the stimulation). These profile characteristics are typical for intracellular NO dynamics and are observed upon stimulation experimentally (Laranjinha et al., 2012)

and numerically (Fadel et al., 2009), who model endothelium-derived NO release upon shear stress activation using a PDE system.

The cGMP concentration in the SMC reaches from 8.9 μM (baseline) to 11.3 μM (activated state, shown in Figure 33c)). Its profile is similar to that of [NO], but with a slower return to pre-stimulation conditions (approximately 400 s). The [cGMP] dynamics lead to changes in K_2 and K_5 of the adapted actin-myosin crossbridge model (Hai and Murphy, 1988; Yang et al., 2005; Dormanns et al., 2014). (Figure 33d) shows the non-dimensional values). In a steady state (non-stimulated) stage we obtain $K_2 = K_5 = 1.8\,s^{-1}$, which is more than three-fold the baseline value in Dormanns et al. (2014). This leads to a more dilated resting tone of the vessel and an overall shift of the radius profile. K_2 and K_5 reach a maximum value of $2.0\,s^{-1}$ at approximately 600 s.

Figure 33f) shows the perfusing vessel radius as a function of time. It has a baseline (steady state) value of 22.91 μm and a peak value during stimulation of 29.81 μm. The profile shows a rapid radius increase immediately after the start of stimulation, continuing for approximately 10-15 seconds, but the gradient then decreases until the stimulation ceases. The first 80% of dilation is achieved within 30 s and the remainder within 170 s. At the end of stimulation it has not reached steady state conditions yet and takes approximately 300 s to return to the original non-activated value.

6.3.2 *Distribution of Nitric Oxide*

Investigating the cellular distribution of NO among all cell types is of high interest, because NO diffuses rapidly from one compartment into others and therefore its physiological impact is not limited to the cell in which it is synthesised. In our model NO is produced in the NE and the EC, which are the most influential NO producers (Fleming and Busse, 1999; Forsythe

et al., 2001). We analyse the equilibrium concentration of NO obtained by diffusion and consumption in all four cell types, with special emphasis on that in the SMC, since it forms the contractile unit of the NVU.

We are interested in the resting state, when NO is produced at a basal level, and in the activated state during NVC, when we expect higher NO release from the NE. In each state, three cases are studied: The influence of NO release 1) from both, the NE and EC, 2) only from the NE and 3) only from the EC.

Figure 34a) shows the equilibrium distribution of basal NO. When both cell types, NE and EC, release NO, the equilibrium NO concentration is the highest in the NE (0.18 μM), followed by the AC (0.13 μM) and the lowest in the SMC and EC (both 0.07 μM). With NO only released from the NE, we obtain a similar gradient among the different cell types reaching from 0.14 μM in the NE to 0.03 μM in the SMC and EC. However, when only endothelial NO production is activated, the concentration in all cell types is constant (0.04 μM). The NO concentration in the SMC in a resting state is dominated by the production from the EC. Figure 34b) shows the equilibrium distribution of NO during neuronal activation. Here, the NO concentration in the NE is more than twice as high as in the resting state (Figure 34a)). In all cell types the influence of the neuronal NO production governs the total equilibrium concentration in an activated state.

6.3.3 *Contribution of Nitric Oxide towards Neurovascular Coupling*

The majority of published work in the literature states that NO plays a central role in cerebral blood flow regulation by modulating NVC. In order to further understand this, the vascular response to neuronal activity with and without the NO signalling pathway was analysed. Figure 35 shows the open

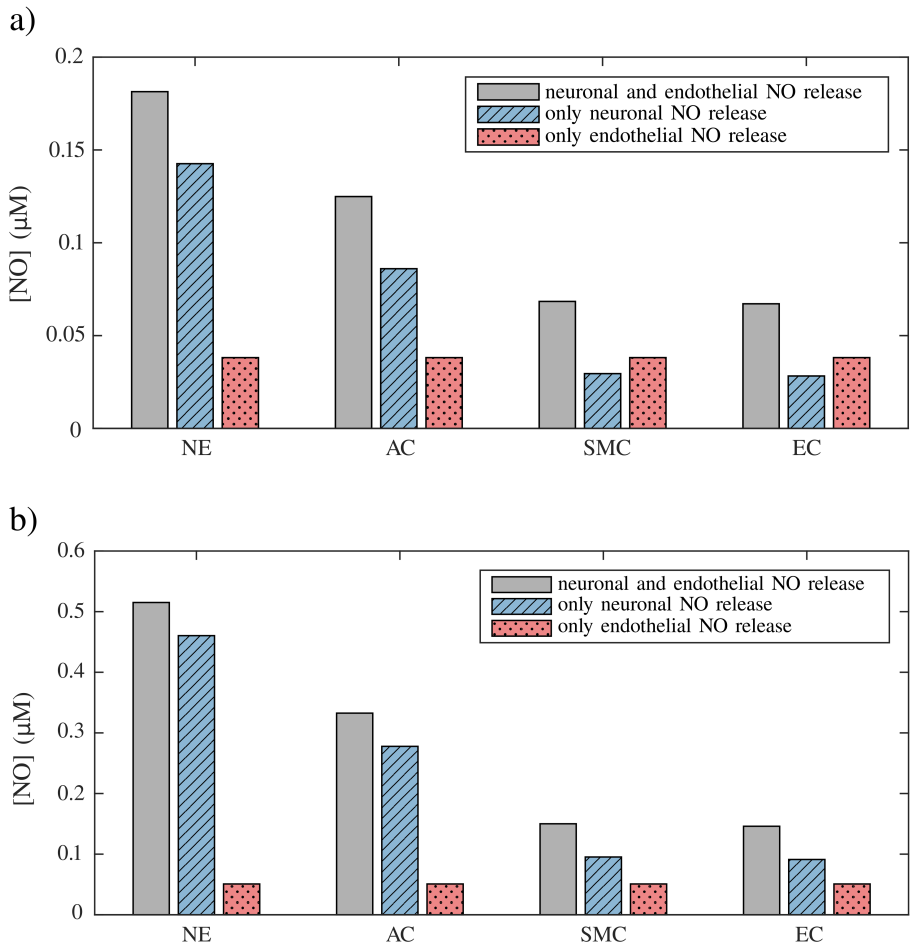

Figure 34: Steady state distribution of NO concentration among different cell types under the influence of basal NO release from NE and EC (plain, left), only from NE (hatched, middle) and only from EC (dotted, right). a) Resting state, b) Activated state.

probability of the BK channel and the arteriolar radius over time in four cases: 1) No input stimulus, 2) only neuronal K^+ as input and all NO signalling pathway related components disabled, i.e. no NO production in EC or NE, 3) only Glu stimulus with NO signalling pathway enabled, and 4) both input stimuli K^+ and Glu. In all cases the neuronal stimulation, if existent, was given from 400 s to 600 s.

With the NO pathway included the arteriolar vessel shows a more dilated resting tone (22.91 μm) compared to the NVC model without NO (19.46 μm).

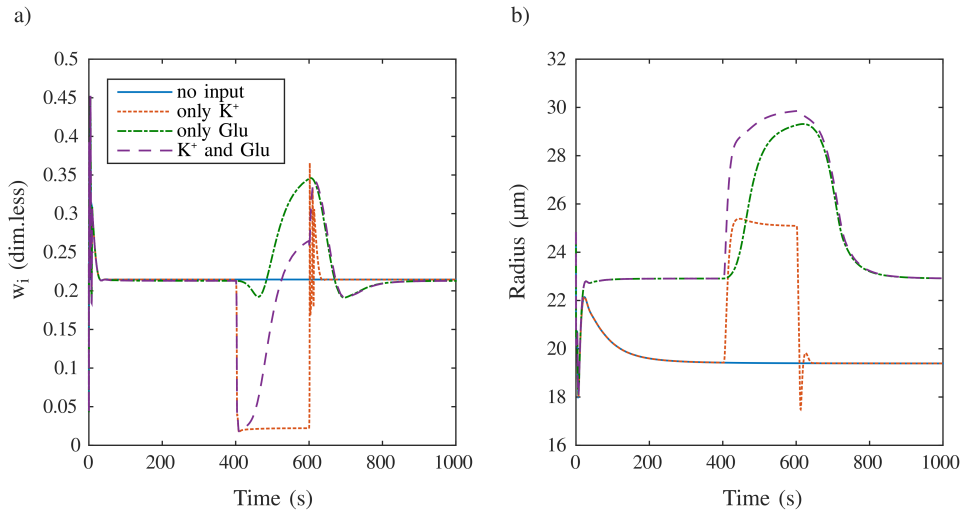

Figure 35: Open probability of the SMC BK channel (a) and arteriolar radius response (b) for four different cases of stimuli (see text for description).

During neuronal activation the vessel responds differently for the two cases. Both profiles show a rapid increase upon stimulation in the first 30 s. After this the radius of the model without NO drops slightly and reaches a plateau value of 24.8 µm, whereas the radius of the model with NO keeps constantly increasing, but at a slower rate than in the first 30 s. Within a stimulation of 200 s it reaches 29.9 µm, which is 4.7% more dilation with respect to the baseline. After stimulation ends both profiles return to the original value. Without NO we observe an undershoot of the radius, whereas with NO we obtain a smoother curve with a relatively slow return to the baseline.

6.4 DISCUSSION

Our numerical model of NVC including the NO signalling pathway is capable of simulating arteriolar responses to neuronal activation. It can show that NO acts in a vasodilatory sense and that it significantly influences key components of NVC dynamics. Furthermore, it can give a unique insight

into the effects of NO in the whole NVU, thereby revealing underlying mechanisms that are not able to be shown in experiments, or only to a limited extent.

6.4.1 *Contribution of Nitric Oxide towards Neurovascular Coupling*

The implementation of the NO signalling pathway in our NVU model (Dormanns et al., 2014) leads to major changes throughout all model components, of which the arteriolar radius is of highest interest, because it directly determines the regional cerebral blood flow (rCBF). With the NO pathway included the arteriolar vessel shows a more dilated resting tone compared to the NVC model without NO (see Figure 35, right). This shift of baseline is due to a constant supply of vasodilatory NO from both NE and EC (see Figure 34a)). The other novelty is the dilation behaviour during neuronal stimulation. The radius profile shows a larger and longer response to stimulation than without the NO pathway.

Analysing all model components we can divide the radius response into two phases:

1) During neuronal stimulation, the K^+ concentration in the PVS increases and activates the K^+ efflux through the inward-rectifying potassium (J_{KIR}) channel in the SMC (see Figure 32). As a result of this the intracellular K^+ drops. This leads to hyperpolarisation of the cell, which in turn enhances the J_{KIR} efflux further, forming a positive feedback mechanism. At the same time, the decreased membrane potential v_i leads to a decrease of the K^+ efflux through the big potassium (BK) channel ($J_{BK,i}$). This absolute amount of decrease, however, is smaller than the increase of K^+ leaving the cell through the J_{KIR} channel. Therefore, the drop in the SMC membrane potential (v_i) is maintained and leads to a closure of the VOCC channel. The Ca^{2+} influx

through this channel is decreased leading to a drop of Ca^{2+} concentration in the SMC cytosol and a relatively fast dilation of the vessel radius. After approximately 100 s the fluxes balance each other and the system reaches steady state conditions and rests at an activated, dilated state equilibrium.

2) A slower component of the model with the NO signalling pathway is the increase of cGMP in the SMC. This leads to the shift of the open probability of the BK channel. The K^+ efflux increases with the opening of the channel, which means that the intracellular K^+ concentration drops at a faster rate than before. Instead of reaching steady state conditions after around 100 s, as the model would do if the NO pathway was not included, the membrane potential drops further. As a consequence of this the VOCC channel closes further and the SMC Ca^{2+} concentration decreases. As an overall behaviour the vessel dilates further with the NO signalling pathway included in the model and returns back to the basal state more slowly.

We can conclude that the neuronal K^+ release governs the fast onset of vasodilation whilst the Glu release, *via* the NO signalling pathway, is responsible for maintaining the dilation longer and thus providing more oxygen and glucose to adjacent brain tissue with increased cerebral blood flow. The model shows the interactions between K^+ and Glu signalling and that NO plays a role as an important vasodilator, which is in agreement with experimental results that show that NOS blockade strongly attenuates the K^+-induced vasodilation and, ultimately, elevation of rCBF (Dreier et al., 1995).

The rCBF Q changes the arteriolar radius r in the following way (assuming Hagen-Poiseuille flow, see Eq 6.16):

$$\frac{dQ}{dr} = \frac{\Delta P \pi 4 r^3}{8 \eta L} \, . \tag{6.32}$$

Using Eq 6.16 and 6.32 changes in Q upon neuronal stimulation compared to the basal rCBF Q_0 can be written as:

$$\frac{dQ}{Q_0} = \frac{\Delta P \pi 4 r^3}{8\eta L} dr \left(\frac{\Delta P \pi r^4}{8\eta L} \right)^{-1} = \frac{4}{r_0} dr \,, \tag{6.33}$$

from which follows

$$\frac{dr}{r_0} = \frac{1}{4} \frac{dQ}{Q_0} \,, \tag{6.34}$$

where r_0 is the basal arteriolar radius.

Dirnagl et al. (1993) observed an increase of rCBF upon vibrissae stimulation for 60 s of $\frac{dQ}{Q_0} = 17\%$ in control rats and approximately 50% less response when the production of NO was blocked. This corresponds to a radius increase of 4.25% (with NO) and 2.13% (blocked NO production). Our foundation model without NO shows an increase of the arteriolar radius of 27.4% and the radius in our model including NO signalling responds to neuronal K^+ and Glu stimulation with a 30.5%. There may be several explanations for the discrepancy in the vessel response, e.g. anesthesia of rats, measuring method and level of neuronal activity. Hillman et al. (2007) observe rapid dilation of pial arterioles upon fore- and hind-paw stimulation of 17% to 29%, which corresponds more with our findings. Further validation of our model with experimental data combined with a parameter sensitivity analysis will be needed to improve accuracy of results.

6.4.2 *Governing Source of Nitric Oxide*

NO signalling is regulated at the level of its production. It can lead either to toxicity or to neuroprotection depending on the level of NO (Zorrilla-Zubilete et al., 2010). Our model predicts an NO concentration in different cerebral cell types from 0.03 µM in the SMC and EC to 0.18 µM in the NE

(see Figure 34a) and 34b)). This lies in the range of neuroprotective effects (Zorrilla-Zubilete et al., 2010), but physiological measurements in literature show conflicting results regarding NO concentration in the brain. Basal NO levels reach from <0.01 µM (Malinski et al., 1993) to as high as 1.6 µM (Buerk, 2001). Our model shows the distribution of equilibrium NO among different cell types (see Figure 34a) and 34b)). A high amount of NO being scavenged by the reactions with arteriolar haemoglobin explains the reduction of NO concentration the closer the cell types are located to the lumen. This can be described as a luminal "sink". Our diffusion model is very approximate, however the result are in the same order of magnitude as those from models with spatially varying solutions (Kavdia and Popel, 2003).

A considerable amount of experimental research has been focussed on determining the most important source of NO contributing to cerebrovascular regulation. NO is involved in the maintenance of resting cerebral blood flow as well as in the control of the vascular response to neuronal activation. However, it is still a matter of debate which cell type contributes most in each physiological phenomenon (Butler and Nicholsson, 2003; Lourenco et al., 2014; Tabatabaei and Girouard, 2014). Fleming and Busse (1999) emphasise that NO derived from the endothelium is the primary relaxing factor in the regulation of vascular tone and homeostasis. Nevertheless, eNOS is not believed to be the only regulator of vascular perfusion. Simultaneous measurements of NO dynamics and cerebral blood flow changes in hippocampus *in vivo* by Lourenco et al. (2014) support the hypothesis that NVC is mediated by nNOS-derived NO. It is believed that, despite the fact that nNOS is the major form of NOS in arterioles (Chen and Popel, 2006), both nNOS and eNOS are involved in NVC. Depending on the level of stimulation, eNOS plays a prominent role at low intensity stimulation, while nNOS is more involved at high intensity stimulation (Tabatabaei and Girouard, 2014).

Generally, the NO in the SMC comprises NO that was produced by nNOS in the NE and by eNOS in the EC. Our model shows that in a resting state the main source of vasodilating NO that diffuses to the contractile unit of the NVU, the SMC, is eNOS (see Figure 34a)). However, during glutamatergic neuronal stimulation nNOS plays the more prominent role in providing NO and the SMC NO concentration is dominated by the NE component (see Figure 34b)).

6.5 CONCLUSION

Nitric oxide (NO) is a neurotransmitter known to act as a potent cerebral vasodilator. Its role in neurovascular coupling (NVC) is discussed controversially and one of the main unanswered questions is which cell type provides the governing source of NO for the regulation of vasodynamics.

Mathematical modelling can be an appropriate tool to investigate the contribution of NO towards the key components of NVC and analyse underlying mechanisms. The lumped parameter model of a neurovascular unit, including neurons (NE), astrocytes (AC), smooth muscle cells (SMC) and endothelial cells (EC), was extended to model the NO signalling pathway.

Results show that NO leads to a general shift of the resting regional blood flow by dilating the arteriolar radius. Furthermore, dilation during neuronal activation is enhanced. Simulations show that potassium release is responsible for the fast onset of vascular response, whereas NO-modulated mechanisms maintain dilation. Wall shear stress-activated NO release from the EC leads to a delayed return to the basal state of the arteriolar radius. The governing source of vasodilating NO that diffuses into the SMC, which determine the arteriolar radius, depends on neuronal activation. In the rest-

ing state the EC provides the major contribution towards vasorelaxation, whereas during neuronal stimulation NO produced by the NE dominates.

7

VASCULAR TREE MODEL

7.1 INTRODUCTION

The network of blood vessels responsible for supplying the brain has two primary purposes, to deliver the required O_2 and nutrients to the tissue, and to convectively remove metabolic waste products such as CO_2. It has to dynamically match the supply to the varying metabolic demand of localised neuronal activity. This is achieved by NVC, the local vessel dilation and constriction due to changes in neuronal activity. The vessel diameter controls the local cerebral bloodflow and thereby the supply of O_2 and nutrients.

Nutrient exchange primarily occurs in the capillaries, the fine mesh-like network of blood vessels embedded in the tissue, where species such as O_2, CO_2 and Glu are able to diffuse through the capillary walls.

The principal physical mechanism that controls bloodflow through the capillary network is the active dilation and contraction of the small arterioles that feed the tissue. Vessel dilation reduces the resistance to bloodflow, and hence increases the flow, while contraction restricts the blood supply. The vasocontraction and -dilation is due to the layers of SMCs surrounding the arteriole, which have the ability to actively contract or relax through actin-myosin crossbridge formation and cycling. The primary biochemical agent responsible for regulating this process is Ca^{2+} in the cytosol of the SMC. As highlighted in previous chapters, stimuli that have chemical pathways ulti-

mately affecting cytosolic Ca^{2+} are manifold, including shear stress at the arterial wall (Wiesner et al., 1997; see chapter 6), transmural pressure in the vessel (Gonzalez-Fernandez and Ermentrout, 1994), tissue pH, and neuronal activity through Glu and K^+ release in the SC (Attwell et al., 2010; see chapter 4).

The cerebral cortex is fed with blood and nutrients from the outside inwards, starting at the pia mater (pial arteries) and bifurcating into the cortex with penetrating arteries which eventually perfuse the capillary bed. Thus it is essentially a tree of blood vessels, which repeatedly bifurcates from a large root vessel into vessels of shorter length and smaller radius. A cerebral vascular tree may comprise up to 20 or more bifurcation levels, corresponding to many millions of vessels in the tree.

The dimensions of the vessels scale in such a way as to leave a significant fraction of the overall pressure drop from the root of the tree to the capillary bed across the smallest arterioles near the leaves of the tree (Fung, 1993). Variation in the resistance of these vessels can hence modify bloodflow in a highly localised manner, and collective variation can significantly modify the overall cerebral perfusion.

Because of the connectivity of the tree, a change in resistance of one blood vessel can cause a change in pressure, and hence flow, throughout the binary tree. For example, if the resistance of blood vessels in a particular region decreases, then bloodflow will effectively be diverted through those vessels from other parts of the tree. The remainder of the tree will need, to some extent, to compensate for this decrease in flow. The effect that this connectedness will have on cerebral perfusion is not immediately apparent. One means of studying this problem is through large-scale simulation, whereby arteriole-level models of NVC, achieved by the collection of linked NVU cells, incorporating the desired biochemical processes are inserted into a spatially-

embedded vascular tree, and simulations are conducted at a macroscopic-scale.

The communication between cerebral tissue and vasculature exhibits a bidirectional character. Not only does neuronal activity modulate the vessel diameter *via* the previously described signalling pathways, but the NVU can also receive information from the vessel lumen. Spatially varying luminal agonists, such as ATP, can act on endothelial receptors and provide a flux of IP_3 into the EC cytosol. IP_3 diffuses through GJ between ECs and SMCs and can change their dynamical state (see chapter 5).

Additionally, ECs and SMCs are able to detect and respond to radial changes through stretch-activated channels (Koenigsberger et al., 2006). These channels provide a flux of Ca^{2+} into the EC, which again through GJ transfers Ca^{2+} to the SMC increasing vasoconstriction *via* the myocin-actin pathway (Hai and Murphy, 1988). The stretch channel flux equation is a function of a number of variables, notably the membrane potential, v, and the vessel radius, r, and is given as

$$J_{stretch} = \frac{G_{stretch}}{1 + \exp\left(-\alpha_{stretch}\left(\frac{\Delta p r}{h} - \sigma_0\right)\right)}\,(v - E_{SAC}) \ . \tag{7.1}$$

Here p is the pressure in the vessel (mean value of the pressure in the two nodes connected by the vessel), $G_{stretch}$ the channel conductance, h the vessel wall thickness, E_{SAC} the Nernst potential, $\alpha_{stretch}$ a model parameter and σ_0 the circumferential stress associated with an equilibrium state of the vascular tone of the vessel (Koenigsberger et al., 2006). Hence, the stretch-activated channels provide an essential link between the NVU and the vascular tree.

Up to now *in vitro*, *in vivo* and *in silico* experiments have either investigated time-dependent flow through either simple or complex vasculatures or

looked at cell functioning *independent* of the consideration of how blood flow itself is affecting the neural phenomena and vice versa.

To investigate the effect of complex cellular models embedded in a vascular tree we allow a single NVU to be connected to each of the leaves of a tree which models in some topological sense a small section of cortical tissue/vasculature. Thus an individual NVU perfuses a small section of tissue. The activity of each NVU may be varied according to its position in the tissue block. By introducing a model of a spatially embedded dynamic vascular tree regulated by a time-dependent and spatially varying cellular scale model of NVC we can begin to examine some of the effects introduced by the connectivity of the structure of the tree and the dynamics of the cellular function. In addition, the coupling induced by the vascular tree presents numerical challenges to not only the numerical solution of the resulting ODE or PDE systems, but also because of the possible size of the system to the parallel implementation itself. In chapter 5 it was shown that for certain concentrations of agonist in both the flowing blood and tissue, the EC/SMC system exhibits domains of oscillation and induces oscillation in the arteriolar radii of the vascular tree (vasomotion). In addition, the frequency changes as a function of agonist concentration. The model is therefore able to investigate the relationship between oscillatory states of the EC/SMC and the resulting motion of the vasculature.

7.2 METHODS

In this section first the basic structure of the vascular tree, which allows for a space filling simulation, is described. The root of the tree can be considered as either a pial artery and a subsequent penetrating arterial structure into

the cerebral cortex or the start of the penetrating structure itself. Having determined the basis of the tree the NVU is briefly described, but the details can be found in Chapter 4 and the Appendix. Finally, a description is given which links the two models together forming a multi-scale model and an algorithm, which determines the numerical solution method in a parallel environment.

7.2.1 *Vascular Tree Model*

The vascular network considered in this work is a tree-like structure of blood vessels modelling a portion of the cerebral vasculature branched off from the pial or penetrating arteries (see subsection 1.1.3). The blood vessels branch into successively shorter and narrower vessels until they reach the fine mesh structure of the capillary bed. The final vessels in the tree are referred to as the terminal arterioles, and have a typical radius of 10 µm (Bell and Zlokovic, 2009).

The Reynolds and Womersley numbers for the flow in the small blood vessels in the model are very small, so we can readily assume Hagen-Poiseuille flow: for a vessel of length L and radius R, we have

$$Q = \frac{\pi R^4}{8\mu L}\Delta P \ , \tag{7.2}$$

where Q is the blood flow, μ is the blood viscosity and ΔP is the pressure drop over the vessel. We fix characteristic length and pressure values R_0, L_0, and P_0, and setting $R = R_0 r$, $\Delta P = P_0 w$ and $L = L_0 l$, equation (7.2) becomes

$$Q = \frac{\pi R_0^4 P_0}{8\mu L_0}\frac{r^4}{l} w = Q_0 g w = Q_0 q \ , \tag{7.3}$$

where $g = r^4/l$ is the (non-dimensional) conductance of the vessel. The equation $q = gw$ is analogous to Ohm's Law for an electrical circuit, with flow q taking the role of current, w as potential difference, and g as conductance (reciprocal of resistance). Note that the conductance is highly sensitive to the radius of the vessel. Because most of the systemic pressure drop occurs over the small arterioles, we assume a constant capillary bed pressure p_{cap}, and a (possibly) time-dependent pressure $p_0(t)$ at the root of the tree (see Figure 36). We consider a network of n blood vessels arranged in a symmetric binary tree with m internal nodes. The branches and nodes are ordered breadth-first, i.e. the neighbour branches and nodes are labelled first, before moving to the next level in the tree.

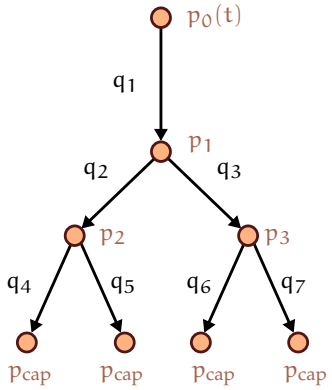

Figure 36: Indexing scheme for a binary tree. The branches and nodes are ordered breadth-first. The terminating arterioles have their pressure fixed at p_{cap}.

7.2.1.1 *Spatially Embedded Vascular Tree*

As a crude approximation of a tree with physiologically realistic morphology, we model the tree as a symmetric binary tree, with a 2D H-tree spatial structure. At each bifurcation, the radius of the daughter vessels is a factor $\alpha = \sqrt{2}$ of the radius of the parent, and the length is divided by 2 every second bifurcation. These scalings are again within the biologically realistic

limits described in the asymetric binary tree algorithm of Ottesen and Olufsen (2004). The smallest vessels are defined to have radius 10 µm and length 200 µm, and the scale of the model is therefore determined by the number of levels in the tree. A tree of 5 levels, perfusing an approximately 1.6 × 1.6 mm × 0.4 mm slice of tissue, is depicted in Figure 37.

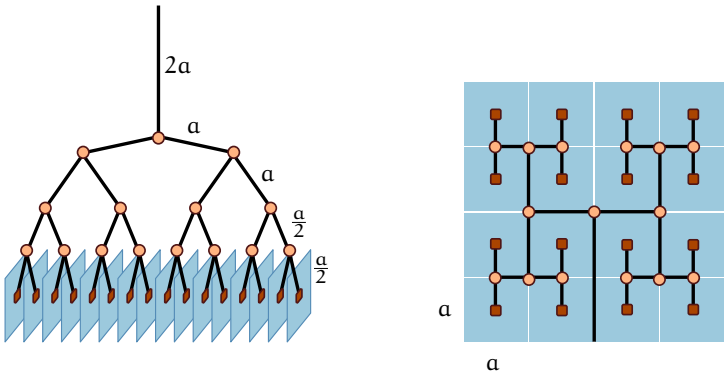

Figure 37: Spatial arrangement of a 5-level H-tree model. The tree is laid out in such a way that the terminal arterioles form a regular 2-dimensional grid in space. Each of the terminal arterioles is considered to perfuse one block of tissue.

Finally, we assume that when unpressurised, each vessel has wall thickness h^* proportional to its radius R^*, namely

$$h^* = h_{RR} R^* \,. \tag{7.4}$$

The result is a tree with a somewhat realistic morphology, but with a space-filling property that enables the coupling of 2D or 3D spatial phenomena such as the localised neural activity to the inherently 1D (or 0D) problem of blood flow in the vascular tree.

7.2.2 *Parallel Implementation*

The parallel implementation follows the work of Brown and David (2013). Because of the global coupling induced by the resistive network, the resulting stiff system of ODEs has a dense Jacobian which precludes the direct application of traditional implicit methods for numerically solving the differential equations. We consider a technique for remedying this problem by taking a block diagonal Jacobian approximation which allows use of an implicit method but retains the desirable property of explicit solvers of linear solution time scaling with problem size. Additionally, the method is amenable to significant parallelisation, and we present scaling results. A mathematical description of the problem is as follows. We model the network by a directed graph with m internal nodes and n edges. The graph is represented by an incidence matrix $A \in \mathbb{R}^{m\times n}$ with entries a_{ij} given by: a_{ij} = -1 if edge j enters node i, a_{ij} = 1 if edge j exits node i, and a_{ij} = 0 otherwise. For example, for the tree depicted in Figure 36 we obtain

$$A = \begin{bmatrix} -1 & 1 & 1 & 0 & 0 & 0 & 0 \\ 0 & -1 & 0 & 1 & 1 & 0 & 0 \\ 0 & 0 & -1 & 0 & 0 & 1 & 1 \end{bmatrix} . \tag{7.5}$$

With imposed potential or flow boundary conditions, the potential differences $\boldsymbol{w}$ across the edges are given by an expression of the form

$$\boldsymbol{w} = \begin{bmatrix} p_0 - p_1 \\ p_1 - p_2 \\ \vdots \\ p_4 - p_{cap} \end{bmatrix} = A^T \mathbf{p} + \mathbf{b} , \tag{7.6}$$

where $\mathbf{p} \in \mathbb{R}^m$ is the vector of potentials at each internal node, and $\mathbf{b} \in \mathbb{R}^n$ incorporates the boundary conditions:

$$\mathbf{b} = \begin{bmatrix} p_0(t) & 0 & 0 & -p_{cap} & -p_{cap} & -p_{cap} & -p_{cap} \end{bmatrix}^T . \tag{7.7}$$

We assume that the constitutive relation on each edge is Ohm's law: the flow through edge j is $q_j = g_j w_j$ where g_j is the conductance of the edge. In matrix form,

$$\mathbf{q} = G\boldsymbol{w} \in \mathbb{R}^n , \tag{7.8}$$

where G = diag $\mathbf{g}$.

Flow conservation requires

$$\begin{cases} \text{node 1: } -q_1 + q_2 + q_3 = 0 \\ \text{node 2: } -q2 + q_4 + q_5 = 0 \\ \text{node 3: } -q_3 + q_6 + q_7 = 0 \end{cases} \quad ; \quad \Rightarrow A\mathbf{q} = 0 , \tag{7.9}$$

and thus the vector of potentials $\mathbf{p} \in \mathbb{R}^m$ is given by solving the positive definite linear system

$$AGA^T\mathbf{p} = -AG\mathbf{b} . \tag{7.10}$$

The class of models we consider takes such a network and couples it to a system of ordinary differential equations (ODEs)

$$\dot{\mathbf{x}} = \mathbf{f}(\mathbf{x}, \mathbf{p}, t), \qquad \mathbf{x} \in \mathbb{R}^l, l \in \mathbb{N} , \tag{7.11}$$

where the vector $\mathbf{x}$ corresponds to the set of state variables of the ODE system. The differential equations for the state variables depend on the potentials in the network, and the conductances in the network are algebraically dependent on the state variables, $\mathbf{g} = \mathbf{g}(\mathbf{x})$ (the conductances can be com-

puted from the radii of the terminal arterioles). Further, the boundary conditions may be time-varying, $\mathbf{b} = \mathbf{b}(t)$. Equations (7.10) and (7.11) thus define a semi-explicit index-1 differential algebraic system of equations. The system can naively be solved by standard ODE methods by transforming it into an ODE system:

$$\frac{d\mathbf{x}}{dt} = \mathbf{f}(\mathbf{x}, (AG(\mathbf{x})A^T)^{-1}AG(\mathbf{x})\mathbf{b}(t), t) \tag{7.12}$$

The linear system (7.10) is positive definite, typically highly sparse, and depending on its structure can be efficiently solved by the conjugate gradient method or direct sparse Cholesky factorisation. Hence, function evaluations for this ODE system are relatively cheap. However, the system is stiff, requiring the evaluation of the Jacobian of the system. The Jacobian of (7.12) can be decomposed into the following form:

$$J = \frac{\partial \mathbf{f}}{\partial \mathbf{x}} + \frac{\partial \mathbf{f}}{\partial \mathbf{p}} \frac{\partial \mathbf{p}}{\partial \mathbf{g}} \frac{\partial \mathbf{g}}{\partial \mathbf{x}} \,. \tag{7.13}$$

For a typical problem the terms $\frac{\partial \mathbf{f}}{\partial \mathbf{x}}, \frac{\partial \mathbf{f}}{\partial \mathbf{p}}, \frac{\partial \mathbf{g}}{\partial \mathbf{x}}$ are likely to be highly sparse, because f and x span all of the tissue blocks and components, e.g. $\frac{\partial f_i}{\partial x_j}$ in these matrices are only non-zero if i, j correspond to equations / variables within the same tissue block. The term $\frac{\partial \mathbf{p}}{\partial \mathbf{g}}$ is given by

$$\frac{\partial \mathbf{p}}{\partial \mathbf{g}} = -(A \operatorname{diag}(\mathbf{g}(\mathbf{x})A^T)^{-1} A \operatorname{diag}(A^T\mathbf{p} + \mathbf{b}) \,, \tag{7.14}$$

which is a dense matrix, since it contains the inverse of a sparse matrix $A \operatorname{diag}(\mathbf{g})A^T$ and that matrix cannot be permuted into block triangular form. The system Jacobian, J, is thus also dense, precluding its direct evaluation for a large-scale problem. For large-scale problems it is not feasible to construct the full Jacobian of the system to use in a direct linear solver. For example, the autoregulation problem for a vasculature involving approxim-

ately 10,000,000 vessels would require more than 20TB of RAM to store the Jacobian. We choose the approximation to have block diagonal structure, so that the factorisation and solution can be decomposed into as many independent tasks as there are blocks, and hence the decomposition yields a natural parallelisation of the problem. Details of this procedure can be found in Brown and David (2013).

7.2.2.1 *Parallel Considerations*

When this algorithm is implemented on a parallel system, the H-tree network is partioned at a coarser scale, one subnetwork per computational node. Each of these coarse partitions is formed from the union of a number of fine partitions. Each coarse partition has its own incidence matrix $A^{(i)}$ with its own set of boundary values $\mathbf{b}^{(i)}$ corresponding to where it meets the problem boundary and other subnetworks. Before the approximate Jacobian can be evaluated, a global computation of pressures throughout the network is completed.

7.2.2.2 *Large-Scale Simulation of the Neurovascular Coupling Model*

We now consider applying the methodology to our previously described autoregulation model. The tissue blocks and terminal arterioles are of fixed size, so the overall problem size is dictated by the number of levels, L, in the binary tree.

To parallelise the problem, the tissue domain is split into N subdomains, where $N = 2^{L_0}, L_0 \in \mathbb{N}$, where L_0 is the number of levels in the root subtree such that each of the subdomains corresponds to an equally sized subtree with incidence matrix $A^{(i)}$. The root subtree of the network connecting each of these subtrees has incidence matrix $A^{(0)}$. The subtrees are binary trees of $L - L_0$ levels each. For each subtree in the coarse partition we specify

the fine partitioning for the Jacobian approximation by further decomposing each subtree into its own root tree with subtrees of N_S levels. The imposed boundary nodes are the nodes where the fine subtrees interface with the root. The degree of sparsity of the Jacobian can be controlled by specifying the number of levels in the tree, N_S, each subtree spans. The two decompositions are illustrated in Figure 38.

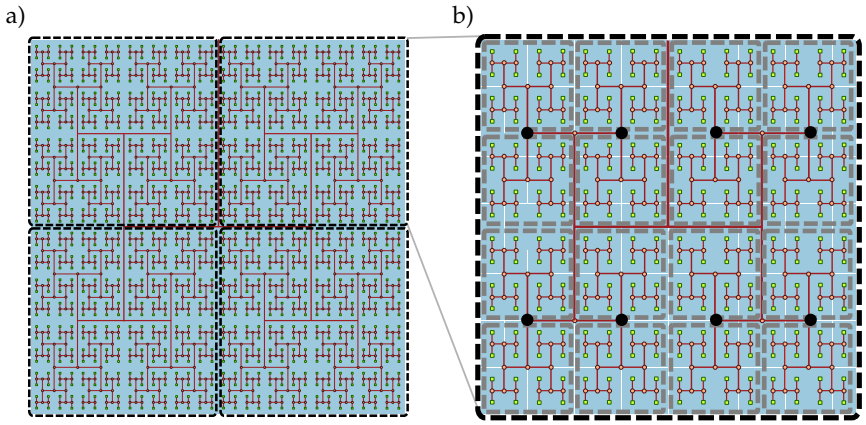

Figure 38: Example of an H-tree model of the vasculature showing fine and coarse decomposition. a) depicts a 12 $\times$ 12 $\times$ 0.4 mm tissue slice. Each subdomain of the coarse partition is mapped to one processor, whereas the fine partitioning of each subdomain (b) sets the Jacobian block size. For this example N_S = 5, so there are 16 tissue blocks and hence 16 $\times$ 24 state variables per fine partition, the Jacobian block size is 384 $\times$ 384. A tree of L levels has an $m \times n$ incidence with L = 11 into N = 4 four subtrees (L_0 = 2). The root subtree is shown in grey. b) Fine partitioning of subtree with N_S = 5 for Jacobian approximation. The network is split at the nodes (marked as black circles), resulting in Jacobian blocks for the state variables in each grey rectangle.

7.2.3 *Numerical Solution Method*

Numerical experiments were conducted to assess the convergence and scalability of the approach for the cerebral vasculature problem in the UC HPC IBM Power 755 cluster and the HP DL560 generation 9 server. The test system used is up to 32 processors in HP DL560, and 128 processors in the

Power 755 cluster, which corresponds to 4 nodes. Intranodal communication is conducted using shared memory, while internodal communication utilises an infiniband network.

To solve the ODE system, a fixed-step backward Euler method was used to solve the radial change of the leaf of the H-tree using the NVC model described in Chapter 4. The Jacobian was computed from the initial state, and then updated subsequent to any iteration that took more than 8 iterations to converge. Newton's method was said to converge when either the function value or relative error dropped below a tolerance of $\epsilon = 10^{-6}$. The matrices $\partial \mathbf{f}^{(i)}/\partial \mathbf{p}^{(i)}$ and $\partial \mathbf{f}^{(i)}/\partial \mathbf{x}^{(i)}$ were computed numerically by finite differences, using the algorithm of Curtis et al. (1974). The equations were all scaled to have steady state values near 1. The matrix $\partial \mathbf{g}^{(i)}/\partial \mathbf{p}^{(i)}$ was computed analytically. The algorithm was implemented in C with MPI, compiled using IBM's XLC (Power 755) and the GNU compiler GCC (HP DL560), and utilised CSparse (Davis, 2006) for the sparse matrix operations (sparse Cholesky factorisation, sparse LU decomposition, and matrix multiplication). The code was executed on a number of cores ranging from 1 to 32 and 128, respectively.

7.2.4 *Diffusion*

The vascular tree with the space-filling property coupled with tissue blocks allows us to study spatial phenomena such as diffusion in the tissue, which was not possible in the single NVU models.

Physiologically, the extracellular space (ECS) provides a space for multiple species to diffuse between cerebral cells. Here, hindrance by the structure of the narrow confines of the ECS compared to a free medium, expressed as tortuosity, has to be considered (Syková and Nicholson, 2008). Diffusion can

also occur between cells through ion channels and homo- and heterocellular GJs such as exhibited in SMCs and ECs. Furthermore, some molecules, such as NO, are small enough to diffuse freely through cell membranes.

For diffusion of a species, ϕ, between two adjacent tissue blocks we assume linear diffusion:

$$d = \frac{[\phi]_i - [\phi]_{i+1}}{\tau_\phi} \, . \tag{7.15}$$

Here, τ_ϕ is the characteristic time that is needed for ϕ to diffuse over the distance, Δx_{tb}, from one tissue block centre to the next. It is defined by the Einstein-Smoluchowski equation:

$$\tau_\phi = \frac{(\Delta x_{tb})^2}{2D_\phi} \, . \tag{7.16}$$

D_ϕ is the effective diffusion coefficient of ϕ in the medium and is determined by

$$D_\phi = \frac{D_{free}}{\lambda_0^2} \, , \tag{7.17}$$

where D_{free} is the free diffusion coefficient of ϕ and λ_0 is a non-dimensional tortuosity factor. For intracellular diffusion a value of 3.2 has been reported and for extracellular diffusion λ_0 =1.6 (Syková and Nicholson, 2008).

Diffusion between tissue blocks and across message passing interface (MPI) domain boundaries was implemented using so-called 'ghost blocks' at the edge of each MPI domain. In these ghost blocks variable values are stored after each iteration of the solver. Then information is exchanged with the adjacent MPI domain using the MPI routine `MPI_Sendrecv()`.

7.3 RESULTS

7.3.1 *Numerical Scaling Experiments*

Two numerical experiments were performed in order to determine the scaling effects of the parallel code, the results of which are depicted in Figure 39. The first experiment measured the strong scaling performance of the problem for a fixed problem size of L = 10 levels, with subtree size $N_S = 3$. The number of processors was varied in powers of 2 between 1 and 32 and the simulation wall clock time recorded. Figure 39a) shows that up to this number of processors, the method scales ideally. Scaling is initially superlinear, because as more processors are added, more of the problem is able to fit in fast cache memory. The second experiment measured the weak scaling

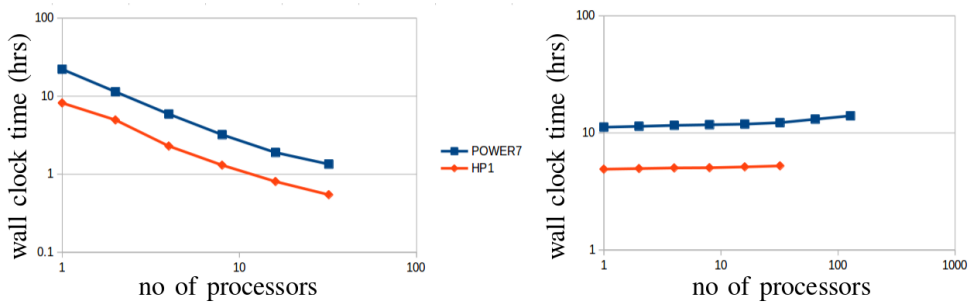

Figure 39: a) Strong scaling (L = 10, N = 1,...,32; $N_S = 3$). b) Weak scaling (L = 9, ...,16; N = 1,...,64; $N_S = 3$).

performance of the problem, whereby the problem size is increased in proportion with the number of processors. The problem size was varied between L = 9 and L = 14, with the number of processors varying between N = 1 and N = 32. Figure 39b) shows that the elapsed computational time increases slightly as the problem and computing size increase. Small problem sizes were chosen to accentuate the relative contribution of communication, and increasing the problem scale would flatten the curve further.

7.3.2 *Multi-Scale Simulations*

The presented simulations concentrate on the resulting linkage between the vasculature and the NVU embedded in a tissue block. The results are divided into three sections where the simulations provide the system when there is only i) neuronal activation only (varying spatially with the tissue block), ii) agonist activation only and iii) where is both agonist and neuronal activation.

Figure 40 shows a 64 $\times$ 64 tissue block slice containing 4096 individual blocks. The case shown simulates a Gaußian distribution of agonist in the centre of the slice, inducing oscillation in each of the tissue blocks out to a defined radius. The colour map of the blocks depicts Ca^{2+} whilst the colour of the vascular segments depicts the (scaled) bloodflow through the vessels. It is normalised for each level by a factor of $2^{(L-1)}$ to be able to compare the bloodflow of different levels in the tree.

7.3.2.1 *Neuronal Activiation Only*

Figure 41 shows the tissue block of size 8 $\times$ 8 where the neuron is activated in the area, denoted by the 3 $\times$ 3 sub-block whose border is defined by cells numbered 60 (outside) and 61 (inside). The neuronal activation starts at t = 100 seconds. The colour map on the vessel segments denotes blood flow whilst the colour mapped onto the tissue blocks denotes cytosolic SMC Ca^{2+}. The sizes of the radial segments indicate the actual radius of the vessel segment. For this particular part of the time-dependent behaviour the radius inside the activated area shows a constant and dilated set of arterial segments. As a response, vessels in the activated area dilate and due to flow conservation adjacent vessels outside get constricted. If both leaf vessels lay in the activated area their dilation is smaller than if in different areas. NVU tis-

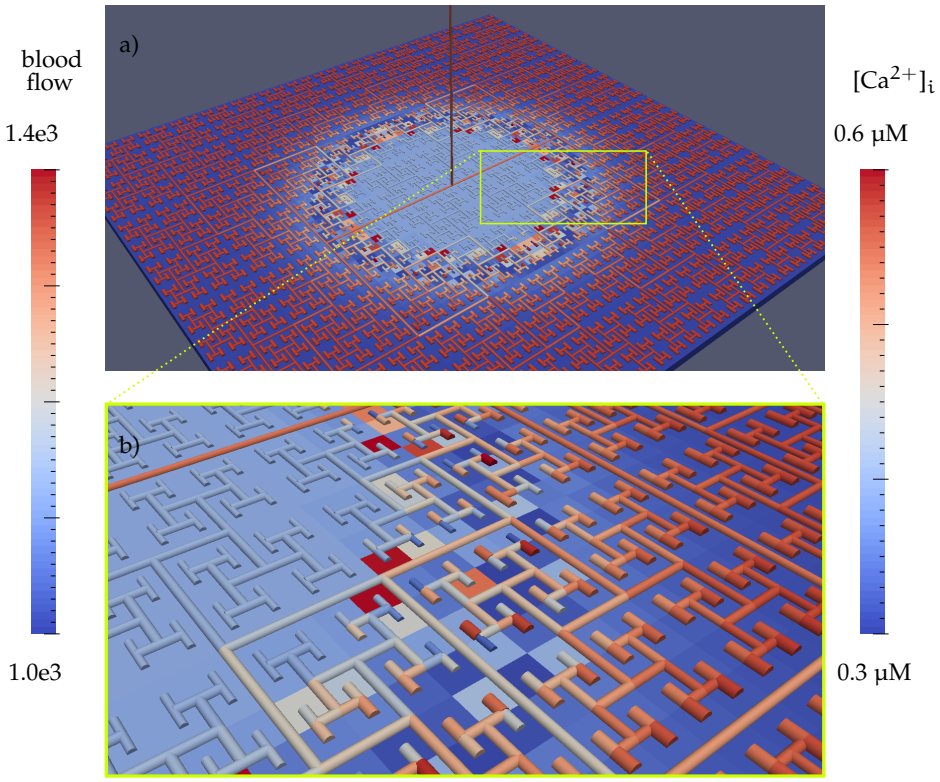

Figure 40: Simulation of a 25.6 × 25.6 mm cerebral tissue slice including 4096 NVU blocks globally coupled with a space-filling vascular tree. A two-dimensional Gaußian input function is used to activate the centre of the tissue blocks with an increased luminal agonist flux (0.18 to 0.4 µM s^{-1}). a) Overview; b) detail.

sue blocks and vasculature are bidirectionally coupled. The feedback from the radius to the NVU via the stretch-activated channels leads to a (small) change in Ca^{2+} also for the tissue blocks in the non-activated area.

Figure 42 shows the time dependent profiles for both Ca^{2+} and radius for cells 60 and 61. At the start of the activation the radius of cell 61 (inside the activated area) shows a constriction and then a dilation to accommodate the increase in neuronal activity and hence oxygen consumption. The Ca^{2+} for cell 61 shows an initial increase in value but then decreases to a constant value. This is due to the increase in K^+ in the PVS and subsequent hyperpol-

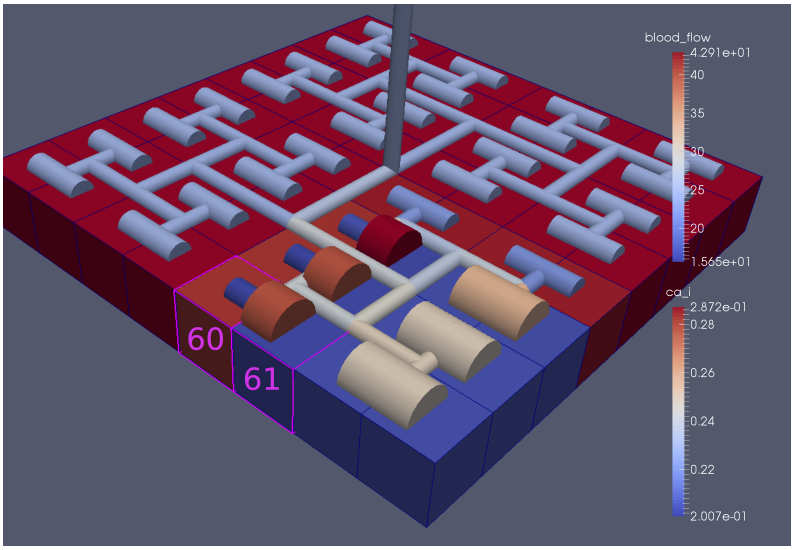

Figure 41: A square of 9 tissue blocks (shown in blue) is activated with neuronal K^+ release (F_{input} = 2.5).

arisation of the SMC. The Ca^{2+} and radius in cell 60 (outside of the activated area) shows only a small perturbation with the radius reaching a constant value slightly lower than the steady state, due to the effect of the conservation of mass at the junction of the vessel segments that perfuse cells 60 and 61.

Figure 43 shows a tissue block slice of size 4 $\times$ 4 with different number of activated blocks. In Figure 43a) the neuron is activated in the area denoted by a 1 $\times$ 1 sub-block and in b) increased to a 2 $\times$ 2 sub-block. Here, the colour mapped onto the tissue blocks denotes the K^+ concentration in the SC. Again, vessels in the activated area dilate due to neuronal activity. When a leaf vessels lays in the activated area and is surrounded by other non-activated blocks its dilation is larger than if surrounded by activated blocks (compare vessel 0 in Figure 43c) and Figure 43d)). Also, the time-dependent profiles of the bloodflow in the tree segments that feed vessel 0 are shown. When only one block is activated the vessel response during activation decreases with increasing level in a non-linear fashion (see Figure 43c)). However, when

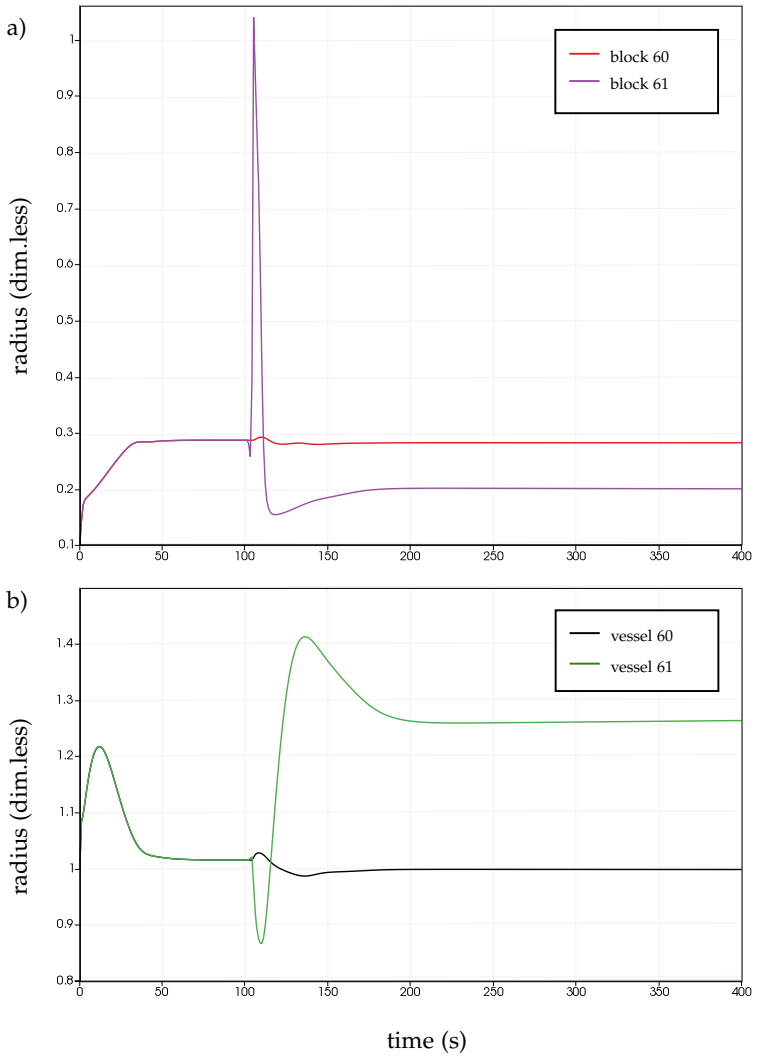

Figure 42: a) Ca^{2+} concentration in the SMC changes in two adjacent tissue blocks and b) radius dynamics in the corresponding leaf branches. Tissue block and leaf vessel 60 lay in a non-activated area and 61 in an area which is activated with a time-dependent K^+ input (F_{input} = 2.5). NVU tissue blocks and vasculature are bidirectionally coupled (stretch-activated channels enabled).

more tissue blocks are activated the leaf vessels in the activated area and their parents exhibit the same (relative) increase in bloodflow (see vessels 0, 16 and 24 in Figure 43d)). Furthermore, with a larger activated area, the root vessel (number 30) shows an increased radius and hence bloodflow compared to that with a smaller activated area.

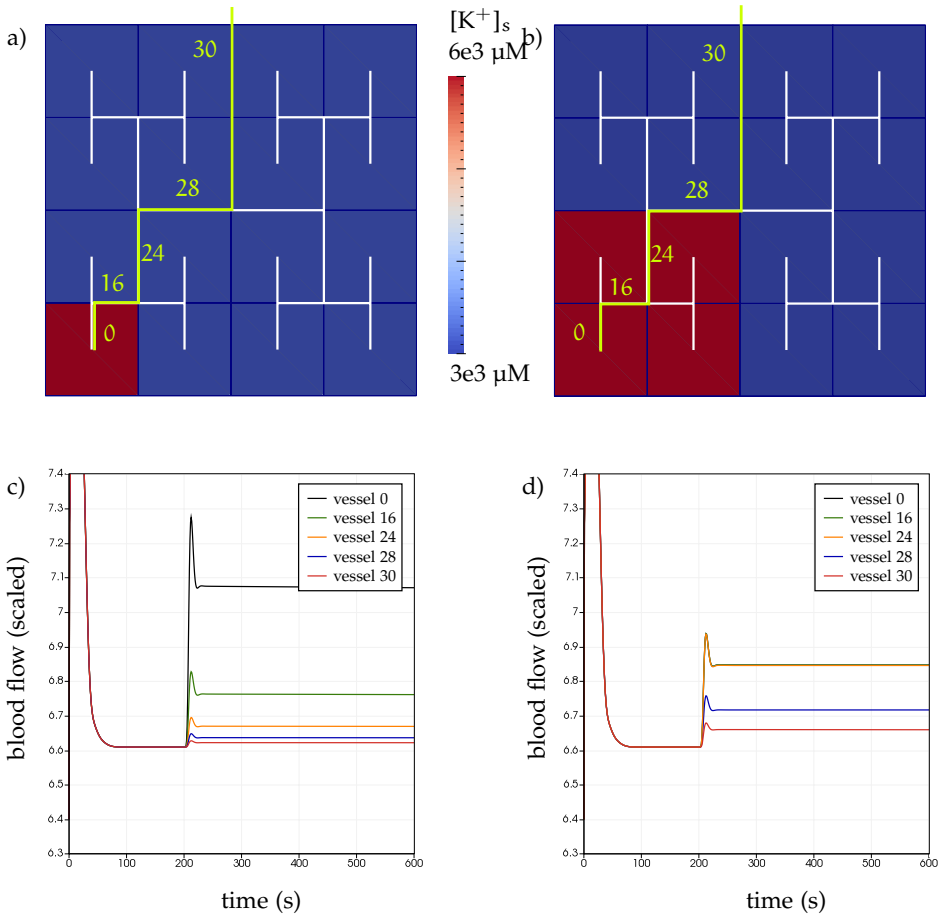

Figure 43: Bloodflow change in the vessels upon a time-dependent K^+ input (F_{input} = 2.5) in different activated areas.

7.3.2.2 *Lumen Agonist Activation Only*

Figure 44 shows a detail of a 64 block simulation. The small 9 × 9 block (red) has a constant agonist flux of 0.4 µM s^{-1} whilst the remaining blocks (blue) have a constant value of 0.18 µM s^{-1}. Two blocks are also highlighted where one block lies within the high agonist domain (cell 61) and the other (cell 60) lies adjacent but inside the low agonist domain.

Figure 45 shows the time-dependent profiles of radii in the two adjacent blocks (cells 60 and 61). Since the agonist flux of 0.4 µM s^{-1} is high enough

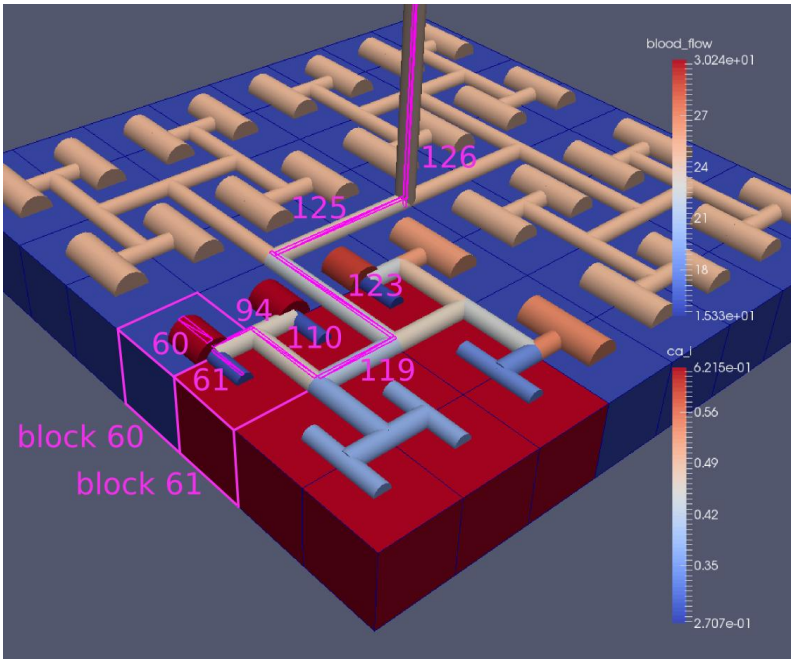

Figure 44: A square of 9 tissue blocks is activated with an increased luminal agonist flux (0.4 µM s^{-1}). As a response, vessel radii in the activated area become oscillatory. The vessel segments are numbered from the root (126) to the leaf (60, 61). Radial diameters are shown proportional to their size and colour mapped as proportional to bloodflow. Tissue blocks are coloured proportional to SMC Ca^{2+}.

to include oscillation in the SMC, this is shown clearly in Figure 45 both in the radius of cell 61 (in the high flux domain) and in the cytosolic Ca^{2+} of the associated SMC. Additionally, although Ca^{2+} in the block outside of the high flux domain is constant, the corresponding radius does exhibit small oscillations and indicates that the vasculature provides a form of coupling to other perfusing segments of the tree.

Figure 44 shows numbered segments of the vasculature from the root segment (126) to the activated leaf of the H-tree (61). Figure 46 shows the corresponding bloodflow time dependent profiles for the number segments (60,...126). We see that the root (segment 126) has the lowest flow but contains the sum of all the lower mass flow rates and has the largest radius. Interestingly the blood flow to the two cells (60 and 61) both exhibit oscilla-

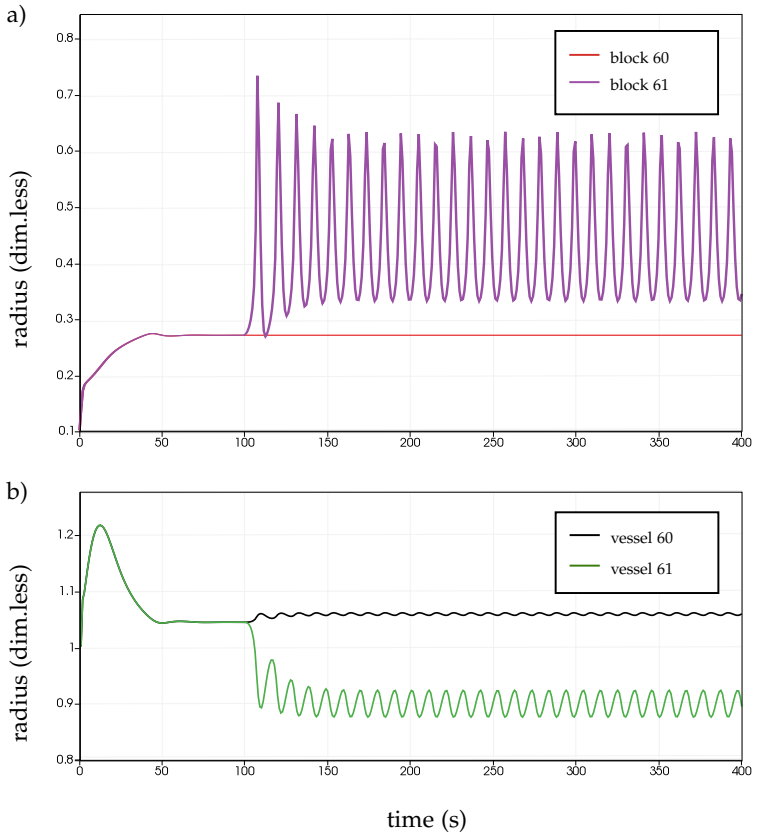

Figure 45: SMC Ca^{2+} concentration changes in two adjacent tissue blocks and radius dynamics in the corresponding leaf branches. Tissue block and leaf vessel 60 lay in a non-activated area and 61 in an area which is activated with a time-dependent luminal agonist flux (0.4 µM s^{-1}). NVU tissue blocks and vasculature are uncoupled (stretch-activated channels disabled).

tions. Cell 61 has the lowest bloodflow and this is due to the fact that its Ca^{2+} has a high temporal average and thus induces a constriction. Conversely, the cell adjacent but outside of the high agonist domain has the highest bloodflow in order to maintain mass (flow) conservation. The remaining segments exhibit oscillations due to pressure variations within the vasculature. Hence even though the vasculature and tissue blocks are effectively decoupled by forcing the pressure term in equation (7.1) to be constant, the tissue blocks outside of the activated domain are dynamic. Figure 47 shows a 64 tissue block with associated vasculature where the tissue colour map simulates

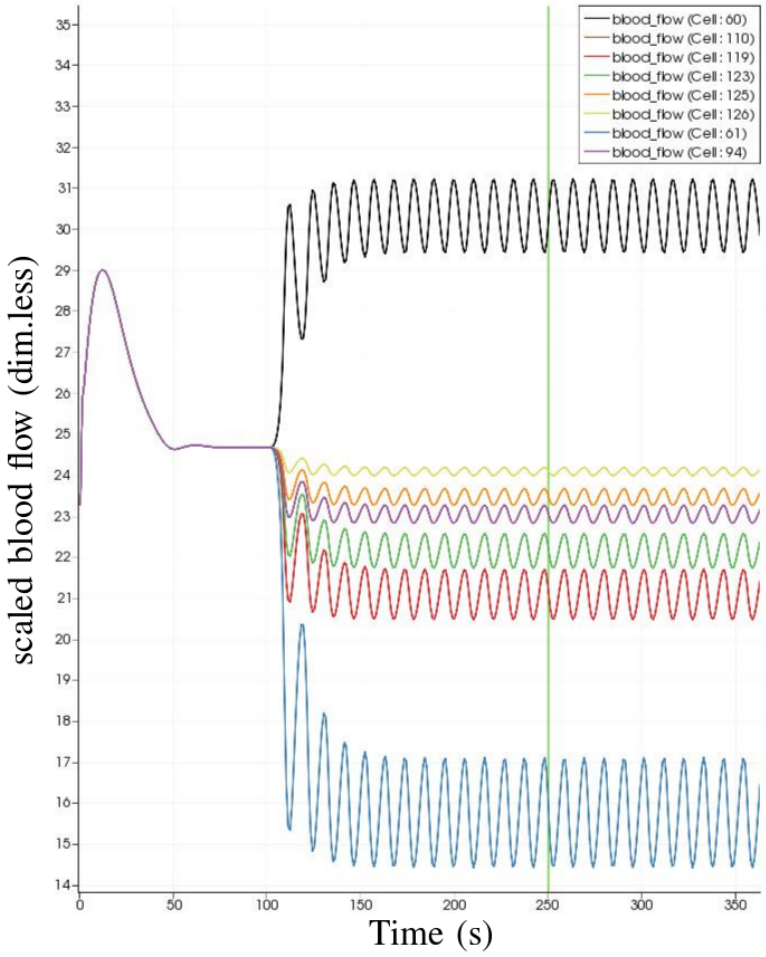

Figure 46: Bloodflow time-dependent profiles in vessel segments (60, 61, 94, 110, 119, 123, 115, 126). Tissue block and leaf vessel 60 lay in a non-activated area and 61 in an area which is activated with a time-dependent luminal agonist flux (0.4 µM s^{-1})

cytosolic SMC Ca^{2+} and the vascular colour indicates bloodflow. In this case, the agonist profile is varying linearly from top to bottom of the tissue block. Four blocks are highlighted and numbered 0, 3, 5, 7. Figure 48 (top) shows the time dependent Ca^{2+} profiles in the four tissue blocks for the decoupled case, shown as an overview in Figure 47. The agonist profile is such that the top two block rows and that of the bottom three are such as to produce a steady state in the SMC Ca^{2+}. All other rows induce oscillations in the SMC compartment of the NVU. Figure 48 (bottom) shows the same situation, but

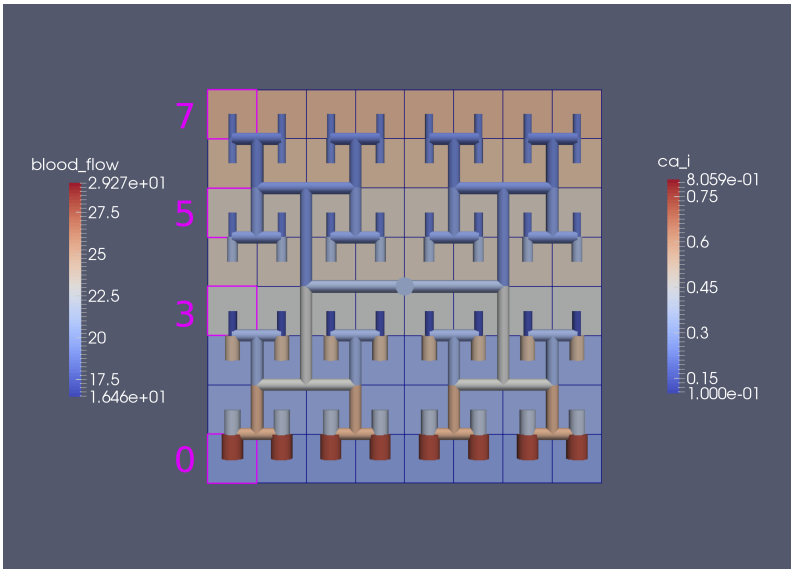

Figure 47: 64 tissue block with agonist profile is varying linearly from top to bottom of the tissue block. The tissue colour map simulates cytosolic SMC Ca^{2+} and the vascular colour indicates bloodflow. The size of the radial segments indicates the actual radius of the vessel segment. Four blocks are highlighted and numbered 0, 3, 5, 7.

where the coupling between NVU and vasculature is active, (i.e. the stretch channel has the radius and pressure terms changing). Comparison of the profiles show only a small change, most notably in the Ca^{2+} of cell block 3. The Ca^{2+} in the coupled case has a higher frequency and the profile is more sinusoidal in shape indicating that the calcium mediated channels are opening more quickly.

7.3.2.3 *Neuronal and Agonist Activation*

For this case the neuron is activated by both an increase in K^{+} in the synaptic cleft and an increase in agonist concentration over the highlighted area. Figure 49 shows the tissue blocks and numbered cells on the border of the activated area. Figure 50 shows for cells numbered 60, 61 and 62 the time dependent profiles for both radius and Ca^{2+}. Tissue cell 60 (outside of the activated area) has the largest radius and the lowest Ca^{2+} perturbed only a

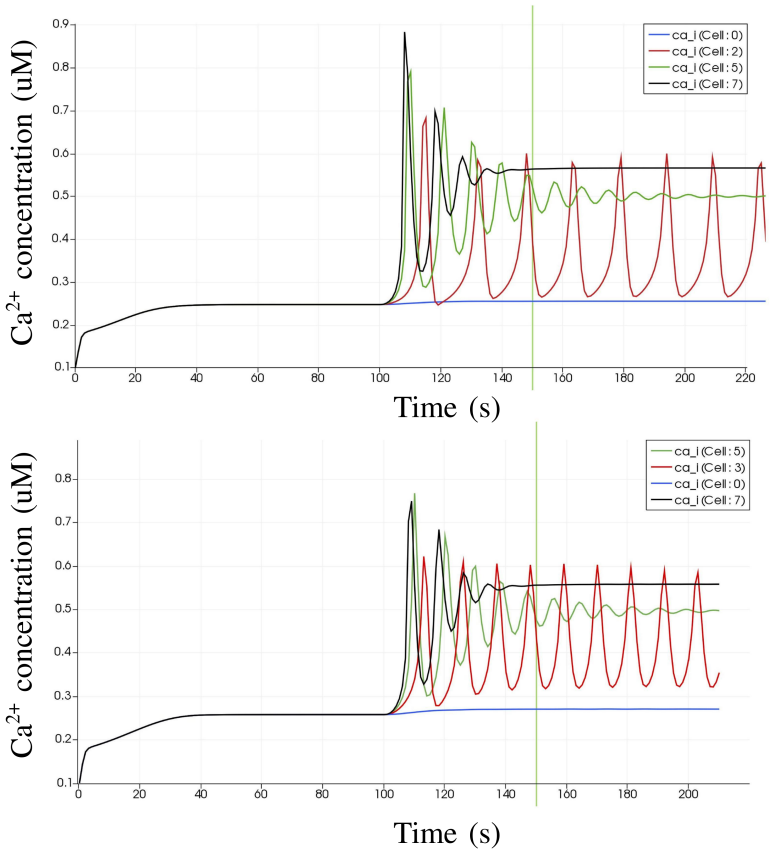

Figure 48: Time dependent Ca^{2+} profiles in the four tissue blocks for the decoupled (top) and coupled (bottom) case shown as an overview in Figure 47.

small value from equilibrium but showing small amplitude oscillations. This is a particular effect of the vasculature on the system since if the vasculature was decoupled then the radius and Ca^{2+} would be of a constant value. For the cells (61 and 62) inside the activated area the time dependent profiles indicate that there exists a phase difference between both radius and Ca^{2+}. The phase difference increases as time progresses. Because the time averaged value of Ca^{2+} for both cells 61 and 62 is high, the radius attains a constricted value compared to the equilibrium state.

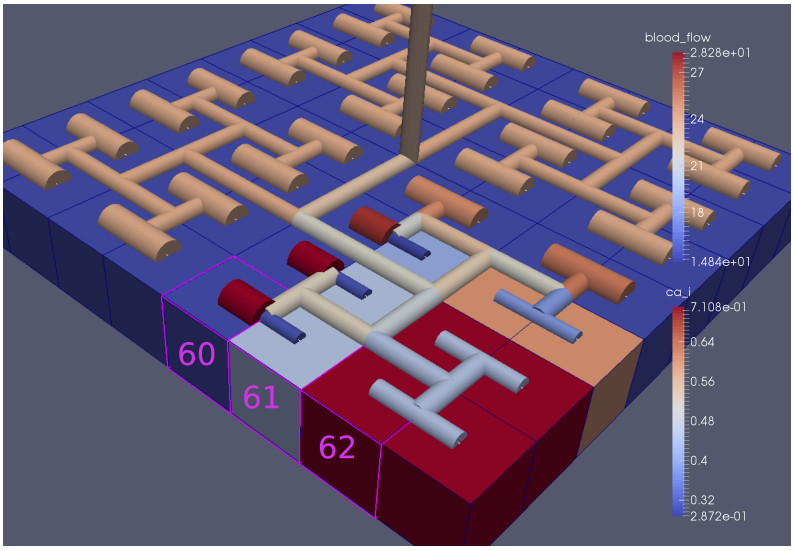

Figure 49: 64 block with both neuronal and agonist activation. Highlighted blocks indicate outside (60), boundary (61) and inside (62) the activated domain.

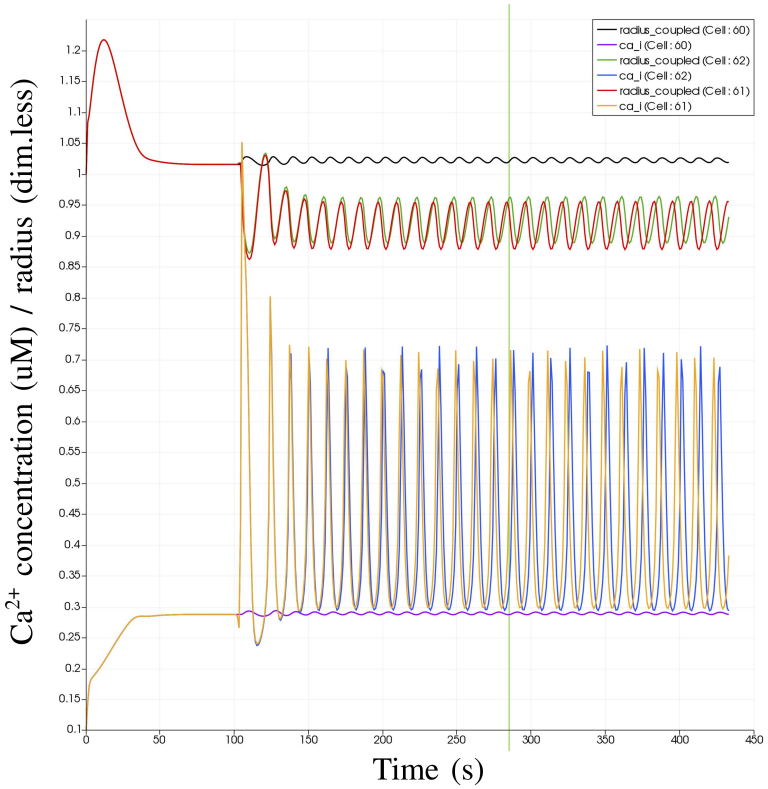

Figure 50: Time dependent profiles for both radius and Ca^{2+} for cells numbered 60, 61 and 62.

7.3.3 *Diffusion*

Figure 51 shows the effect diffusion has on the steady-state distribution of K^+ in the PVS. In both cases a sub-block of 8 × 8 tissue blocks was activated with a neuronal K^+ input. The AC in the NVU model within each tissue block takes up K^+ from the SC and subsequently releases K^+ into the PVS upon stimulation. Figure 51 a) depicts the perivascular K^+ distribution without diffusion. Here, there is a sharp edge between the K^+ concentration in the activated and the non-activated areas. When linear diffusion of K^+ between adjacent tissue blocks is activated, a steady-state gradient between the two areas evolves (see Figure 51 b)).

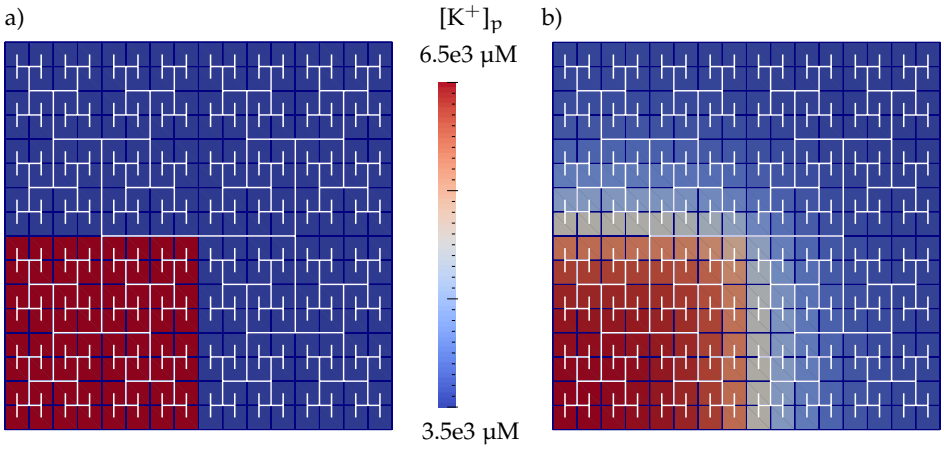

Figure 51: Steady state distribution of K^+ in the perivascular space during neuronal activation only in the activated area denoted by an 8 × 8 sub-block. a) Without diffusion, b) with linear diffusion of $[K^+]_p$ between adjacent tissue blocks.

7.3.4 *Nitric Oxide Signalling Pathway*

The vascular tree model with the coupled NVU models can be used to also include model extensions, such as the NO signalling pathway. Figure 52

shows a 4096 block tissue slice with the NO signalling pathway (described in Chapter 6) included in the NVU blocks. The colour mapped onto the blocks depicts the NO concentration in the SMC. A Gaußian neuronal input signal is given in the centre of the tissue slice. Figure 52b) shows the time-dependent profiles of the NO concentration in the SMC in the highlighted blocks. The SMC receives NO from two sources, the NE and the EC. During neuronal stimulation NO production in the postsynaptic NE increases. The NO release from the luminal side depends on the wss that is created through increased blood-flow. The NO concentration in the SMC is higher the closer the tissue block is to the centre of the activated area. The wss-mediated NO production in the EC forms a further coupling mechanism of the vasculature-tissue interactions.

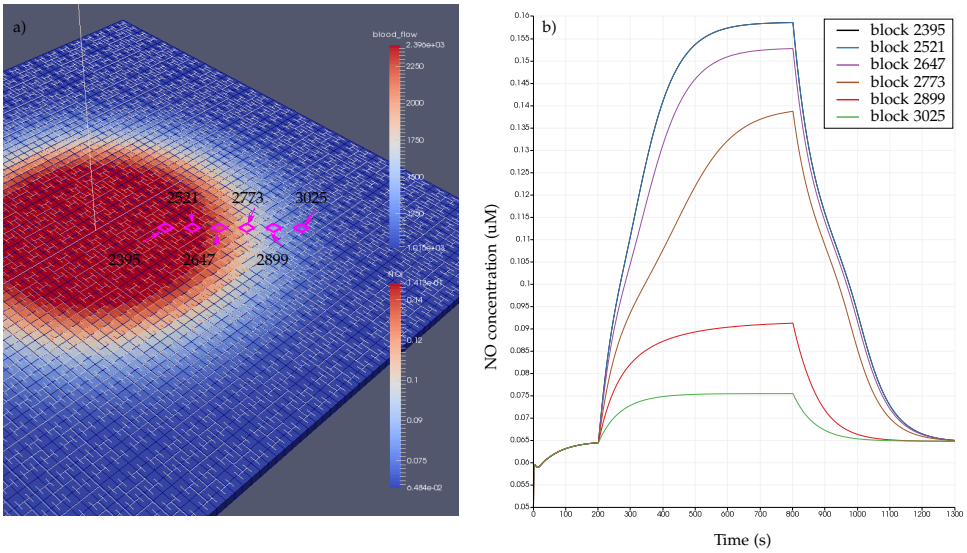

Figure 52: The NO dynamics in the vascular tree model.

7.4 DISCUSSION

We have developed a coupled model which links a large dynamic vascular tree to a set of neurovascular coupling units whose details can be found in the previous chapters. Coupling is enabled by the inclusion of a variable pressure in the stretch-activated ion channel (see equation 7.1). We have implemented three basic cases where a specific area of the tissue blocks is activated by either neuronal activation and the corresponding increase in perivascular K^+, or the increase in agonist concentration, or both. Scaling results show that strong scaling provides a near ideal profile, and weak scaling results indicate that the parallel algorithm is close to optimal parallelisation.

Figures 41 to 50 show a series of results from the three basic cases. They show that on the basis of the single stretch-activated channel per NVU block the effect of the vasculature coupling with the NVU shows only a weak association. However, there are interesting phenomena occurring on the boundaries of subdomains activated by either neuronal activity or agonist concentration. As expected for a purely neuronal activation, the solution reaches a steady state, with segments outside of the activated area reaching values slightly smaller than the equilibrium. For the agonist induced case, only the Ca^{2+} in cells inside the activated area becomes oscillatory. However, the radii of cells both inside and outside the activated area oscillate (albeit small for those outside). This shows the effect of the coupling through the pressure variations evaluated in the vascular tree, although these are small. It is interesting to investigate the difference between profiles exhibited with and without coupling. Again, only small differences occur and a slightly higher time averaged Ca^{2+} occurs with the coupled system. This is due to the increase in the open probability of the stretch mediated ion channel and inducing a larger flux of Ca^{2+} into the cytosol of the SMC and EC. In addition.

the oscillation profile differs between coupled and decoupled states with the time required to refill the cytosol with decreasing Ca^{2+} and increasing frequency with coupling.

Diffusion of species between tissue blocks is an interesting addition to the model. It allows a more physiological model of ion dynamics in the ECS, but also between cells that are coupled through GJ like SMCs and ECs are. Figure 51 shows the case of introducing diffusion for K^+ in the PVS. This is not a very physiological example of cerebral K^+ diffusion. However, it shows how diffusion of a given species acts on the overall steady-state concentration distribution in the tissue slice. Further work will include the diffusion of extracellular K^+ and can potentially be helpful for the study of underlying mechanisms in cortical spreading disease, where K^+ waves in the ECS are observed (Dreier, 2011).

The present vascular tree model preserves the character of modularity introduced with the single NVU model in Chapter 4. Model extensions, such as the NO signalling pathway described in Chapter 6, can be added in a straightforward manner. Adding the NO signalling pathway into the vascular tree model increases the number of coupling mechanisms between the tissue and the vasculature. This is due to the fact that wss is a trigger for the production of endothelial derived NO, which causes vasodilation *via* the cGMP pathway (Yang et al., 2005), see Figure 52.

8

CONCLUDING REMARKS

The NVC mechanisms to assure an adequate supply of blood perfusion in the human brain exhibit a high level of complexity. A variety of cerebral cell types, called neurovascular unit (NVU), work together to delicately regulate perfusion, which is required for the supply of nutrients to sustain cerebral activity.

Recent studies suggest that impaired cerebral perfusion is associated with neurodegenerative disorders such as AD and other cerebral diseases (Zlokovic, 2005). Nevertheless, underlying mechanisms of NVC under normal and pathological conditions are still poorly understood.

Mathematical modelling can be a useful tool to elucidate physiological processes and to guide directions for further experiments. However, the development of computational models for NVC is a challenging task. As in any biophysical model, one of the difficulties is to obtain the right balance between detail and complexity. The present work focusses on the use of physiological rather than phenomenological models. This allows the study of underlying mechanisms and identify governing NVC contributors.

The aims of the present research were accomplished in two main model development phases. In a first step, a biophysical model of a single NVU was developed, which successfully coupled neuronal activity to a vascular response and which was extended further by including additional important signalling pathways. The second step was to embed the single NVU model in a large tissue-like structure, which is coupled to the cerebral vasculature

and allows the study of NVC interactions on the vascular level. The presented model is the first of its kind, leading the way in modelling the whole NVC process.

8.1 SINGLE NVU MODELS

A mathematical foundation model, based on the K^+ and smooth muscle Ca^{2+} pathway, was developed. It describes NVC from a neuronal input signal to the mechanical vessel response. The model successfully predicts vasodilation upon neuronal activity. This research aim was accomplished by further developing available models found in the literature and extending them to include additional ion channels, intercellular coupling and a mechanical model to describe temporal variations in vessel diameter. The compartment lumped parameter approach chosen in this work provides a certain degree of simplicity, as spatial homogeneity is assumed and therefore no partial differential equations are needed to describe rates of change of species' concentrations. However, we are aware of the fact that spatial gradients may be important for some physiological mechanisms.

In the NVU foundation model neuronal activity is modelled as K^+ release from the NE. This leads to an increase of K^+ in the SC, which is taken up by the AC surrounding the SC with its processes. The AC then successively releases K^+ into the PVS through its endfoot close to the arteriole. Changes of K^+ in the SMC cytosol lead to hyperpolarisation of the cell and therefore mediate the closure of VOCCs. Less Ca^{2+} enters the cell and is available for actin-myosin crossbridge formation. This leads to vasodilation and therefore an increase in bloodflow providing more nutrients and oxygen during neuronal activity. The observed increase in radius of 27.4 % is in agreement with

experimental data from Hillman et al. (2007), who obtain rapid dilation of pial arterioles upon fore- and hind-paw stimulation of 17 % to 29 % in rats *in vivo*. The detailed physiological model allows us to investigate the importance of different ion channels.

The NVU model was developed such that new aspects can be added straightforwardly. This modular character is an important feature of the model, as there are numerous signalling pathways that mediate the perfusion response (LeCrux and Hamel, 2011), of which some may not be discovered yet. Modularity allows the analysis of single signalling pathways, and additive effects when combined and comparison between corresponding impacts.

In the present work NO and luminal agonist ATP were identified as further important signalling molecules. The inclusion in the NVU foundation model is able to analyse the contribution of these pathways. ATP has a considerable effect on NVC *via* the IP_3 pathway. During neuronal activity the mean vascular response is reduced. However, vasomotion is induced, a beneficial reaction, which is known to increase perfusion in the capillary bed (Intaglietta, 1991). The main effects of including NO in the NVU model are a shift in the resting radius value towards a more dilated state and an enhanced dilation during neuronal activation.

The single NVU model has allowed the study of interesting phenomena during normal and pathological conditions *in silico* and can be used to explain and analyse underlying mechanisms of NVC.

8.2 THE VASCULAR-TREE MODEL

Cerebral cells exhibit complex signalling pathways not only within the NVU, but also *via* diffusion in the ECS and coupling with the vasculature. To study

the NVC phenomena at this macro scale, the single NVU model was extended into a network of tissue blocks coupled with (embedded within) a spatially-embedded binary tree representing the cerebral vasculature.

Different input signals were given, namely a neuronal K^+ release, luminal agonist and a combination of the two. It could be shown that the ratio of the activated tissue blocks influences the vascular response on the arteriolar level, but also further up the vascular tree. Coupling between the vasculature and the tissue was achieved by stretch-activated channels in the ECs and SMCs. Coupling the vasculature to the NVU *via* these Ca^{2+} channels changes the time-dependent profiles of bloodflow and reveals a myogenic response of the arteriole, i.e. the increase in intraluminal pressure induced a (small) increase in Ca^{2+} concentration in the SMC and therefore vessel constriction (Takenaka et al., 1998).

Furthermore, the model is able to investigate the relationship between oscillatory states of the ECs/SMCs and the resulting motion of the vasculature.

8.3 COMPUTATIONAL INFRASTRUCTURE

The construction of the single NVU models was done in `MATLAB` (R2014b, Math-Works, Massachussets, U.S.A.), which provides many implemented algorithms and tools that allow a fast and straightforward construction of a simple model. Nevertheless, to use the high performance computers of UC HPC, the transfer of the model into `C` and parallelisation of the code was necessary.

Scaling the NVU model into the vascular tree model and the use of multiple computational frameworks and programming languages, however, has led to difficulties during the present work. Due to the large number of para-

meters, algebraic expressions and ordinary differential equations problems arise when models or model segments are transferred from one platform to another.

Our research group has looked into possibilities to avoid these issues and provide a more user-friendly interface for the development of complex models as well as the scaling into tissue-like structures. We have developed a programme, the neurovascular simulator (NVS), which is based on the template system `Mako` for `Python` and has shown promising initial performance results. An overview of the programme idea is given in Figure 53.

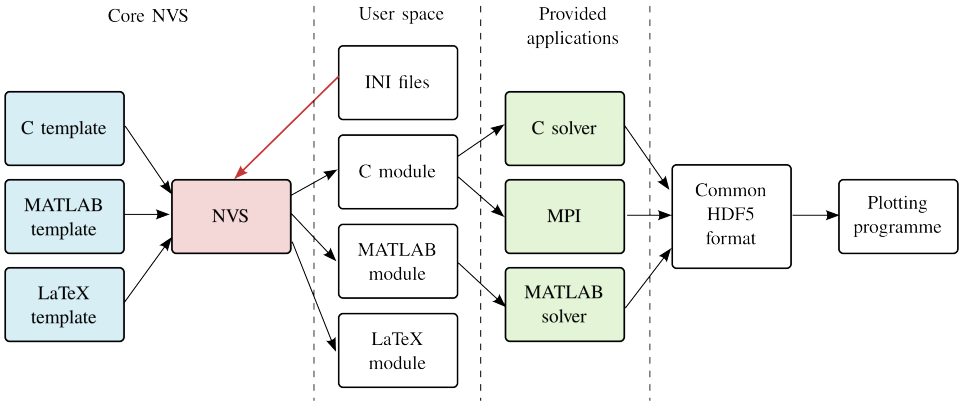

Figure 53: Layout of the `NVS` program functionality. The user provides input to the program *via* the INI files and can access the different modules. The NVS core, including the NVS program and the templates, is not exposed to the user.

The `NVS` program only needs to receive a simplistic input, in the form of INI files, and then automatically generates simulation code in `MATLAB` and `C`, together with LaTeX documentation files, that all hold an identical copy of the model equations and parameters. The code will be generated for a single NVU model and for multiple NVUs embedded in the vascular tree model. The INI file format is a simple text file, which is commonly used for configuration files. It has the filename extension, .ini, which stands for "initialisation". It is separated into sections specified by the following headers:

- Initial values for the state variables of the system will be listed under `[initial]`.
- Parameters to the module will be listed under `[parameters]`. Users may specify the units of their parameters by inserting them after the parameter value, separated by a comma.
- The optional `[input]` section contains variables to which input from an external source will be assigned.
- Algebraic expressions will be listed under `[algebraic]`.
- ODEs will be listed under `[ode]`.

A unique identifier for each model module will be given at the top of the file. An example INI file of the Hai and Murphy (1988) model is given in Listing 1

Listing 1: An example INI file for the Hai and Murphy (1988) model.

```
identifier = haimurphy


[initial]
M_p = 0.19
AM_p = 0.7
AM = 0.08


[parameters]
gam = 17 , uM^{-3} s^{-1}
K_2 = 0.5 , s^{-1}
K_3 = 0.4 , s^{-1}
K_4 = 0.1 , s^{-1}
K_5 = 0.5 , s^{-1}
K_7 = 0.1 , s^{-1}
```

```
[input]
Z =

[algebraic]
K_1 = gam * Z**3
K_6 = gam * Z**3
M = 1 - M_p - AM - AM_p

[ode]
dM_p_dt = K_4 * AM_p + K_1 * M - (K_2 + K_3) * M_p
dAM_p_dt = K_3 * M_p + K_6 * AM - (K_4 + K_5) * AM_p
dAM_dt = K_5 * AM_p - (K_7 + K_6) * AM
```

The INI files are processed by a Python script. It extracts the information contained in them and passes it to Mako templates, which generate C and MATLAB code. Due to its user-friendly interface and the fast code generation, the NVS program has added a high amount of convenience to the handling of mathematical models. It will also help with the further development of the present NVU model as it simplifies the exchange and inclusion of new model components.

8.4 FUTURE WORK

The presented work could be extended in several ways.

Further research would benefit from investigation into the development of a more detailed NE model that can be included in the NVU. The NE model used in this work only comprises one compartment. To simulate interactions in neuronal networks it will be necessary to focus on multiple sections

of the NE that can be modelled as connected compartments, such as that described by Chang et al. (2013). Furthermore, the NE model should contain Ca^{2+} dynamics, because of the known importance in neurodegenerative diseases such as AD (Woods and Padmanabhan, 2012).

An extended NE model would also require a compartment for the ECS as the NE strongly interacts with this surrounding space. The inclusion of the ECS compartment will also allow us to investigate diffusion in the cerebrospinal fluid (CSF), which plays an important role in cell-to-cell signalling processes (Syková and Nicholson, 2008). The K^+ waves observed in ECF would be of particular interest from a modelling perspective.

Up to this point, the NE and AC compartments in our model are coupled only through K^+ exchange, because it is known to be one of the most important signalling molecules in NVC. There is growing evidence that there are also metabolic interactions between the two cell types that may play a crucial role in cerebral homeostasis. ACs supply NEs with energy metabolites, such as glutamine, and are involved with neurotransmitter recycling (Allaman et al., 2011). A metabolic model presented by Cloutier et al. (2009) includes mitochondria energy production *via* the TCA cycle and a lactate shuttle between NE and AC. Preliminary unpublished work carried out by our research group suggests that the incorporation of the Cloutier et al. (2009) model into our NVU model is a promising extension.

We were careful to omit astrocytic Ca^{2+} dynamics in our NVU foundation model in order to study the K^+ pathway in isolation. Our results suggest that Ca^{2+} is not the only mediating signalling pathway in NVC. Exploring the relative contributions of different pathways, such as the astrocytic and neuronal Ca^{2+} dynamics, however, will be an interesting research aim for further studies. It is important to investigate the effect Ca^{2+} has on the neuronal function and how it is disturbed from its non-pathological equilibrium. In

particular we will concentrate on simulating the role of the Ca^{2+}-mediated TRPV4 ion channel, which is known to be enhanced under increased A-β concentration and to contribute to hippocampal damage with resulting Ca^{2+} dyshomeostasis (Bai and Lipski, 2014).

Including other cell types, such as other types of microglia or pericytes, would provide further insights into interactions in the NVU. There is contradictory evidence concerning whether or not pericytes play an important role in the NVC signalling. Hamilton et al. (2010) promotes the idea that pericytes modulate capillary diameter in response to neural activity, whereas Hill et al. (2015) clearly indicate that pericytes do *not* have contractile properties. Our mathematical model might be able to help clarify the previous findings and suggest further experiments.

As our model is becoming increasingly complex and the number of state variables and parameters is increasing steadily over time, analytical methods could help to simplify and reduce aspects of the model without losing important capabilities. Non-dimensionalisation, uncertainty quantification and sensitivity analysis provide promising tools to accomplish this aim.

At present, the variation in arteriolar vessels only occurs at the leaves of the vascular tree model. The future model will include variations in upstream segments of the vasculature utilising a simple pressure balance.

The vascular model will further benefit from investigations of O_2 flux from the perfusing vessel into the NVU providing energy to the ATPase pump of the NE. Furthermore, the incorporation of the wss-induced ATP production and its influence on IP_3 and subsequent pathways will be interesting to study.

A

APPENDIX

A.1 MODEL EQUATIONS AND PARAMETERS OF THE NVC FOUNDATION MODEL

Neuron/Astrocyte Submodule

Input signals

Neuronal K^+ input signal (dim.less):

$$f_{K/Na}(t) = \begin{cases} F_{input}\frac{(\alpha_n+\beta_n-1)!}{(\alpha_n-1)!(\beta_n-1)!}\left(\frac{1-(t-t_0)}{\Delta t_2}\right)^{\beta_n-1}\left(\frac{t-t_0}{\Delta t_2}\right)^{\alpha_n-1}, & \text{for } t_0 \leqslant t < t_1 \\ -F_{input}, & \text{for } t_2 \leqslant t \leqslant t_3 \\ 0, & \text{otherwise} \end{cases} \quad (A.1)$$

End of neuronal pulse (s):

$$t_1 = t_0 + \Delta t \quad (A.2)$$

Start of back-buffering (s):

$$t_2 = t_0 + \Delta t_1 \quad (A.3)$$

End of back buffering (s):

$$t_3 = t_1 + \Delta t_1 \quad (A.4)$$

F_{input}	amplitude scaling factor	2.5	ME[1]
α_n	beta distribution constant	2	ME
β_n	beta distribution constant	5	ME
t_0	start of neuronal activation	model input (s)	
Δt_1	length of neuronal activation	model input (s)	
Δt_2	time-scaling factor	10 s	(Østby et al., 2009)

Scaling

Astrocyte volume-area ratio (m):

$$\frac{dR_k}{dt} = L_p([Na^+]_k + [K^+]_k + [Cl^-]_k + [HCO_3^-]_k - [Na^+]_s - [K^+]_s - [Cl^-]_s - [HCO_3^-]_s + \frac{X_k}{R_k}) \quad (A.5)$$

1 Model Estimation

Synaptic cleft volume-surface ratio (m):

$$R_s = R_{tot} - R_k \tag{A.6}$$

L_p	total water permeability per unit area of the astrocyte	2.1×10^{-9} m $\mu M^{-1} s^{-1}$	(Østby et al., 2009)[2]
X_k	Number of negatively charged impermeable ions trapped within the astrocyte divided by the astrocyte membrane area	12.41×10^{-3} μM m	(Østby et al., 2009)
R_{tot}	Total volume surface ratio AC + SC $((V_{sc}+V_k)/A_k)$	8.79×10^{-8} m	(Østby et al., 2009)[2]
A_k	characteristic exchange surface area	3.7×10^{-9} m^2	(Østby et al., 2009)[3]

Differential equations

SYNAPTIC CLEFT

K^+ concentration in the SC (times the SC volume-area ratio R_s; in μM m):

$$\frac{dN_{K,s}}{dt} = k_C f(t) - \frac{dN_{K,k}}{dt} - J_{BK,k}\,; \quad [K^+]_s = \frac{N_{K,s}}{R_s} \tag{A.7}$$

Na^+ concentration in the SC (times the SC volume-area ratio R_s; in μM m):

$$\frac{dN_{Na,s}}{dt} = -k_C f(t) - \frac{dN_{Na,k}}{dt}\,; \quad [Na^+]_s = \frac{N_{Na,s}}{R_s} \tag{A.8}$$

HCO_3^- concentration in the SC (times the SC volume-area ratio R_s; in μM m):

$$\frac{dN_{HCO_3,s}}{dt} = -\frac{dN_{HCO_3,k}}{dt}\,; \quad [HCO_3^-]_s = \frac{N_{HCO_3,s}}{R_s} \tag{A.9}$$

k_C	Input scaling parameter	7.35×10^{-5} μM m s^{-1}	(Østby et al., 2009)

2 corrected value/unit obtained from `CellML`
3 corrected value/unit obtained from communication with author

ASTROCYTE

K^+ concentration in the AC (times the AC volume-area ratio R_k; in µM m):

$$\frac{dN_{K,k}}{dt} = -J_{K,k} + 2J_{NaK,k} + J_{NKCC1_k} + J_{KCC1_k} - J_{BK,k}\,; \quad [K^+]_k = \frac{N_{K,k}}{R_k} \tag{A.10}$$

Na^+ concentration in the AC (times the AC volume-area ratio R_k; in µM m):

$$\frac{dN_{Na,k}}{dt} = -J_{Na,k} - 3J_{NaK,k} + J_{NKCC1_k} + J_{NBC,k}\,; \quad [Na^+]_k = \frac{N_{Na,k}}{R_k} \tag{A.11}$$

HCO_3^- concentration in the AC (times the AC volume-area ratio R_k; in µM m):

$$\frac{dN_{HCO_3,k}}{dt} = 2J_{NBC,k}\,; \quad [HCO_3^-]_k = \frac{N_{HCO_3,k}}{R_k} \tag{A.12}$$

Cl^- concentration in the AC (times the AC volume-area ratio R_k; in µM m):

$$\frac{dN_{Cl,k}}{dt} = \frac{dN_{Na,k}}{dt} + \frac{dN_{K,k}}{dt} - \frac{dN_{HCO_3,k}}{dt}\,; \quad [Cl^-]_k = \frac{N_{Cl,k}}{R_k} \tag{A.13}$$

Open probability of the BK channel (non-dim.):

$$\frac{dw_k}{dt} = \phi_w\,(w_\infty - w_k) \tag{A.14}$$

PERIVASCULAR SPACE

K^+ concentration in the PVS (in µM):

$$\frac{d[K^+]_p}{dt} = \frac{J_{BK,k}}{R_k R_{pk}} + \frac{J_{KIR,i}}{R_{ps}} - R_{decay}([K^+]_p - [K^+]_{p,min}); \tag{A.15}$$

R_{pk}	Volume ratio of PVS to AC	10^{-3} [-]	(Nagelhus et al., 1999)
R_{ps}	Volume ratio of PVS to SMC	10^{-3} [-]	(Nagelhus et al., 1999)
R_{decay}	Decay rate	0.05 s^{-1}	M.E.
$[K^+]_{p,min}$	minimum K^+ concentration	3×10^3 µM	M.E.

Fluxes

K^+ flux (times the AC volume-area ratio R_k; in $\mu M\ m\ s^{-1}$):

$$J_{K,k} = \frac{g_{K_k}}{F}(v_k - E_{K,k}) \tag{A.16}$$

Na^+ flux (times the AC volume-area ratio R_k; in $\mu M\ m\ s^{-1}$):

$$J_{Na,k} = \frac{g_{Na_k}}{F}(v_k - E_{Na,k}) \tag{A.17}$$

Na^+ and HCO_3^- flux through the NBC channel (times the AC volume-area ratio R_k; in $\mu M\ m\ s^{-1}$):

$$J_{NBC,k} = \frac{g_{NBC,k}}{F}\,(v_k - E_{NBC,k}) \tag{A.18}$$

Cl^- and K^+ flux through the KCC1 channel (times the AC volume-area ratio R_k; in $\mu M\ m\ s^{-1}$):

$$J_{KCC1,k} = C_{input}\frac{g_{KCC1,k}}{F}\frac{R_{gas}T}{F}\ln\left(\frac{[K^+]_s[Cl^-]_s}{[K^+]_k[Cl^-]_k}\right) \tag{A.19}$$

Na^+, K^+ and Cl^- flux through the NKCC1 channel (times the AC volume-area ratio R_k; in $\mu M\ m\ s^{-1}$):

$$J_{NKCC1,k} = C_{input}\frac{g_{NKCC1,k}}{F}\frac{R_{gas}T}{F}\ln\left(\frac{[Na^+]_s[K^+]_s{[Cl^-]_s}^2}{[Na^+]_k[K^+]_k{[Cl^-]_k}^2}\right) \tag{A.20}$$

Flux through the sodium potassium pump (times the astrocyte volume-area ratio R_k; in $\mu M\ m\ s^{-1}$):

$$J_{NaK,k} = J_{NaK,max}\frac{{[Na^+]_k}^{1.5}}{{[Na^+]_k}^{1.5} + {K_{Na,k}}^{1.5}}\frac{[K^+]_s}{[K^+]_s + K_{K,s}} \tag{A.21}$$

K^+ flux through the BK channel (times the astrocyte volume-area ratio R_k; in $\mu M\ m\ s^{-1}$):

$$J_{BK,k} = \frac{g_{BK,k}}{F}w_k\,(v_k - E_{BK,k}) \tag{A.22}$$

F	Faraday's constant	9.649×10^{4} C mol^{-1}	
R_{gas}	Gas constant	8.315 J mol^{-1}K^{-1}	
T	Temperature	300 K	
g_{K_k}	Specific ion conductance of potassium	40×10^{3} Ω^{-1}m^{-2}	(Østby et al., 2009)
$g_{Na,k}$	Specific ion conductance of sodium	1.314×10^{3} Ω^{-1}m^{-2}	(Østby et al., 2009)
$g_{NBC,k}$	Specific ion conductance of the NBC cotransporter	7.57×10^{2} Ω^{-1}m^{-2}	(Østby et al., 2009)
$g_{KCC1,k}$	Specific ion conductance of the KCC1 cotransporter	10 Ω^{-1}m^{-2}	(Østby et al., 2009)
$g_{NKCC1,k}$	Specific ion conductance of the NKCC1 cotransporter	55.4 Ω^{-1}m^{-2}	(Østby et al., 2009)
$J_{NaK,max}$	Maximum flux through the NaKATPase pump	1.42×10^{-3} µM ms^{-1}	(Østby et al., 2009)
$G_{BK,k}$	Potassium conductance of the BK channel	4.3×10^{3} pS	(Gonzalez-Fernandez and Ermentrout, 1994)
C_{input}	Block function to switch the channel on and off	0 ; 1 [-]	
$K_{Na,k}$	Michaelis-Menten constant	10^{4} µM	
$K_{K,s}$	Michaelis-Menten constant	1.5×10^{3} µM	
C_{unit}	Unit converting factor	10^{3}	M.E.

Specific ion conductance of the BK channel (Ω^{-1}m^{-2}):

$$g_{BK,k} = \frac{G_{BK,k}\times10^{-12}}{A_k} = 1.16\times10^{3}\ \Omega^{-1}\text{m}^{-2} \tag{A.23}$$

Additional Equations

SYNAPTIC CLEFT

Cl^- concentration (times the SC volume-area ratio R_s; in µM m):

$$N_{Cl,s} = N_{Na,s} + N_{K,s} - N_{HCO_{3,s}}\,; \quad [Cl^-]_s = \frac{N_{Cl,s}}{R_s} \tag{A.24}$$

ASTROCYTE

Membrane voltage of the astrocyte (V):

$$v_k = \frac{g_{Na,k}E_{Na,k} + g_{K,k}E_{K,k} + g_{Cl,k}E_{Cl,k} + g_{NBC,k}E_{NBC,k} + g_{BK,k}w_kE_{BK,k} - J_{NaK,k}FC_{unit}}{g_{Na,k} + g_{K,k} + g_{Cl,k} + g_{NBC,k} + g_{BK,k}w_k} \tag{A.25}$$

Nernst potential for the potassium channel (V):

$$E_{K,k} = \frac{R_{gas}T}{z_K F} \ln\left(\frac{[K^+]_s}{[K^+]_k}\right) \tag{A.26}$$

Nernst potential for the sodium channel (V):

$$E_{Na,k} = \frac{R_{gas}T}{z_{Na} F} \ln\left(\frac{[Na^+]_s}{[Na^+]_k}\right) \tag{A.27}$$

Nernst potential for the chloride channel (V):

$$E_{Cl,k} = \frac{R_{gas}T}{z_{Cl} F} \ln\left(\frac{[Cl^-]_s}{[Cl^-]_k}\right) \tag{A.28}$$

Nernst potential for the NBC channel (V):

$$E_{NBC,k} = \frac{R_{gas}T}{z_{NBC} F} \ln\left(\frac{[Na^+]_s {HCO_3}_{,s}^2}{[Na^+]_k {HCO_3}_{,k}^2}\right) \tag{A.29}$$

Nernst potential for the BK channel (V):

$$E_{BK,k} = \frac{R_{gas}T}{z_K F} \ln\left(\frac{[K^+]_p}{[K^+]_k}\right) \tag{A.30}$$

Equilibrium state BK-channel (-):

$$w_\infty = 0.5\left(1 + \tanh\left(\frac{v_k + v_6}{v_4}\right)\right) \tag{A.31}$$

Time constant associated with the opening of BK channels (s^{-1}):

$$\phi_w = \psi_w \cosh\left(\frac{v_k + v_6}{2v_4}\right) \tag{A.32}$$

$g_{Cl,k}$	Specific ion conductance of chloride	0.879 $\Omega^{-1}m^{-2}$	(Østby et al., 2009)
z_K	Valence of a potassium ion	1	
z_{Na}	Valence of a sodium ion	1	
z_{Cl}	Valence of a chloride ion	-1	
z_{NBC}	Effective valence of the NBC cotransporter complex	-1	
v_6	Voltage associated with the opening of half the population	0.022 V	(Gonzalez-Fernandez and Ermentrout, 1994)
v_4	A measure of the spread of the distribution of the open probability of the BK channel	0.0145 V	(Gonzalez-Fernandez and Ermentrout, 1994)
ψ_w	A characteristic time for the open probability of the BK channel	2.664 s^{-1}	(Gonzalez-Fernandez and Ermentrout, 1994)

A.1.1 *The Smooth Muscle Cell and Endothelial Cell Model*

Conservation Equations

SMOOTH MUSCLE CELL

Cytosolic $[Ca^{2+}]$ in the smooth muscle cell (in μM):

$$\begin{aligned}\frac{d[Ca^{2+}]_i}{dt} &= J_{IP_3,i} - J_{upt,i} + J_{CICR,i} - J_{extr,i} + J_{leak,i} \cdots \\ &-J_{VOCC,i} + J_{Na/Ca,i} + 0.1J_{stretch,i} + J^{SMC-EC}_{Ca^{2+}-coupling_i}\end{aligned} \tag{A.33}$$

$[Ca^{2+}]$ in the sarcoplasmic reticulum of the smooth muscle cell (in μM):

$$\frac{d[\widehat{Ca^{2+}}]_i}{dt} = J_{upt,i} - J_{CICR,i} - J_{leak,i} \tag{A.34}$$

Membrane potential of the smooth muscle cell (in mV):

$$\begin{aligned}\frac{dv_i}{dt} = \gamma_i(&-J_{Na/K,i} - J_{Cl,i} - 2J_{VOCC,i} - J_{Na/Ca,i} - J_{K,i} \cdots \\ &-J_{stretch,i} - J_{KIR,i}) + V^{SMC-EC}_{coupling_i}\end{aligned} \tag{A.35}$$

Open state probability of calcium-activated potassium channels (dim.less):

$$\frac{dw_i}{dt} = \lambda_i\,(K_{act_i} - w_i) \tag{A.36}$$

IP_3 concentration om the smooth muscle cell (in μM):

$$\frac{d[IP_3]_i}{dt} = J^{\text{SMC-EC}}_{IP_3\text{-coupling},i} - J_{\text{degr},i} \tag{A.37}$$

K^+ concentration in the smooth muscle cell (in μM):

$$\frac{d[K^+]_i}{dt} = J_{Na/K,i} - J_{KIR,i} - J_{K,i} \tag{A.38}$$

γ_i	Change in membrane potential by a scaling factor	1970 mV μM^{-1}	(Koenigsberger et al., 2006)
λ_i	Rate constant for opening	45.0 s^{-1}	(Koenigsberger et al., 2006)

ENDOTHELIAL CELL

Cytosolic Ca^{2+} concentration in the endothelial cell (in μM):

$$\begin{aligned}\frac{d[Ca^{2+}]_j}{dt} &= J_{IP_3,j} - J_{upt,j} + J_{CICR,j} - J_{extr,j} \dots \\ &+ J_{leak,j} + J_{cation_j} + J_{0,j} + J_{stretch,j} - J^{\text{SMC-EC}}_{Ca^{2+}\text{-coupling},j}\end{aligned} \tag{A.39}$$

Ca^{2+} concentration in the endoplasmic reticulum in the endothelial cell (in μM):

$$\frac{d[\widehat{Ca^{2+}}]_j}{dt} = J_{upt,j} - J_{CICR,j} - J_{leak,j} \tag{A.40}$$

Membrane potential of the endothelial cell (in mV):

$$\frac{dv_j}{dt} = -\frac{1}{C_{m,j}}(J_{K,j} + J_{R,j}) + V^{\text{SMC-EC}}_{\text{coupling},j} \tag{A.41}$$

IP_3 concentration of the endothelial cell (in μM):

$$\frac{d[IP_3]_j}{dt} = J_{EC,IP_3} - J_{degr,j} - J^{SMC-EC}_{IP_3-coupling_j} \tag{A.42}$$

$C_{m,j}$	Membrane capacitance	25.8 pF	(Koenigsberger et al., 2006)
J_{EC,IP_3}	PLC / IP_3 production rate	0.18 or 0.4 $\mu M\ s^{-1}$	(Koenigsberger et al., 2006)
$J_{0,j}$	Constant Ca^{2+} leak term (influx)	0.029 $\mu M\ s^{-1}$	(Koenigsberger et al., 2006)

Fluxes

SMOOTH MUSCLE CELL

Release of calcium from IP_3 sensitive stores in the SMC (in $\mu M\ s^{-1}$):

$$J_{IP_3,i} = F_i \frac{[IP_3]_i^2}{K_{ri}^2 + [IP_3]_i^2} \tag{A.43}$$

F_i	Maximal rate of activation-dependent calcium influx	0.23 $\mu M\ s^{-1}$	(Koenigsberger et al., 2006)
K_{ri}	Half-saturation constant for agonist-dependent calcium entry	1 μM	(Koenigsberger et al., 2006)

Uptake of calcium into the sarcoplasmic reticulum (in $\mu M\ s^{-1}$):

$$J_{upt,i} = B_i \frac{{[Ca^{2+}]_i}^2}{c_{bi}^2 + {[Ca^{2+}]_i}^2} \tag{A.44}$$

B_i	SR uptake rate constant	2.025 $\mu M\ s^{-1}$	(Koenigsberger et al., 2006)
c_{bi}	Half-point of the SR ATPase activation sigmoidal	1.0 μM	(Koenigsberger et al., 2006)

Calcium-induced calcium release (CICR; in $\mu M\ s^{-1}$):

$$J_{CICR,i} = C_i \frac{{[\widehat{Ca^{2+}}]_i}^2}{s_{ci}^2 + {[\widehat{Ca^{2+}}]_i}^2} \frac{{[Ca^{2+}]_i}^4}{c_{ci}^4 + {[Ca^{2+}]_i}^4} \tag{A.45}$$

C_i	CICR rate constant	55 μM s^{-1}	(Koenigsberger et al., 2006)
s_{ci}	Half-point of the CICR Ca^{2+} efflux sigmoidal	2.0 μM	(Koenigsberger et al., 2006)
c_{ci}	Half-point of the CICR activation sigmoidal	0.9 μM	(Koenigsberger et al., 2006)

Calcium extrusion by Ca^{2+}-ATPase pumps (in μM s^{-1}):

$$J_{extr,i} = D_i[Ca^{2+}]_i \left(1 + \frac{v_i - v_d}{R_{di}}\right) \tag{A.46}$$

D_i	Rate constant for Ca^{2+} extrusion by the ATPase pump	0.24 s^{-1}	(Koenigsberger et al., 2006)
v_d	Intercept of voltage dependence of extrusion ATPase	-100.0 mV	(Koenigsberger et al., 2006)
R_{di}	Slope of voltage dependence of extrusion ATPase.	250.0 mV	(Koenigsberger et al., 2006)

Leak current from the SR (in μM s^{-1}):

$$J_{leak,i} = L_i[\widehat{Ca^{2+}}]_i \tag{A.47}$$

L_i	Leak from SR rate constant	0.025 s^{-1}	(Koenigsberger et al., 2006)

Calcium influx through VOCCs (in μM s^{-1}):

$$J_{VOCC,i} = G_{Ca,i} \frac{v_i - v_{Ca_1,i}}{1 + \exp(-[(v_i - v_{Ca_2,i})/R_{Ca,i}])} \tag{A.48}$$

$G_{Ca,i}$	Whole-cell conductance for VOCCs	1.29×10^{-3} $\mu M\ mV^{-1}s^{-1}$	(Koenigsberger et al., 2006)
$\nu_{Ca_1,i}$	Reversal potential for VOCCs	100.0 mV	(Koenigsberger et al., 2006)
$\nu_{Ca_2,i}$	Half-point of the VOCC activation sigmoidal	-24.0 mV	(Koenigsberger et al., 2006)
$R_{Ca,i}$	Maximum slope of the VOCC activation sigmoidal	8.5 mV	(Koenigsberger et al., 2006)

Flux of calcium exchanging with sodium in the Na^+Ca^{2+} exchange (in $\mu M\ s^{-1}$):

$$J_{Na/Ca,i} = G_{Na/Ca,i}\frac{[Ca^{2+}]_i}{[Ca^{2+}]_i + c_{Na/Ca,i}}\left(\nu_i - \nu_{Na/Ca,i}\right) \tag{A.49}$$

$G_{Na/Ca,i}$	Whole-cell conductance for Na^+/Ca^{2+} exchange	3.16×10^{-3} $\mu M\ mV^{-1}s^{-1}$	(Koenigsberger et al., 2006)
$c_{Na/Ca,i}$	Half-point for activation of Na^+/Ca^{2+} exchange by Ca^{2+}	0.5 μM	(Koenigsberger et al., 2006)
$\nu_{Na/Ca,i}$	Reversal potential for the Na^+/Ca^{2+} exchanger	-30.0 mV	(Koenigsberger et al., 2006)

Calcium flux through the stretch-activated channels in the SMC (in $\mu M\ s^{-1}$):

$$J_{stretch,i} = \frac{G_{stretch}}{1+\exp\left(-\alpha_{stretch}\left(\frac{\Delta p R}{h} - \sigma_0\right)\right)}\left(\nu_i - E_{SAC}\right) \tag{A.50}$$

$G_{stretch}$	Whole cell conductance for SACs	6.1×10^{-3} $\mu M\ mV^{-1}s^{-1}$	(Koenigsberger et al., 2006)
$\alpha_{stretch}$	Slope of stress dependence of the SAC activation sigmoidal	7.4×10^{-3} $mmHg^{-1}$	(Koenigsberger et al., 2006)
Δp	Pressure difference	30 mmHg	ME
σ_0	Half-point of the SAC activation sigmoidal	500 mmHg	(Koenigsberger et al., 2006)
E_{SAC}	Reversal potential for SACs	-18 mV	(Koenigsberger et al., 2006)

Flux through the sodium potassium pump (in $\mu M\ s^{-1}$):

$$J_{Na/K,i} = F_{Na/K,i} \tag{A.51}$$

$F_{Na/K,i}$	Rate of the potassium influx by the sodium potassium pump	4.32×10^{-2} $\mu M\ s^{-1}$	(Koenigsberger et al., 2006)

Chloride flux through the chloride channel (in $\mu M\ s^{-1}$):

$$J_{Cl,i} = G_{Cl,i}\left(v_i - v_{Cl,i}\right) \tag{A.52}$$

$G_{Cl,i}$	Whole-cell conductance for Cl^- current	1.34×10^{-3} $\mu M\ mV^{-1}s^{-1}$	(Koenigsberger et al., 2006)
$v_{Cl,i}$	Reversal potential for Cl^- channels.	-25.0 mV	(Koenigsberger et al., 2006)

Potassium flux through potassium channel (in $\mu M\ s^{-1}$):

$$J_{K,i} = G_{K,i} w_i \left(v_i - v_{K_i}\right) \tag{A.53}$$

$G_{K,i}$	Whole-cell conductance for K^+ efflux.	4.46×10^{-3} $\mu M\ mV^{-1}s^{-1}$	(Koenigsberger et al., 2006)
v_{K_i}	Nernst potential	-94 mV	(Koenigsberger et al., 2006)

Flux through KIR channels in the SMC (in $\mu M\ s^{-1}$):

$$J_{KIR,i} = \frac{F_{KIR,i}\, g_{KIR,i}}{\gamma_i}\left(v_i - v_{KIR,i}\right) \tag{A.54}$$

$F_{KIR,i}$	Scaling factor of potassium efflux through the KIR channel	750 mV μM^{-1}	(Gonzalez-Fernandez and Ermentrout, 1994)

IP_3 degradation (in $\mu M\ s^{-1}$):

$$J_{degr,i} = k_{d,i}[IP_3]_i \tag{A.55}$$

$k_{d,i}$	Rate constant of IP_3 degradation	0.1 s^{-1}	(Koenigsberger et al., 2006)

ENDOTHELIAL CELL

Release of calcium from IP_3-sensitive stores in the EC (in $\mu M\ s^{-1}$):

$$J_{IP_3,j} = F_j \frac{[IP_3]_j^2}{K_{rj}^2 + [IP_3]_j^2} \tag{A.56}$$

F_j	Maximal rate of activation-dependent calcium influx	0.23 $\mu M\ s^{-1}$	(Koenigsberger et al., 2006)
K_{rj}	Half-saturation constant for agonist-dependent calcium entry	1 μM	(Koenigsberger et al., 2006)

Uptake of calcium into the endoplasmic reticulum (in $\mu M\ s^{-1}$):

$$J_{upt,j} = B_j \frac{[Ca^{2+}]_j{}^2}{c_{bj}^2 + [Ca^{2+}]_j{}^2} \tag{A.57}$$

B_j	ER uptake rate constant	0.5 $\mu M\ s^{-1}$	(Koenigsberger et al., 2006)
c_{bj}	Half-point of the SR ATPase activation sigmoidal	1.0 μM	(Koenigsberger et al., 2006)

Calcium-induced calcium release (CICR; in $\mu M\ s^{-1}$):

$$J_{CICR,j} = C_j \frac{[\widehat{Ca^{2+}}]_j{}^2}{s_{cj}^2 + [\widehat{Ca^{2+}}]_j{}^2} \frac{[Ca^{2+}]_j{}^4}{c_{cj}^4 + [Ca^{2+}]_j{}^4} \tag{A.58}$$

C_j	CICR rate constant	5 $\mu M\ s^{-1}$	(Koenigsberger et al., 2006)
s_{cj}	Half-point of the CICR Ca^{2+} efflux sigmoidal	2.0 μM	(Koenigsberger et al., 2006)
c_{cj}	Half-point of the CICR activation sigmoidal	0.9 μM	(Koenigsberger et al., 2006)

Calcium extrusion by Ca^{2+}-ATPase pumps (in $\mu M\ s^{-1}$):

$$J_{extr,j} = D_j[Ca^{2+}]_j \tag{A.59}$$

D_j	Rate constant for Ca^{2+} extrusion by the ATPase pump	$0.24\ s^{-1}$	(Koenigsberger et al., 2005)

Calcium flux through the stretch-activated channels in the EC (in $\mu M\ s^{-1}$):

$$J_{stretch,j} = \frac{G_{stretch}}{1 + e^{-\alpha_{stretch}(\sigma - \sigma_0)}}(v_j - E_{SAC}) = \frac{G_{stretch}}{1 + e^{-\alpha_{stretch}(\frac{\Delta p R}{h} - \sigma_0)}}(v_j - E_{SAC}) \tag{A.60}$$

Leak current from the ER (in $\mu M\ s^{-1}$):

$$J_{leak,j} = L_j[\widehat{Ca^{2+}}]_j \tag{A.61}$$

L_j	Rate constant for Ca^{2+} leak from the ER	$0.025\ s^{-1}$	(Koenigsberger et al., 2006)

Calcium influx through nonselective cation channels (in $\mu M\ s^{-1}$):

$$J_{cation_j} = G_{cat,j}(E_{Ca,j} - v_j)\frac{1}{2}\left(1 + \tanh\left(\frac{\log_{10}[Ca^{2+}]_j - m3_{cat,j}}{m4_{cat,j}}\right)\right) \tag{A.62}$$

$G_{cat,j}$	Whole-cell cation channel conductivity	6.6×10^{-4} $\mu M\ mV^{-1}s^{-1}$	(Koenigsberger et al., 2006)
$E_{Ca,j}$	Ca^{2+} equilibrium potential	50 mV	(Koenigsberger et al., 2006)
$m3_{cat,j}$	Model constant	-0.18 μM	(Koenigsberger et al., 2006)
$m4_{cat,j}$	Model constant	0.37 μM	(Koenigsberger et al., 2006)

Potassium efflux through the $J_{BK_{Caj}}$ channel and the $J_{SK_{Caj}}$ channel (in $\mu M\ s^{-1}$):

$$J_{K,j} = G_{totj}(v_j - v_{Kj})\left(J_{BK_{Caj}} + J_{SK_{Caj}}\right) \tag{A.63}$$

G_{totj}	Total potassium channel conductivity.	6927 pS	(Koenigsberger et al., 2006)
v_{Kj}	K^+ equilibrium potential	-80.0 mV	(Koenigsberger et al., 2006)

Potassium efflux through the $J_{BK_{Caj}}$ channel (in $\mu M\ s^{-1}$):

$$J_{BK_{Caj}} = 0.2\left(1+\tanh\left(\frac{(\log_{10}[Ca^{2+}]_j - c)(v_j - b_j) - a_{1j}}{m_{3bj}(v_j + a_{2j}(\log_{10}[Ca^{2+}]_j - c) - b_j)^2 + m_{4bj}}\right)\right) \tag{A.64}$$

Potassium efflux through the $J_{SK_{Caj}}$ channel (in $\mu M\ s^{-1}$):

$$J_{SK_{Caj}} = 0.3\left(1+\tanh\left(\frac{\log_{10}[Ca^{2+}]_j - m_{3sj}}{m_{4sj}}\right)\right) \tag{A.65}$$

c	Model constant, further explanation see reference	-0.4 μM	(Koenigsberger et al., 2006)
b_j	Model constant, further explanation see reference	-80.8 mV	(Koenigsberger et al., 2006)
a_{1j}	Model constant, further explanation see reference	53.3 μM mV	(Koenigsberger et al., 2006)
a_{2j}	Model constant, further explanation see reference	53.3 mV μM^{-1}	(Koenigsberger et al., 2006)
m_{3bj}	Model constant, further explanation see reference	1.32×10^{-3} μM mV^{-1}	(Koenigsberger et al., 2006)
m_{4bj}	Model constant, further explanation see reference	0.30 μM mV	(Koenigsberger et al., 2006)
m_{3sj}	Model constant, further explanation see reference	-0.28 μM	(Koenigsberger et al., 2006)
m_{4sj}	Model constant, further explanation see reference	0.389 μM	(Koenigsberger et al., 2006)

Residual current regrouping chloride and sodium current flux (in $\mu M\ s^{-1}$):

$$J_{R,j} = G_{R_j}(v_j - v_{rest,j}) \tag{A.66}$$

$G_{R,j}$	Residual current conductivity	955 pS	(Koenigsberger et al., 2006)
$v_{rest,j}$	Membrane resting potential	-31.1 mV	(Koenigsberger et al., 2006)

IP_3 degradation (in $\mu M\ s^{-1}$):

$$J_{degr,j} = k_{d,j}[IP_3]_j \tag{A.67}$$

$k_{d,j}$	Rate constant of IP_3 degradation	$0.1\ s^{-1}$	(Koenigsberger et al., 2006)

Coupling

Heterocellular electrical coupling between SMCs and ECs (in $mV\ s^{-1}$):

$$V^{SMC-EC}_{coupling_i} = -G_{coup}(v_i - v_j) \tag{A.68}$$

Heterocellular IP_3 coupling between SMCs and ECs (in $\mu M\ s^{-1}$):

$$J^{SMC-EC}_{IP_3-coupling_i} = -P_{IP_3}([IP_3]_i - [IP_3]_j) \tag{A.69}$$

Calcium coupling with EC (in $\mu M\ s^{-1}$):

$$J^{SMC-EC}_{Ca^{2+}-coupling_i} = -P_{Ca^{2+}}([Ca^{2+}]_i - [Ca^{2+}]_j) \tag{A.70}$$

G_{coup}	Heterocellular electrical coupling coefficient	$0.5\ s^{-1}$	ME
P_{IP_3}	Heterocellular IP_3 coupling coefficient	$0.05\ s^{-1}$	(Koenigsberger et al., 2006)
$P_{Ca^{2+}}$	Heterocellular $P_{Ca^{2+}}$ coupling coefficient	$0.05\ s^{-1}$	(Koenigsberger et al., 2006)

Additional Equations

Equilibrium distribution of open channel states for the voltage and calcium activated potassium channels (dimensionless):

$$K_{act_i} = \frac{\left([Ca^{2+}]_i + c_{wi}\right)^2}{\left([Ca^{2+}]_i + c_{wi}\right)^2 + \beta_i \exp(-([v_i - v_{Ca_{3i}}]/R_{Ki}))} \tag{A.71}$$

Nernst potential of the KIR channel in the SMC (in mV):

$$v_{KIR,i} = z_1 [K^+]_p - z_2 \tag{A.72}$$

Conductance of KIR channel (in µM mV^{-1} s^{-1}):

$$g_{KIR,i} = \exp(z_5 v_i + z_3 [K^+]_p - z_4) \tag{A.73}$$

c_{wi}	Translation factor for Ca^{2+} dependence of K_{Ca} channel activation sigmoidal.	0.0 µM	(Koenigsberger et al., 2006)
β_i	Translation factor for membrane potential dependence of K_{Ca} channel activation sigmoidal.	0.13 μM^2	(Koenigsberger et al., 2006)
$v_{Ca_{3i}}$	Half-point for the K_{Ca} channel activation sigmoidal.	-27 mV	(Koenigsberger et al., 2006)
R_{Ki}	Maximum slope of the K_{Ca} activation sigmoidal.	12 mV	(Koenigsberger et al., 2006)
z_1	Model estimation for membrane voltage KIR channel	4.5×10^3 mV μM^{-1}	(Filosa et al., 2006)
z_2	Model estimation for membrane voltage KIR channel	112 mV	(Filosa et al., 2006)
z_3	Model estimation for the KIR channel conductance	4.2×10^2 $mV^{-1}s^{-1}$	(Filosa et al., 2006)
z_4	Model estimation for the KIR channel conductance	12.6 µM $mV^{-1}s^{-1}$	(Filosa et al., 2006)
z_5	Model estimation for the KIR channel conductance	-7.4×10^{-2} µM $mV^{-2}s^{-1}$	(Filosa et al., 2006)

A.1.2 *The Contraction Model*

Fraction of free phosphorylated cross-bridges (dimensionless):

$$\frac{d[Mp]}{dt} = K_4[AMp] + K_1[M] - (K_2 + K_3)[Mp] \tag{A.74}$$

Fraction of attached phosphorylated cross-bridges (dimensionless):

$$\frac{d[AMp]}{dt} = K_3[Mp] + K_6[AM] - (K_4 + K_5)[AMp] \tag{A.75}$$

Fraction of attached dephosphorylated cross-bridges (dimensionless):

$$\frac{d[AM]}{dt} = K_5[AMp] - (K_7 + K_6)[AM] \tag{A.76}$$

Fraction of free non-phosphorylated cross-bridges (dimensionless):

$$[M] = 1 - [AM] - [AMp] - [Mp] \tag{A.77}$$

Rate constants that represent phosphorylation of M to Mp and of AM to AMp by the active myosin light chain kinase (MLCK), respectively (in s^{-1}):

$$K_1 = K_6 = \gamma_{cross}[Ca^{2+}]_i^{\,n_{cross}} \tag{A.78}$$

A.1.3 *The Mechanical Model*

Wall thickness of the vessel (in μm):

$$h = 0.1R \tag{A.79}$$

Fraction of attached myosin cross-bridges (dimensionless):

$$F_r = [AM_p] + [AM] \tag{A.80}$$

K_2	Rate constant for dephosphorylation (of Mp to M) by myosin light-chain phosphatase (MLCP)	0.5 s^{-1}	(Hai and Murphy, 1989)
K_3	Rate constants representing the attachment/detachment of fast cycling phosphorylated cross-bridges	0.4 s^{-1}	(Hai and Murphy, 1989)
K_4	Rate constants representing the attachment/detachment of fast cycling phosphorylated cross-bridges	0.1 s^{-1}	(Hai and Murphy, 1989)
K_5	Rate constant for dephosphorylation (of AMp to AM) by myosin light-chain phosphatase (MLCP)	0.5 s^{-1}	(Hai and Murphy, 1989)
K_7	Rate constant for latch-bridge detachment	0.1 s^{-1}	(Hai and Murphy, 1989)
γ_{cross}	Sensitivity of the contractile apparatus to calcium	17 μM^{-3} s^{-1}	(Koenigsberger et al., 2005)
n_{cross}	Fraction constant of the phosphorylation cross-bridge	3 [–]	(Koenigsberger et al., 2005)

η	viscosity	10^4 Pa s	(Koenigsberger et al., 2006)
$R_{0_{pas}}$	Radius of the vessel when passive and no stress is applied	20 µm	ME
P_T	Transmural pressure	4×10^3 Pa	ME
E_{pas}	Young's modulus for the passive vessel	66×10^3 Pa	(Gore and Davis, 1985)
E_{act}	Young's modulus for the active vessel	233×10^3 Pa	(Gore and Davis, 1985)
α_r	Scaling factor initial radius	0.6	(Gore and Davis, 1985)

Vessel radius (in m):

$$\frac{dR}{dt} = \frac{R_{0_{pas}}}{\eta}\left(\frac{RP_T}{h} - E(F_r)\frac{R - R_0(F_r)}{R_0(F_r)}\right) \tag{A.81}$$

with:

$$E(F_r) = E_{pas} + F_r\left(E_{act} - E_{pas}\right) \tag{A.82}$$

$$R_0(F_r) = R_{0_{pas}} + F_r(\alpha_r - 1)R_{0_{pas}} \tag{A.83}$$

A.2 MODEL EQUATIONS AND PARAMETERS OF THE NO SIGNALLING PATHWAY

Global Constants

F	Faraday's constant	96500 C mol^{-1}	
T	temperature	300 K	
R_{gas}	gas constant	8.315 J $mol^{-1}K^{-1}$	
$D_{c,NO}$	NO diffusion coefficient	3300 $\mu m^2 s^{-1}$	(Malinski et al., 1993)

Model input

Glu concentration in the synaptic cleft (µM):

$$[Glu]_{sc}(t) = [Glu]_{max}\,(0.5\tanh(t - t_0) - 0.5\tanh(t - t_2)) \tag{A.84}$$

Neuron

Differential equations

Rate of change of cytosolic Ca^{2+} concentration (µM s^{-1}):

$$\frac{d[Ca^{2+}]_n}{dt} = \frac{I_{Ca,tot}/(2FV_{spine}) - \kappa_{ex}([Ca^{2+}]_n - [Ca^{2+}]_{rest})}{1 + \lambda_{buf}} \tag{A.85}$$

Rate of change of activated nNOS (µM s^{-1}):

$$\frac{d[nNOS_{act}]_n}{dt} = \frac{V_{max,nNOS}[CaM]_n}{K_{m,nNOS} + [CaM]_n} - \mu_{deact,n}[nNOS_{act}]_n \tag{A.86}$$

Rate of change of neuronal NO (µM s^{-1}):

$$\frac{d[NO]_n}{dt} = p_{NO,n} - c_{NO,n} + d_{NO,n} \tag{A.87}$$

Algebraic equations

Fraction of open NR2A NMDA receptors (dim.less):

$$w_{NR2,A} = \frac{[Glu]_{sc}}{K_{m,A} + [Glu]_{sc}} \tag{A.88}$$

Fraction of open NR2B NMDA receptors (dim.less):

$$w_{NR2,B} = \frac{[Glu]_{sc}}{K_{m,B} + [Glu]_{sc}} \tag{A.89}$$

Inward calcium current per open NMDA receptor (fA):

$$I_{Ca} = \frac{4\nu_n G_M (P_{Ca}/P_M)([Ca^{2+}]_{ex}/[M])}{1 + \exp(\alpha_\nu(\nu_n + \beta_\nu))} \frac{\exp(2\nu_n F/(R_{gas}T))}{1 - \exp(2\nu_n F/(R_{gas}T))} \tag{A.90}$$

Total inward calcium current for all open NMDA receptors per synapse (fA):

$$I_{Ca,tot} = (n_{NR2,A} w_{NR2,A} + n_{NR2,B} w_{NR2,B}) I_{Ca} \tag{A.91}$$

Sum of all the states of bound calcium with respect to free calcium (dim.less):

$$\phi_{mc} = 1 + Q_1[Ca^{2+}]_n + Q_1Q_2[Ca^{2+}]_n^2 + Q_1Q_2Q_3[Ca^{2+}]_n^3 + Q_1Q_2Q_3Q_4[Ca^{2+}]_n^4 \tag{A.92}$$

Number of calcium ions bound per calmodulin (dim.less):

$$m_c = \frac{[Ca^{2+}]_n}{\phi_{mc}} \frac{d\phi_{mc}}{d[Ca^{2+}]_n} \tag{A.93}$$

Calcium-calmodulin complex concentration (μM):

$$[CaM]_n = \frac{[Ca^{2+}]_n}{m_c} \tag{A.94}$$

NO production flux (μM s^{-1}):

$$p_{NO,n} = V_{max,NO,n}[nNOS_{act}]_n \frac{[O_2]_n}{K_{m,O2,n} + [O_2]_n} \frac{[L\text{-}Arg]_n}{K_{m,L\text{-}Arg,n} + [L\text{-}Arg]_n} \tag{A.95}$$

NO consumption flux ($\mu M\ s^{-1}$):

$$c_{NO,n} = k_{O2,n}[NO]_n^2[O_2]_n \tag{A.96}$$

NO diffusive flux ($\mu M\ s^{-1}$):

$$d_{NO,n} = \frac{[NO]_k - [NO]_n}{\tau_{nk}} \tag{A.97}$$

Time for NO to diffuse between the centres of the NE and the AC (s):

$$\tau_{nk} = \frac{\chi_{nk}^2}{2D_{c,NO}} \tag{A.98}$$

Astrocyte

Differential equations

Rate of change of astrocytic NO concentration ($\mu M\ s^{-1}$):

$$\frac{d[NO]_k}{dt} = p_{NO,k} - c_{NO,k} + d_{NO,k} \tag{A.99}$$

Algebraic equations

NO production flux ($\mu M\ s^{-1}$):

$$p_{NO,k} = 0 \tag{A.100}$$

NO consumption flux ($\mu M\ s^{-1}$):

$$c_{NO,k} = k_{O2,k}[NO]_k^2[O_2]_k \tag{A.101}$$

NO diffusive flux ($\mu M\ s^{-1}$):

$$d_{NO,k} = \frac{[NO]_n - [NO]_k}{\tau_{nk}} + \frac{[NO]_i - [NO]_k}{\tau_{ki}} \tag{A.102}$$

$[Glu]_{max}$	maximum glutamate concentration	1846 µM	(Santucci and Raghavachari, 2008)
t_0	start time for Glu pulse	var.	see (Dormanns et al., 2014)
t_2	end time for Glu pulse	var.	see (Dormanns et al., 2014)
V_{spine}	dentritic spine volume	8×10^{-8} nL	(Santucci and Raghavachari, 2008)
κ_{ex}	decay rate constant of internal Ca^{2+} concentration	1.6×10^{3} s^{-1}	(Santucci and Raghavachari, 2008)
$[Ca^{2+}]_{rest}$	resting internal calcium concentration	0.1 µM	(Santucci and Raghavachari, 2008)
λ_{buf}	buffer capacity	20 (dim.less)	(Santucci and Raghavachari, 2008)
$V_{max,nNOS}$	maximum nNOS activation rate	25×10^{-3} µM	M.E.
$K_{m,nNOS}$	Michaelis constant	9.27×10^{-2}	(Hayashi et al., 1999)
$\mu_{deact,n}$	rate constant at which nNOS is deactivated	0.0167 s^{-1}	(Comerford et al., 2008)
$K_{m,A}$	Michaelis constant	650 µM	(Santucci and Raghavachari, 2008)
$K_{m,B}$	Michaelis constant	2800 µM	(Santucci and Raghavachari, 2008)
ν_n	neuronal membrane potential	-0.04 V	M.E.
G_M	conductance of NMDA receptor	4.6×10^{4} fS	(Santucci and Raghavachari, 2008)
P_{Ca}/P_M	ratio of NMDA receptor permeability to Ca^{2+} to permeability to monovalent ions	3.6 (dim.less)	(Santucci and Raghavachari, 2008)
$[Ca^{2+}]_{ex}$	external calcium concentration	2×10^{3} µM	(Santucci and Raghavachari, 2008)
$[M]$	concentration of monovalent ions	1.3×10^{5} µM	(Santucci and Raghavachari, 2008)
α_ν	voltage-dependent Mg^{2+} block parameter	-80 V^{-1}	(Santucci and Raghavachari, 2008)
β_ν	voltage-dependent Mg^{2+} block parameter	0.02 V	(Santucci and Raghavachari, 2008)
$n_{NR2,A}$	average number of NR2A NMDA receptors	0.63 (dim.less)	(Santucci and Raghavachari, 2008)
$n_{NR2,B}$	average number of NR2A NMDA receptors	11 (dim.less)	(Santucci and Raghavachari, 2008)
Q_1	Ca^{2+}-CaM binding constant	1.9×10^{5} μM^{-1}	(Crouch and Klee, 1980)
Q_2	Ca^{2+}-CaM binding constant	2.1×10^{5} μM^{-1}	(Crouch and Klee, 1980)
Q_3	Ca^{2+}-CaM binding constant	0.4×10^{5} μM^{-1}	(Crouch and Klee, 1980)
Q_4	Ca^{2+}-CaM binding constant	0.26×10^{5} μM^{-1}	(Crouch and Klee, 1980)
$V_{max,NO,n}$	maximum catalytic rate of neuronal NO production	4.22 s^{-1}	(Chen and Popel, 2006)
$[O_2]_n$	O_2 concentration in the neuron	200 µM	M.E.
$K_{m,O2,n}$	Michaelis constant for nNOS for O_2	243 µM	(Chen and Popel, 2007)
$[L\text{-}Arg]_n$	L-Arg concentration in the neuron	100 µM	(Chen and Popel, 2007)
$K_{m,L\text{-}Arg,n}$	Michaelis constant for nNOS for L-Arg	1.5 µM	(Chen and Popel, 2006)
$k_{O2,n}$	O_2 reaction rate constant	9.6×10^{-6} μM^{-2} s^{-1}	(Kavdia et al., 2002)
x_{nk}	distance between centres of NE and AC	25 µm	M.E.

Time for NO to diffuse between the centres of the AC and the SMC (s):

$$\tau_{ki} = \frac{x_{ki}^2}{2D_{c,NO}} \tag{A.103}$$

$k_{O2,k}$	O_2 reaction rate constant	$9.6\times10^{-6}\,\mu M^{-2}s^{-1}$	(Kavdia et al., 2002)
x_{ki}	distance between centres of AC and SMC compartments	25 µm	model assumption

Smooth muscle cell

Differential equations

Rate of change of NO concentration in the SMC ($\mu M\ s^{-1}$):

$$\frac{d[NO]_i}{dt} = p_{NO,i} - c_{NO,i} + d_{NO,i} \tag{A.104}$$

Rate of change of fraction of sGC in the basal state (s^{-1}):

$$\frac{dE_b}{dt} = -k_1 E_b [NO]_i + k_{-1} E_{6c} + k_4 E_{5c} \tag{A.105}$$

Rate of change of fraction of sGC in the intermediate form (s^{-1}):

$$\frac{dE_{6c}}{dt} = k_1 E_b [NO]_i - (k_{-1} + k_2) E_{6c} - k_3 E_{6c} [NO]_i \tag{A.106}$$

Rate of change of cGMP concentration ($\mu M\ s^{-1}$):

$$\frac{d[cGMP]_i}{dt} = V_{max,sGC} E_{5c} - \frac{V_{max,pde}[cGMP]_i}{K_{m,pde}[cGMP]_i} \tag{A.107}$$

Algebraic equations

NO production flux ($\mu M\ s^{-1}$):

$$p_{NO,i} = 0 \tag{A.108}$$

NO consumption flux ($\mu M\ s^{-1}$):

$$c_{NO,i} = k_{dno}[NO]_i \tag{A.109}$$

NO diffusive flux ($\mu M\ s^{-1}$):

$$d_{NO,i} = \frac{[NO]_k - [NO]_i}{\tau_{ki}} + \frac{[NO]_j - [NO]_i}{\tau_{ij}} \tag{A.110}$$

sGC kinetics rate constant (s^{-1}):

$$k_4 = C_4[cGMP]_i^{m_4} \tag{A.111}$$

Fraction of sGC in the fully activated form (dim.less):

$$E_{5c} = 1 - E_b - E_{6c} \tag{A.112}$$

Regulatory effect of cGMP on myosin dephosphorylation (dim.less):

$$R_{cGMP} = \frac{[cGMP]_i^2}{K_{m,mlcp}^2 + [cGMP]_i^2} \tag{A.113}$$

Rate constants for dephosphorylation (s^{-1}), see (Dormanns et al., 2014):

$$K_{2c} = K_{5c} = \delta_i \left(k_{mlpc,b} + k_{mlpc,c} R_{cGMP}\right) \tag{A.114}$$

Equilibrium distribution of open channel states for the BK channel (dim.less), see (Dormanns et al., 2014):

$$K_{act,i} = \frac{([Ca^{2+}]_i + c_{w,i})^2}{([Ca^{2+}]_i + c_{w,i})^2 + \beta_i \exp(\nu_{Ca3,i} - \nu_i/R_{K,i})} \tag{A.115}$$

Translation factor, regulatory effect of cGMP on the BK channel open probability (μM):

$$c_{w,i} = \frac{1}{\epsilon_i + \alpha_i \exp(\gamma_i [cGMP]_i)} \tag{A.116}$$

Maximum cGMP production rate ($\mu M\ s^{-1}$):

$$V_{max,pde} = k_{pde}[cGMP]_i \tag{A.117}$$

Time for NO to diffuse between the centres of the SMC and the EC (s):

$$\tau_{ij} = \frac{\chi_{ij}^2}{2D_{c,NO}} \tag{A.118}$$

k_{-1}	sGC kinetics rate constant	100 s^{-1}	(Yang et al., 2005)
k_1	sGC kinetics rate constant	2×10^3 μM^{-1} s^{-1}	(Yang et al., 2005)
k_2	sGC kinetics rate constant	0.1 s^{-1}	(Yang et al., 2005)
k_3	sGC kinetics rate constant	3 μM^{-1} s^{-1}	(Yang et al., 2005)
$V_{max,sGC}$	maximal cGMP production rate	0.8520 μM s^{-1}	(Yang et al., 2005)
$K_{m,pde}$	Michaelis constant	2 μM	(Yang et al., 2005)
k_{dno}	lumped NO consumption rate constant reflecting the activity of various NO scavengers	0.01 s^{-1}	(Yang et al., 2005)
C_4	constant	0.011 s^{-1} μM^{-2}	(Yang et al., 2005)
m_4	cGMP feedback strength	2 (dim.less)	(Yang et al., 2005)
$K_{m,mlcp}$	Hill coefficient	5.5 μM	(Yang et al., 2005)
δ_i	constant to fit data	58.1395 (dim.less)	(Hai and Murphy, 1988), fit
$k_{mlpc,b}$	basal MLC dephosphorylation rate constant	0.0086 s^{-1}	(Yang et al., 2005)
$k_{mlpc,c}$	first-order rate constant for cGMP-regulated MLC dephosphorylation	0.0327 s^{-1}	(Yang et al., 2005)
α_i	constant to fit data	1×10^{14} μM^{-1}	(Stockand and Sansom, 1996), fit
β_i	translation factor for membrane potential dependence of K_{Ca} channel activation sigmoidal	0.13 μM^2	(Koenigsberger et al., 2006)
γ_i	constant to fit data	-3 μM^{-1}	(Stockand and Sansom, 1996), fit
ϵ_i	constant to fit data	1 μM^{-1}	(Stockand and Sansom, 1996), fit
$[Ca^{2+}]_i$	calcium concentration in the SMC cytosol	var.	see (Dormanns et al., 2014)
$v_{Ca3,i}$	half-point for the K_{Ca} channel activation sigmoidal.	-27 mV	(Koenigsberger et al., 2006)
v_i	SMC membrane potential	var.	see (Dormanns et al., 2014)
$R_{K,i}$	Maximum slope of the K_{Ca} activation sigmoidal	12 mV	(Koenigsberger et al., 2006)
k_{pde}	phosphodiesterase rate constant	0.0195 s^{-1}	(Yang et al., 2005)

Endothelial cell

Differential equations

$$\frac{d[eNOS_{act}]_j}{dt} = \gamma_{eNOS}\frac{K_{dis}[Ca^{2+}]_j}{K_{m,eNOS}+[Ca^{2+}]_j} + (1-\gamma_{eNOS})g_{max}F_{wss} - \mu_{deact,j}[eNOS_{act}]_j \tag{A.119}$$

$$\frac{d[NO]_j}{dt} = p_{NO,j} - c_{NO,j} + d_{NO,j} \tag{A.120}$$

Algebraic equations

Fraction of the elastic strain energy stored within the membrane (dim.less):

$$F_{wss} = \frac{1}{1+\alpha_{wss}\exp(-W_{wss})} - \frac{1}{1+\alpha_{wss}} \tag{A.121}$$

Strain energy density (Pa):

$$W_{wss} = W_0\frac{(\tau_{wss}+\sqrt{16\delta_{wss}^2+\tau_{wss}^2}-4\delta_{wss})^2}{\tau_{wss}+\sqrt{16\delta_{wss}^2+\tau_{wss}^2}} \tag{A.122}$$

Wall shear stress (Pa):

$$\tau_{wss} = \frac{r\Delta P}{2L} \tag{A.123}$$

NO production flux ($\mu M\ s^{-1}$):

$$p_{NO,j} = V_{max,NO,j}[eNOS_{act}]_j\frac{[O_2]_j}{K_{m,O2,j}+[O_2]_j}\frac{[L\text{-}Arg]_j}{K_{m,L\text{-}Arg,j}+[L\text{-}Arg]_j} \tag{A.124}$$

NO consumption flux ($\mu M\ s^{-1}$):

$$c_{NO,j} = k_{O2,j}[NO]_j^2[O_2]_j \tag{A.125}$$

NO diffusive flux ($\mu M\ s^{-1}$):

$$d_{NO,j} = \frac{[NO]_i - [NO]_j}{\tau_{ij}} - \frac{4D_{c,NO}[NO]_j}{r^2} \tag{A.126}$$

γ_{eNOS}	relative strength of the Ca^{2+}-dependent pathway for the eNOS activation	0.1 (dim.less)	(Comerford et al., 2008)
$\mu_{deact,j}$	eNOS-caveolin association rate	0.0167 s^{-1}	(Comerford et al., 2008)
K_{dis}	eNOS-caveolin disassociation rate	0.09 $\mu M\ s^{-1}$	(Comerford et al., 2008)
$[Ca^{2+}]_j$	calcium concentration in the EC cytosol	var.	see (Dormanns et al., 2014)
$K_{m,eNOS}$	Michaelis constant	0.45 μM	(Comerford et al., 2008)
g_{max}	maximum wall-shear-stress-induced eNOS activation	0.06 $\mu M\ s^{-1}$	(Comerford et al., 2008)
α_{wss}	zero shear open channel constant	2 (dim.less)	(Comerford et al., 2008)
W_0	shear gating constant	1.4 Pa^{-1}	(Comerford et al., 2008)
δ_{wss}	membrane shear modulus	2.86 Pa	(Comerford et al., 2008)
r	radius of arteriole	var.	see (Dormanns et al., 2014)
$V_{max,NO,j}$	maximum catalytic rate of NO production	1.22 s^{-1}	(Chen and Popel, 2006)
$[O_2]_j$	O_2 concentration in the EC	200 μM	M.E.
$K_{m,O2,j}$	Michaelis constant for eNOS for O_2	7.7 μM	(Chen and Popel, 2006)
$[L\text{-}Arg]_j$	L-Arg concentration in the neuron	100 μM	(Chen and Popel, 2006)
$K_{m,L\text{-}Arg,j}$	Michaelis constant for eNOS for L-Arg	1.5 μM	(Chen and Popel, 2006)
$\Delta P/L$	pressure drop over length of arteriole	9.1×10^{4} Pa m^{-1}	M.E.
$k_{O2,j}$	O_2 reaction rate constant	9.6×10^{-6} $\mu M^{-2}\ s^{-1}$	(Kavdia et al., 2002)

BIBLIOGRAPHY

Abbott, N. J.; Patabendige, A. a. K.; Dolman, D. E. M.; Yusof, S. R. and Begley, D. J. (**2010**): Structure and function of the blood-brain barrier., Neurobiology of disease, Vol. 37, No. 1 pp. 13–25. (Cited on page 4.)

Ackerman, M. J. and Clapham, D. E. (**1997**): Ion channels - basic science and clinical disease, The New England Journal of Medicine, Vol. 336, No. 22 pp. 1575–1586. (Cited on page 4.)

Alderton, W. K.; Cooper, C. E. and Knowles, R. G. (**2001**): Nitric oxide synthases: structure, function and inhibition, The Biochemical Journal, Vol. 357, No. 1 pp. 593–615. (Cited on page 88.)

Allaman, I.; Bélanger, M. and Magistretti, P. J. (**2011**): Astrocyte-neuron metabolic relationships: for better and for worse, Trends in Neurosciences, Vol. 34, No. 2 pp. 76–87. (Cited on page 154.)

Aoi, M. C.; Hu, K.; Lo, M.-T.; Selim, M.; Olufsen, M. S. and Novak, V. (**2012**): Impaired cerebral autoregulation is associated with brain atrophy and worse functional status in chronic ischemic stroke, PloS ONE, Vol. 7, No. 10 p. e46794. (Cited on page 11.)

Attwell, D.; Buchan, A. M.; Charpak, S.; Lauritzen, M.; Macvicar, B. A. and Newman, E. A. (**2010**): Glial and neuronal control of brain blood flow, Nature, Vol. 468, No. 7321 pp. 232–243. (Cited on pages 4, 8, 12, 13, 88, and 118.)

Bai, J. Z. and Lipski, J. (**2014**): Involvement of TRPV4 channels in Abeta40-induced hippocampal cell death and astrocytic Ca2+ signalling, Neuro-Toxicology, Vol. 41 pp. 64–72. (Cited on page 155.)

Barrio, L. C.; Capel, J.; Jarillo, J. A.; Castro, C. and Revilla, A. (**1997**): Species-Specific Voltage-Gating Properties of Connexin-45 Junctions Expressed in Xenopus Oocytes, Biophysical Journal, Vol. 73, No. 2 pp. 757–769. (Cited on pages 56 and 74.)

Bélanger, M.; Allaman, I. and Magistretti, P. J. (**2011**): Brain energy metabolism: Focus on Astrocyte-neuron metabolic cooperation, Cell Metabolism, Vol. 14, No. 6 pp. 724–738. (Cited on page 3.)

Bell, R. D. R. and Zlokovic, B. B. V. (**2009**): Neurovascular mechanisms and blood-brain barrier disorder in Alzheimer's disease, Acta Neuropathologica, Vol. 118, No. 1 pp. 103–113. (Cited on pages 13, 42, and 121.)

Benarroch, E. E. (**2006**): Basic Neurosciences with Clinical Applications, Butterworth-Heinemann. (Cited on pages 30 and 94.)

Bennett, M. R.; Farnell, L. and Gibson, W. G. (**2008**): Origins of blood volume change due to glutamatergic synaptic activity at astrocytes abutting on arteriolar smooth muscle cells, Journal of Theoretical Biology, Vol. 250, No. 1 pp. 172–185. (Cited on pages 31 and 38.)

Berridge, M. J. (**2008**): Smooth muscle cell calcium activation mechanisms, The Journal of Physiology, Vol. 586, No. 21 pp. 5047–5061. (Cited on pages 70, 78, and 85.)

Berridge, M. J. (**2012**): Cell Signalling Biology: Module 2 - Cell signalling pathways, Biochemical Journal, Vol. Module 2, No. Cell signaling pathway pp. 1–130. (Cited on pages 5 and 10.)

Bindschadler, M. and Sneyd, J. (**2001**): A bifurcation analysis of two coupled calcium oscillators, Chaos, Vol. 11, No. 2001 pp. 237–246. (Cited on page 99.)

Bredt, D. S. (**2003**): Nitric oxide signaling specificity – the heart of the problem, Journal of Cell Science, Vol. 116, No. 1 pp. 9–15. (Cited on page 93.)

Briggs, G. E. (**1925**): A Further Note on the Kinetics of Enzyme Action, The Biochemical Journal, Vol. 19, No. 6 pp. 338–339. (Cited on page 18.)

Brown, R. G. and David, T. (**2013**): Numerical techniques for large-scale resistive networks, with application to a model of cerebral autoregulation pp. 1–18. (Cited on pages 124 and 127.)

Buerk, D. G. (**2001**): Can we model nitric oxide biotransport? A survey of mathematical models for a simple diatomic molecule with surprisingly complex biological activities, Annual Review of Biomedical Engineering, Vol. 3 pp. 109–143. (Cited on pages 89 and 114.)

Butler, A. and Nicholsson, R. (**2003**): Life, Death, and Nitric Oxide, Royal Society of Chemistry. (Cited on pages 9, 88, and 114.)

Butler, A. R.; Megson, I. L. and Wright, P. G. (**1998**): Diffusion of nitric oxide and scavenging by blood in the vasculature, Biochimica et Biophysica Acta - General Subjects, Vol. 1425, No. 1 pp. 168–176. (Cited on page 100.)

Calabrese, V.; Mancuso, C.; Calvani, M.; Rizzarelli, E.; Butterfield, D. A. and Stella, A. M. G. (**2007**): Nitric oxide in the central nervous system: neuroprotection versus neurotoxicity, Nature reviews. Neuroscience, Vol. 8, No. 10 pp. 766–775. (Cited on page 89.)

Carmignoto, G. and Gómez-Gonzalo, M. (**2010**): The contribution of astrocyte signalling to neurovascular coupling, Brain Research Reviews, Vol. 63, No. 1-2 pp. 138–48. (Cited on pages 6 and 29.)

Cebral, J.; Lohner, P.; Yim, J. and Burgess, J. (**2001**): Blood flow predictions during neuro-surgery and carotid artery stenting, International Journal of Bioelectromagnetism, Vol. 3, No. 2 pp. 1–12. (Cited on page 41.)

Chander, B. S. and Chakravarthy, V. S. (**2012**): A Computational Model of Neuro-Glio-Vascular Loop Interactions, PLoS ONE, Vol. 7, No. 11 p. e48802. (Cited on page 38.)

Chang, J. C.; Brennan, K. C.; He, D.; Huang, H.; Miura, R. M.; Wilson, P. L. and Wylie, J. J. (**2013**): A mathematical model of the metabolic and perfusion effects on cortical spreading depression, PloS ONE, Vol. 8, No. 8 p. e70469. (Cited on pages 29, 30, 37, 49, and 154.)

Charles, A. C.; Naus, C. C.; Zhu, D.; Kidder, G. M.; Dirksen, E. R. and Sanderson, M. J. (**1992**): Intercellular calcium signaling via gap junctions in glioma cells, Journal of Cellular Biology, Vol. 118, No. 1 pp. 195–201. (Cited on page 75.)

Charles, E. S.; Costantin, J. L.; Naus, C. C. G. and Charles, A. C. (**2002**): Intercellular Calcium Signaling in Astrocytes via ATP Release through Connexin Hemichannels, Journal of Biological Chemistry, Vol. 277, No. 12 pp. 10482–10488. (Cited on page 75.)

Chen, B. R.; Bouchard, M. B.; McCaslin, A. F. H.; Burgess, S. A. and Hillman, E. M. C. (**2011**): High-speed vascular dynamics of the hemodynamic response, Neuroimage, Vol. 54, No. 2 pp. 1021–1030. (Cited on page 65.)

Chen, K. and Popel, A. S. (**2006**): Theoretical analysis of biochemical pathways of nitric oxide release from vascular endothelial cells, Free Radical Biology and Medicine, Vol. 41, No. 4 pp. 668–680. (Cited on pages 88, 91, 93, 96, 97, 114, 181, and 186.)

Chen, K. and Popel, A. S. (**2007**): Theoretical analysis of biochemical pathways of nitric oxide release from vascular endothelial cells, Free Radical Biology and Medicine, Vol. 41, No. 4 pp. 668–680. (Cited on pages 93, 105, and 181.)

Chung, S.-H.; Andersen, O. S. and Krishnamurthy, V. (**2007**): Biological Membrane Ion Channels: Dynamics, Structure, and Applications, Springer. (Cited on page 45.)

Clapham, D. E. (**1995**): Calcium signaling, Cell, Vol. 80, No. 2 pp. 259–268. (Cited on page 35.)

Cloutier, M.; Bolger, F. B.; Lowry, J. P. and Wellstead, P. (**2009**): An integrative dynamic model of brain energy metabolism using in vivo neurochemical measurements, Journal of Computational Neuroscience, Vol. 27, No. 3 pp. 391–414. (Cited on page 154.)

Comerford, A. and David, T. (**2008**a): Computer Model of Nucleotide Transport in a Realistic Porcine Aortic Trifurcation, Annals of Biomedical Engineering, Vol. 36, No. 7 pp. 1175–1187. (Cited on page 84.)

Comerford, A. and David, T. (**2008**b): eNOS concentrations in complex arterial blood flow, in **Hung, T. K.; Borovitz, H. S. and Woo, S.-Y.** (Ed.), 16th International Conference on Mechanics in Medicine and Biology, University of Pittsburgh. (Cited on page 84.)

Comerford, A.; Plank, M. J. and David, T. (**2008**): Endothelial Nitric Oxide Synthase and Calcium Production in Arterial Geometries: an Integrated Fluid Mechanics/Cell Model, Journal of Biomechanical Engineering, Vol. 130, No. 13 pp. 011010–1–13. (Cited on pages 95, 97, 98, 181, and 186.)

Condorelli, P. and George, S. C. (**2001**): In vivo control of soluble guanylate cyclase activation by nitric oxide: a kinetic analysis, Biophysical Journal, Vol. 80, No. 5 pp. 2110–2119. (Cited on page 101.)

Cox, D. H.; Cui, J. and Aldrich, R. W. (**1997**): Allosteric Gating of a large Conductance Ca-activated K+ Channel, The Journal of General Physiology, Vol. 109, No. 5 pp. 647–673. (Cited on page 45.)

Crouch, T. H. and Klee, C. B. (**1980**): Positive cooperative binding of calcium to bovine brain calmodulin., Biochemistry, Vol. 19, No. 16 pp. 3692–3698. (Cited on pages 95, 96, and 181.)

Curtis, A.; Powell, M. and Reid, J. (**1974**): On the estimation of sparse Jacobian matrices, Journal of the Institute of Mathematics and its Applications, Vol. 13, No. 1 pp. 117—-120. (Cited on page 129.)

David, T. (**2003**): Wall Shear Stress Modulation of ATP/ADP Concentration at the Endothelium, Annals of Biomedical Engineering, Vol. 31, No. 10 pp. 1231–1237. (Cited on page 84.)

David, T.; Alzaidi, S.; Chatelin, R. and Farr, H. (**2008**): Coupled Autoregulation Models, in **Goh, J.** (Ed.), 13th International Conference on Biomedical Engineering, Springer, pp. 1896–1899. (Cited on page 39.)

Davis, T. A. (**2006**): Direct Methods for Sparse Linear Systems. (Cited on page 129.)

Dawson, V. L.; Dawson, T. M.; London, E. D.; Bredt, D. S. and Snyder, S. H. (**1991**): Nitric oxide mediates glutamate neurotoxicity in primary cortical cultures, Proceedings of the National Academy of Sciences of the USA, Vol. 88, No. July pp. 6368–6371. (Cited on page 88.)

Diep, H. K.; Vigmond, E. J.; Segal, S. S. and Welsh, D. G. (**2005**): Defining electrical communication in skeletal muscle resistance arteries: a computational approach, The Journal of Physiology, Vol. 568, No. 1 pp. 267–281. (Cited on pages xix and 75.)

Dirnagl, U.; Lindauer, U. and Villringer, a. (**1993**): Role of nitric oxide in the coupling of cerebral blood flow to neuronal activation in rats, Neuroscience Letters, Vol. 149, No. 1 pp. 43–46. (Cited on page 113.)

Dobutovic, B.; Smiljanic, K.; Soskic, S.; Düngen, H.-D. and Isenovi, E. R. (**2011**): Nitric Oxide and its Role in Cardiovascular Diseases, The Open Nitric Oxide Journal, Vol. 3 pp. 65–71. (Cited on page 88.)

Dormanns, K.; von Disseldorp, E. M.; Brown, R. and David, T. (**2014**): Neurovascular coupling and the influence of luminal agonists via the endothelium, Journal of Theoretical Biology, Vol. 364 pp. 49–70. (Cited on pages xiii, xiv, 89, 90, 92, 96, 98, 101, 102, 103, 104, 105, 107, 111, 181, 183, 184, and 186.)

Dreier, J. P. (**2011**): The role of spreading depression, spreading depolarization and spreading ischemia in neurological disease, Nature Medicine, Vol. 17, No. 4 pp. 439–447. (Cited on page 146.)

Dreier, J. P.; Körner, K.; Görner, A.; Lindauer, U.; Weih, M.; Villringer, A. and Dirnagl, U. (**1995**): Nitric oxide modulates the CBF response to increased extracellular potassium, Journal of Cerebral Blood Flow and Metabolism, Vol. 15, No. 6 pp. 914–919. (Cited on page 112.)

Drewes, L. R. (**2012**): Making connexons in the neurovascular unit, Journal of Cerebral Blood Flow and Metabolism, Vol. 32, No. 8 pp. 1455–1456. (Cited on pages 4 and 11.)

Dunn, K. M.; Hill-Eubanks, D. C.; Liedtke, W. B. and Nelson, M. T. (**2013**): TRPV4 channels stimulate Ca2+-induced Ca2+ release in astrocytic endfeet and amplify neurovascular coupling responses, Proceedings of the National Academy of Sciences, Vol. 110, No. 15 pp. 6157–6162. (Cited on page 32.)

Duvernoy, H. M. (**1999**): The Human Brain, Springer, Wien, 2nd edition. (Cited on page 2.)

Edwards, F. R.; Hirst, G. D. S. and Silverberg, G. D. (**1988**): Inward Rectification in Rat Cerebral Arterioles; Involvement of Potassium Ions in Autoregulation, Journal of Physiology, Vol. 404, No. 1 pp. 455–466. (Cited on pages xii, 37, and 66.)

Endo, M.; Tanaka, M. and Ogawa, Y. (**1970**): Calcium Induced Release of Calcium from the Sarcoplasmic Reticulum of Skinned Skeletal Muscle Fibres, Nature, Vol. 228 pp. 34–36. (Cited on pages 72, 82, and 85.)

Fadel, A. A.; Barbee, K. A. and Jaron, D. (**2009**): A computational model of nitric oxide production and transport in a parallel plate flow chamber, Annals of Biomedical Engineering, Vol. 37, No. 5 pp. 943–954. (Cited on page 107.)

Fall, C. P.; Marland, E. S.; Wagner, J. M. and Tyson, J. J. (**2002**): Computational Cell Biology, Vol. 20 of Interdisciplinary Applied Mathematics, Springer. (Cited on pages x, 19, 22, 23, 24, 26, and 27.)

Farr, H. and David, T. (**2011**): Models of neurovascular coupling via potassium and EET signalling, Journal of Theoretical Biology, Vol. 286, No. 1 pp. 13–23. (Cited on pages 30, 31, 36, 37, 45, 49, 66, 69, 89, 90, and 105.)

Filosa, J. A. and Blanco, V. M. (**2007**): Neurovascular coupling in the mammalian brain, Experimental Physiology, Vol. 92, No. 4 pp. 641–646. (Cited on page 69.)

Filosa, J. A.; Bonev, A. D. and Nelson, M. T. (**2004**): Calcium dynamics in cortical astrocytes and arterioles during neurovascular coupling, Circulation Research, Vol. 95, No. 10 pp. e73–81. (Cited on pages 49 and 69.)

Filosa, J. A.; Bonev, A. D.; Straub, S. V.; Meredith, A. L.; Wilkerson, M. K.; Aldrich, R. W. and Nelson, M. T. (**2006**): Local potassium signaling couples neuronal activity to vasodilation in the brain, Nature Neuroscience, Vol. 9, No. 11 pp. 1397–1403. (Cited on pages xi, 44, 45, 47, 50, 52, 54, 55, 62, and 173.)

Fisslthaler, B.; Dimmeler, S.; Hermann, C.; Busse, R. and Fleming, I. (**2000**): Phosphorylation and activation of the endothelial nitric oxide synthase by fluid shear stress, Acta Physiologica Scandinavica, Vol. 168, No. 1 pp. 81–88. (Cited on page 97.)

Fleming, I. and Busse, R. (**1999**): NO: the primary EDRF, Journal of Molecular and Cellular Cardiology, Vol. 31, No. 1 pp. 5–14. (Cited on pages 90, 92, 107, and 114.)

Förstermann, U. (**2006**): Janus-faced role of endothelial NO synthase in vascular disease: uncoupling of oxygen reduction from NO synthesis and its pharmacological reversal, Biological Chemistry, Vol. 387, No. 12 pp. 1521–1533. (Cited on page 88.)

Förstermann, U.; Boissel, J. P. and Kleinert, H. (**1998**): Expressional control of the 'constitutive' isoforms of nitric oxide synthase (NOS I and NOS III), The FASEB Journal, Vol. 12, No. 10 pp. 773–790. (Cited on pages 88 and 93.)

Forsythe, P.; Gilchrist, M.; Kulka, M. and Befus, A. D. (**2001**): Mast cells and nitric oxide: Control of production, mechanisms of response, International Immunopharmacology, Vol. 1, No. 8 pp. 1525–1541. (Cited on pages 88, 91, 92, and 107.)

Fuji, K.; Heistad, D. D. and Faraki, F. M. (**1990**): Ionic Mechanisms in Spontaneous Vasomotion of the Rat Basilar Artery in vivo, Journal of Physiology, Vol. 430, No. 1 pp. 389–398. (Cited on page 85.)

Fung, Y. C. (**1993**): Biomechanics: Motion, Flow, Stress, and Growth, Journal of Applied Mechanics, Vol. 60, No. 2 p. 567. (Cited on pages 41 and 118.)

Furchgott, R. F. and Zawadzki, J. V. (**1980**): The obligatory role of endothelial cells in the relaxation of arterial smooth muscle by acetylcholine, Nature, Vol. 288, No. 5789 pp. 373–376. (Cited on page 87.)

Gabrys, E.; Rybaczuk, M. and Kedzia, A. (**2006**): Blood flow simulation through fractal models of circulatory system, Chaos, Solitons & Fractals, Vol. 27, No. 1 pp. 1–7. (Cited on page 41.)

Garthwaite, J. and Boulton, C. L. (**1995**): Nitric oxide signaling in the central nervous system, Annual Review of Physiology, Vol. 57 pp. 683–706. (Cited on page 88.)

Girouard, H. and Iadecola, C. (**2006**): Neurovascular coupling in the normal brain and in hypertension, stroke, and Alzheimer disease, Journal of Applied Physiology, Vol. 100, No. 1 pp. 328–335. (Cited on pages 11, 12, and 13.)

Goldbeter, A.; Dupont, G. and Berridge, M. J. (**1990**): Minimal model for signal-induced Ca2+ oscillations and for their frequency encoding through protein phosphorylation, Proceedings of the National Academy of Sciences, Vol. 87, No. 4 pp. 1461–1465. (Cited on pages 35, 72, and 73.)

Gonzalez-Fernandez, J. M. and Ermentrout, B. (**1994**): On the origin and dynamics of the vasomotion of small arteries, Mathematical Biosciences, Vol. 119, No. 2 pp. 127–167. (Cited on pages 45, 47, 49, 62, 69, 85, 118, 161, 163, and 168.)

Gore, R. W. and Davis, M. J. (**1985**): Mechanics of smooth muscle in isolated single microvessels, Annals of Biomedical Engineering, Vol. 12, No. 5 pp. 511–520. (Cited on pages 59, 60, 62, and 175.)

Grinberg, L.; Cheever, E.; Anor, T.; Madsen, J. R. and Karniadakis, G. E. (**2011**): Modeling blood flow circulation in intracranial arterial networks: A comparative 3D/1D simulation study, Annals of Biomedical Engineering, Vol. 39, No. 1 pp. 297–309. (Cited on pages 40 and 42.)

Haddock, R. E.; Grayson, T. H.; Brackenbury, T. D.; Meanez, K. R.; Neylon, C. B.; Sandow, S. L. and Hill, C. E. (**2006**): Endothelial coordination of cerebral vasomotion via myoendothelial gap junctions containing connexins 37 and 40, American Journal of Physiology. Heart and Circulatory Physiology, Vol. 291, No. 5 pp. H2047–56. (Cited on pages 44, 72, 74, and 81.)

Hadfield, J.; Plank, M. J. and David, T. (**2013**): Modeling secondary messenger pathways in neurovascular coupling, Bulletin of Mathematical Biology, Vol. 75, No. 3 pp. 428–443. (Cited on page 69.)

Hai, C. and Murphy, R. A. (**1989**): Ca2+ Crossbridge Phosphorylation, and Contraction, Annual Review of Physiology, Vol. 51, No. 1 pp. 285–298. (Cited on pages xii, 56, 62, 63, 65, 70, 81, 86, and 175.)

Hai, C. M. and Murphy, R. A. (**1988**): Cross-bridge phosphorylation and regulation of latch state in smooth muscle, American Journal of Physiology - Cell Physiology, Vol. 254 pp. C99–C106. (Cited on pages x, xix, 7, 33, 34, 66, 98, 103, 104, 107, 119, 152, and 184.)

Hamel, E. (**2006**): Perivascular nerves and the regulation of cerebrovascular tone, Journal of Applied Physiology, Vol. 100, No. 3 pp. 1059–1064. (Cited on page 4.)

Hamilton, N. B.; Attwell, D. and Hall, C. N. (**2010**): Pericyte-mediated regulation of capillary diameter: a component of neurovascular coupling in health and disease., Frontiers in neuroenergetics, Vol. 2, No. May pp. 1–14. (Cited on page 155.)

Hayashi, Y.; Nishio, M.; Naito, Y.; Yokokura, H.; Nimura, Y.; Hidaka, H. and Watanabe, Y. (**1999**): Regulation of neuronal nitric-oxide synthase by calmodulin kinases, Journal of Biological Chemistry, Vol. 274, No. 29 pp. 20597–20602. (Cited on pages 95 and 181.)

Hebert, L. E.; Weuve, J.; Scherr, P. a. and Evans, D. a. (**2013**): Alzheimer disease in the United States (2010-2050) estimated using the 2010 census, Neurology, Vol. 80, No. 19 pp. 1778–1783. (Cited on pages x and 12.)

Hill, R. A.; Tong, L.; Yuan, P.; Murikinati, S.; Gupta, S. and Grutzendler, J. (**2015**): Regional Blood Flow in the Normal and Ischemic Brain Is Controlled by Arteriolar Smooth Muscle Cell Contractility and Not by Capillary Pericytes, Neuron, Vol. 87, No. 1 pp. 95–110. (Cited on page 155.)

Hillman, E. M.; Devor, A.; Bouchard, M. B.; Dunn, A. K.; Krauss, G.; Skoch, J.; Bacskai, B. J.; Dale, A. M. and Boas, D. a. (**2007**): Depth-resolved optical imaging and microscopy of vascular compartment dynamics during somatosensory stimulation, NeuroImage, Vol. 35, No. 1 pp. 89–104. (Cited on pages 113 and 149.)

Hodgkin, A. L. and Huxley, A. F. (**1952**): A Quantitative Description of Membrane Current and its Application to Conduction and Excitation in Nerve, Bulletin of Physiology, Vol. 52, No. 1 pp. 25–71. (Cited on pages 14 and 38.)

Iadecola, C. (**2004**): Neurovascular regulation in the normal brain and in Alzheimer's disease, Nature Reviews. Neuroscience, Vol. 5, No. 5 pp. 347–360. (Cited on pages 4, 11, 43, and 44.)

Ignarro, L. J.; Buga, G. M.; Wood, K. S.; Byrns, R. E. and Chaudhuri, G. (**1987**): Endothelium-derived relaxing factor produced and released from artery and vein is nitric oxide, Proceedings of the National Academy of Sciences, Vol. 84, No. 24 pp. 9265–9269. (Cited on page 87.)

Intaglietta, M. (**1991**): Arteriolar vasomotion: implications for tissue ischemia., Blood Vessels, Vol. 28 Suppl 1 pp. 1–7. (Cited on page 149.)

Jahr, C. E. and Stevenst, C. F. (**1993**): Calcium permeability of the N-methyl-D-aspartate receptor channel in hippocampal neurons in culture, Proceedings of the National Academy of Sciences, Vol. 90, No. 12 pp. 11573–11577. (Cited on page 94.)

Joannides, R.; Haefeli, W. E.; Linder, L.; Richard, V.; Bakkali, E. H.; Thuillez, C. and Luscher, T. F. (**1995**): Nitric Oxide Is Responsible for Flow-Dependent Dilatation of Human Peripheral Conduit Arteries In Vivo, Circulation, Vol. 91, No. 5 pp. 1314–1319. (Cited on page 90.)

Karch, R.; Neumann, F.; Neumann, M. and Schreiner, W. (**1999**): A three-dimensional model for arterial tree representation, generated by constrained constructive optimization, Computers in Biology and Medicine, Vol. 29 pp. 19–38. (Cited on pages xi, 39, and 40.)

Kavdia, M. and Popel, A. S. (**2003**): Wall shear stress differentially affects NO level in arterioles for volume expanders and Hb-based O2 carriers, Microvascular Research, Vol. 66, No. 1 pp. 49–58. (Cited on pages 100 and 114.)

Kavdia, M.; Tsoukias, N. M. and Popel, A. S. (**2002**): Model of nitric oxide diffusion in an arteriole: impact of hemoglobin-based blood substitutes, American Journal of Physiology. Heart and Circulatory Physiology, Vol. 282, No. 6 pp. 2245–2253. (Cited on pages 99, 101, 181, 182, and 186.)

Keener, J. and Sneyd, J. (**2009**): Mathematical Physiology, Springer. (Cited on pages 14, 18, 21, 73, and 93.)

Keizer, J. and De Young, G. W. (**1992**): Two roles of Ca2+ in agonist stimulated Ca2+ oscillations, Biophysical Journal, Vol. 61, No. 3 pp. 649–660. (Cited on page 72.)

Kimelberg, H. K. (**2004**): The problem of astrocyte identity, Neurochemistry International, Vol. 45, No. 2-3 pp. 191–202. (Cited on page 6.)

Koenigsberger, M.; Sauser, R.; Bény, J.-L. and Meister, J.-J. (**2005**): Role of the endothelium on arterial vasomotion, Biophysical Journal, Vol. 88, No. 6 pp. 3845–3854. (Cited on pages xix, 34, 72, 73, 75, 170, and 175.)

Koenigsberger, M.; Sauser, R.; Bény, J.-L. and Meister, J. J. (**2006**): Effects of arterial wall stress on vasomotion, Biophysical journal, Vol. 91, No. September pp. 1663–1674. (Cited on pages x, 34, 35, 36, 52, 58, 62, 73, 75, 103, 104, 119, 164, 165, 166, 167, 168, 169, 170, 171, 172, 173, 175, and 184.)

Koenigsberger, M.; Sauser, R.; Lamboley, M.; Bény, J.-L. and Meister, J.-J. (**2004**): Ca2+ dynamics in a population of smooth muscle cells: modeling

the recruitment and synchronization, Biophysical Journal, Vol. 87, No. 1 pp. 92–104. (Cited on page 34.)

Kuchibhotla, K. V.; Lattarulo, C. R.; Hyman, B. T. and Bacskai, B. J. (**2009**): Synchronous Hyperactivity and Intercellular Calcium Waves in Astrocytes in Alzheimer Mice, Science, Vol. 323, No. 5918 pp. 1211–1215. (Cited on page 30.)

LaFerla, F. M. (**2002**): Calcium dyshomeostasis and intracellular signalling in Alzheimer's disease, Nature Reviews. Neuroscience, Vol. 3, No. November pp. 862–872. (Cited on page 30.)

Lancaster, J. R. (**1994**): Simulation of the diffusion and reaction of endogenously produced nitric oxide, Proceedings of the National Academy of Sciences of the United States of America, Vol. 91, No. 17 pp. 8137–8141. (Cited on page 90.)

Lancaster, J. R. (**1997**): A Tutorial on the Diffusibility and Reactivity of Free Nitric Oxide, Nitric Oxide, Vol. 1, No. 1 pp. 18–30. (Cited on page 99.)

Laranjinha, J. a.; Santos, R. M.; Lourenço, C. F.; Ledo, A. and Barbosa, R. M. (**2012**): Nitric oxide signaling in the brain: translation of dynamics into respiration control and neurovascular coupling, Annals of the New York Academy of Sciences, Vol. 1259, No. 1 pp. 10–18. (Cited on page 106.)

Laurent, M.; Lepoivre, M. and Tenu, J.-p. (**1996**): Kinetic modelling of the nitric oxide gradient generated in vitro by adherent cells expressing inducible nitric oxide synthase, Biochemical Journal, Vol. 314 pp. 109–113. (Cited on page 99.)

LeCrux, C. and Hamel, E. (**2011**): Review: The neurovascular unit in brain function and disease, Acta Physiologica, Vol. 203, No. 1 pp. 47–59. (Cited on pages 70 and 149.)

Lemon, G.; Gibson, W. G. and Bennett, M. R. (**2003**): Metabotropic receptor activation, desensitization and sequestration - I: Modelling calcium and inositol 1,4,5-trisphosphate dynamics following receptor activation, Journal of Theoretical Biology, Vol. 223, No. 1 pp. 93–111. (Cited on page 31.)

Logan, J. D. (**2013**): Applied Mathematics, Wiley Online Library, 4th edition. (Cited on page 27.)

Lok, J.; Gupta, P.; Guo, S.; Kim, W. J.; Whalen, M. J.; van Leyen, K. and Lo, E. H. (**2007**): Cell-cell signaling in the neurovascular unit, Neurochemical Research, Vol. 32, No. 12 pp. 2032–45. (Cited on pages 10, 38, 43, and 44.)

Lourenco, C. F.; Barbosa, R. M. and Laranjinha, J. a. (**2014**): Nitric Oxide-Mediated Neurovascular Coupling Is Impaired in the Triple-Transgenic

Mouse Model of Alzheimer's Disease Due to Cerebrovascular Dysfunction, Free Radical Biology and Medicine, Vol. 76 p. S25. (Cited on page 114.)

MacNeilage, P. F.; Rogers, L. J. and Vallortigara, G. (**2009**): Origins of the left & right brain, Scientific American, Vol. 301, No. 1 pp. 60–67. (Cited on page 2.)

Magistretti, P. J. and Ransom, B. R. (**2002**): Astrocytes, Neuropsychopharmacology: The Fifth Generation of Progress, , No. 15 pp. 133–145. (Cited on page 29.)

Malinski, T.; Taha, Z.; Grunfeld, S.; Patton, S.; Kapturczak, M. and Tomboulian, P. (**1993**): Diffusion of Nitric Oxide in the Aorta Wall Monitored in Situ by Porphyrinic Microsensors, Biochemical and Biophysical Research Communications, Vol. 193, No. 3 pp. 1076–1082. (Cited on pages 90, 99, 114, and 178.)

Mattson, M. P.; LaFerla, F. M.; Chan, S. L.; Leissring, M. a.; Shepel, P. N. and Geiger, J. D. (**2000**): Calcium signaling in the ER: its role in neuronal plasticity and neurodegenerative disorders., Trends in Neurosciences, Vol. 23, No. 5 pp. 222–229. (Cited on page 31.)

Mayer, B. and Hemmens, B. (**1997**): Biosynthesis and action of nitric oxide in mammalian cells, Trends in Biochemical Sciences, Vol. 22, No. 12 pp. 477–481. (Cited on pages 88, 93, and 100.)

Michaelis, L. and Menten, M. L. (**1913**): Die Kinetik der Invertinwirkung, Biochemische Zeitschrift, Vol. 49, No. 2 pp. 333–369. (Cited on pages x, 18, 19, and 20.)

Miller, A. K.; Alston, R. L. and Corsellis, J. A. (**1980**): Variation with age in the volumes of grey and white matter in the cerebral hemispheres of man: measurements with an image analyser, Neuropathology and Applied Neurobiology, Vol. 6, No. 2 pp. 119–132. (Cited on page 3.)

Moore, S. M.; Moorhead, K. T.; Chase, J. G.; David, T. and Fink, J. (**2005**): One-Dimensional and Three-Dimensional models of Cerebrovascular Flow, Journal of Biomechanical Engineering, Vol. 127, No. 3 pp. 440–449. (Cited on page 42.)

Nagelhus, E.; Horio, Y. and Inanobe, A. (**1999**): Immunogold evidence suggests that coupling of K+ siphoning and water transport in rat retinal muller cells is mediated by a coenrichment of kir4. 1 and aqp4 in specific membrane domains, Glia, Vol. 63, No. 1 pp. 47–54. (Cited on pages 50 and 159.)

Netter, F. H. (**2014**): Atlas of human anatomy, Saunders, Elsevier, 6th edition. (Cited on pages ix and 9.)

Nichols, W. W.; O'Rourke, M. F. and Vlachopoulos, C. (**1992**): McDonald's blood flow in arteries; theoretical, experimental and clinical principles, Vol. 23, CRC Press. (Cited on page 42.)

Nizar, K.; Uhlirova, H.; Tian, P.; Saisan, P. A.; Cheng, Q.; Reznichenko, L.; Weldy, K. L.; Steed, T. C.; Sridhar, V. B.; MacDonald, C. L.; Cui, J.; Gratiy, S. L.; Sakadzic, S.; Boas, D. A.; Beka, T. I.; Einevoll, G. T.; Chen, J.; Masliah, E.; Dale, A. M.; Silvia, G. A. and Devor, A. (**2013**): In vivo Stimulus-Induced Vasodilation Occurs without IP_3 Receptor Activation and May Precede Astrocytic Calcium Increase, The Journal of Neuroscience, Vol. 33, No. 19 pp. 8411–8422. (Cited on page 69.)

Østby, I.; Øyehaug, L.; Einevoll, G. T.; Nagelhus, E. a.; Plahte, E.; Zeuthen, T.; Lloyd, C. M.; Ottersen, O. P. and Omholt, S. W. (**2009**): Astrocytic Mechanisms Explaining Neural-Activity-Induced Shrinkage of Extraneuronal Space, PLoS Computational Biology, Vol. 5, No. 1 p. e1000272. (Cited on pages x, 7, 29, 31, 32, 45, 47, 49, 50, 157, 158, 161, and 163.)

Ottesen, J. and Olufsen, M. (**2004**): Applied mathematical models in human physiology, SIAM Monographs. (Cited on page 123.)

Pantoni, L. and Gorelick, P. B. (**2014**): Cerebral Small Vessel Disease, Cambridge University Press. (Cited on page 9.)

Parthimos, D.; Edwards, D. H. and Griffith, T. M. (**1999**): Minimal model of arterial chaos generated by coupled intracellular and membrane Ca2+ oscillators, American Journal of Physiology - Heart and Circulatory Physiology, Vol. 277, No. 3 pp. H1119–H1144. (Cited on pages 34, 35, 56, 72, 73, and 74.)

Petersen, R. C. (**2010**): Alzheimer's disease: progress in prediction., Lancet neurology, Vol. 9, No. 1 pp. 4–5. (Cited on pages x and 12.)

Purves, D.; Augustine, G. J.; Fitzpatrick, D.; Hall, W. C.; LaMantia, A. S.; McNamara, J. O. and White, L. E. (**2008**): Neuroscience, De Boeck, Sinauer, Sunderland. (Cited on pages 6 and 25.)

Quaegebeur, A.; Lange, C. and Carmeliet, P. (**2011**): The neurovascular link in health and disease: molecular mechanisms and therapeutic implications., Neuron, Vol. 71, No. 3 pp. 406–24. (Cited on page 10.)

Rafikov, R.; Fonseca, F. V.; Kumar, S.; Pardo, D.; Darragh, C.; Elms, S.; Fulton, D. and Black, S. M. (**2011**): eNOS activation and NO function: structural motifs responsible for the posttranslational control of endothelial nitric oxide synthase activity, The Journal of Endocrinology, Vol. 210, No. 3 pp. 271–284. (Cited on page 88.)

Ramachandran, V. S. (**2002**): Encyclopedia of the Human Brain, Academic Press, 4th edition. (Cited on page 6.)

Rivadulla, C.; de Labra, C.; Grieve, K. L. and Cudeiro, J. (**2011**): Vasomotion and neurovascular coupling in the visual thalamus in vivo, PloS ONE, Vol. 6, No. 12 p. e28746. (Cited on page 83.)

Roy, C. S. and Sherrington, C. (**1890**): On the regulation of the blood-supply of the brain, The Journal of Physiology, Vol. 11, No. 1-2 pp. 85–118. (Cited on page 36.)

Rücker, M.; Strobel, O.; Vollmar, B.; Roesken, F. and Menger, M. (**2000**): Vasomotion in critically perfused muscle protects adjacent from capillary perfusion failure, American Journal of Physiology - Heart and Circulatory Physiology, Vol. 279, No. 2 pp. H550–H558. (Cited on pages 84 and 86.)

Sakurai, T. and Terui, N. (**2006**): Effects of sympathetically induced vasomotion on tissue-capillary fluid exchange, American Journal of Physiology - Heart and Circulatory Physiology, Vol. 291, No. 4 pp. H1761–H1767. (Cited on pages 84 and 86.)

Santucci, D. M. and Raghavachari, S. (**2008**): The Effects of NR2 Subunit-Dependent NMDA Receptor Kinetics on Synaptic Transmission and CaMKII Activation, PLoS Computational Biology, Vol. 4, No. 10 p. e1000208. (Cited on pages 30, 93, 94, 95, and 181.)

Schreiner, W. and Buxbaum, P. F. (**1993**): Computer-optimization of vascular trees, IEEE Transactions on Biomedical Engineering, Vol. 40, No. 5 pp. 482–491. (Cited on page 39.)

Schreiner, W.; Karch, R.; Neumann, F.; Rödler, S. M. and End, A. (**2000**): Adaptive Growth and Optimization of Coronary Arterial Tree Models, International Journal of Bioelectromagnetism, Vol. 2, No. 2 pp. 1–7. (Cited on page 39.)

Schutter, E. D. E. and Smolen, P. (**1998**): Calcium Dynamics in Large Neuronal Models, Methods in Neuronal Modeling: From Ions to Networks, Vol. 2 pp. 211–250. (Cited on pages 30 and 31.)

Shaikh, M. A.; Wall, D. J. N. and David, T. (**2011**): Macro-scale phenomena of arterial coupled cells: a massively parallel simulation, Journal of The Royal Society Interface, Vol. 9 pp. 1–17. (Cited on pages xix, 74, and 75.)

Singer, H. A. and Murphy, R. A. (**1987**): Maximal rates of activation in electrically stimulated swine carotid media, Circulation Research, Vol. 60, No. 3 pp. 438–445. (Cited on page 33.)

Sneyd, J.; Keizer, J. and Sanderson, M. J. (**1995**a): Mechanisms of calcium oscillations and waves: a quantitative analysis, The FASEB Journal, Vol. 9, No. 14 pp. 1463–1472. (Cited on page 99.)

Sneyd, J.; Wetton, B. T.; Charles, A. C. and Sanderson, M. J. (**1995**b): Intercellular calcium waves mediated by diffusion of inositol trisphosphate: a two-dimensional model, The American Journal of Physiology, Vol. 268, No. 6 pp. C1537–C1545. (Cited on page 99.)

Stockand, J. D. and Sansom, S. C. (**1996**): Mechanism of activation by cGMP-dependent protein kinase of large Ca2+-activated K+ channels in mesangial cells, American Journal of Physiology - Cell Physiology, Vol. 271, No. 5 pp. C1669–C1677. (Cited on pages 104 and 184.)

Syková, E. and Nicholson, C. (**2008**): Diffusion in brain extracellular space, Physiological Reviews, Vol. 88, No. 4 pp. 1277–1340. (Cited on pages 129, 130, and 154.)

Tabatabaei, S. N. and Girouard, H. (**2014**): Nitric Oxide, Vitamins and Hormones, Vol. 96, No. 441 pp. 347–385. (Cited on page 114.)

Takenaka, T.; Suzuki, H.; Okada, H.; Hayashi, K.; Kanno, Y. and Saruta, T. (**1998**): Mechanosensitive cation channels mediate afferent arteriolar myogenic constriction in the isolated rat kidney, The Journal of Physiology, Vol. 511, No. 1 pp. 245–53. (Cited on pages 35 and 150.)

Vaughn, M. W.; Kuo, L. and Liao, J. C. (**1998**): Estimation of nitric oxide production and reaction rates in tissue by use of a mathematical model, American Journal of Physiology - Heart and Circulatory Physiology, Vol. 274, No. 6 pp. H2163—-H2176. (Cited on page 99.)

Vrselja, Z.; Brkic, H.; Mrdenovic, S.; Radic, R. and Curic, G. (**2014**): Function of circle of Willis, Journal of Cerebral Blood Flow and Metabolism, Vol. 34, No. 4 pp. 578–584. (Cited on page 8.)

Wang, D. D. and Bordey, A. (**2008**): The astrocyte odyssey, Progress in Neurobiology, Vol. 86, No. 4 pp. 342–367. (Cited on page 6.)

Webb, R. C. (**2003**): Smooth muscle contraction and relaxation, Advances in Physiology Education, Vol. 27, No. 4 pp. 201–206. (Cited on page 7.)

Wiesner, T. F.; Berk, B. C. and Nerem, R. M. (**1997**): A mathematical model of the cytosolic-free calcium response in endothelial cells to fluid shear stress, Proceedings of the National Academy of Sciences, Vol. 94, No. 8 pp. 3726–3731. (Cited on pages 97, 98, and 118.)

Witthoft, A.; Filosa, J. A. and Karniadakis, G. E. (**2013**): Potassium Buffering in the Neurovascular Unit: Models and Sensitivity Analysis, Biophysical Journal, Vol. 105, No. 9 pp. 2046–2054. (Cited on pages 4, 32, and 37.)

Witthoft, A. and Karniadakis, G. E. (**2012**): A bidirectional model for communication in the neurovascular unit, Journal of Theoretical Biology, Vol. 311 pp. 80–93. (Cited on pages 31 and 37.)

Wood, J. and Garthwaite, J. (**1994**): Models of the diffusional spread of nitric oxide: implications for neural nitric oxide signalling and its pharmacological properties, Neuropharmacology, Vol. 33, No. 1 pp. 1235–1244. (Cited on page 99.)

Woods, N. K. and Padmanabhan, J. (**2012**): Neuronal calcium signaling and Alzheimer's disease, Adv Exp Med Biol, Vol. 740 pp. 1193–1217. (Cited on page 154.)

Wu, R. S. and Marx, S. O. (**2010**): The BK potassium channel in the vascular smooth muscle and kidney: α- and β-subunits, Kidney International, Vol. 78, No. 10 pp. 963–974. (Cited on page 78.)

Yang, J.; Clark, J. W.; Bryan, R. M. and Robertson, C. S. (**2005**): Mathematical modeling of the nitric oxide/cGMP pathway in the vascular smooth muscle cell, American Journal of Physiology - Heart and Circulatory Physiology, Vol. 289, No. 2 pp. H886–H897. (Cited on pages x, 34, 90, 101, 102, 103, 107, 146, and 184.)

Zhang, X. and Le, W. (**2010**): Pathological role of hypoxia in Alzheimer's disease., Experimental neurology, Vol. 223, No. 2 pp. 299–303. (Cited on page 11.)

Zlokovic, B. V. (**2005**): Neurovascular mechanisms of Alzheimer's neurodegeneration., Trends in neurosciences, Vol. 28, No. 4 pp. 202–8. (Cited on pages 7, 9, 11, 12, and 147.)

Zlokovic, B. V. (**2011**): Neurovascular pathways to neurodegeneration in Alzheimer's disease and other disorders, Nature Reviews. Neuroscience, Vol. 12, No. 12 pp. 723–738. (Cited on pages ix, 9, 11, 12, and 38.)

Zonta, M.; Angulo, M. C.; Gobbo, S.; Rosengarten, B.; Hossman, K.-A.; Pozzan, T. and Carmignoto, G. (**2003**): Neuron-to-Astrocyte signaling is central to the dynamic control of brain microcirculation, Nature Neuroscience, Vol. 6, No. 1 pp. 43–50. (Cited on page 69.)

Zoppo, G. J. and Mabuchi, T. (**2003**): Cerebral Microvessel Responses to Focal Ischemia, Journal of Cerebral Blood Flow and Metabolism, Vol. 23 pp. 879–894. (Cited on page 4.)

Zorrilla-Zubilete, A. M.; Maur, G. D.; Palumbo, L. M. and Genaro, M. A. (**2010**): Role of Nitric Oxide Signaling Pathways in Brain Injuries, Current Chemical Biology, Vol. 4, No. 3 pp. 250–261. (Cited on pages 89, 113, and 114.)

DECLARATION

I declare that this dissertation is my own unaided work. It is being submitted for the degree of Doctor of Philosophy at the University of Canterbury. It has not been submitted for any other degree or examination in any other University.

Katharina Dormanns